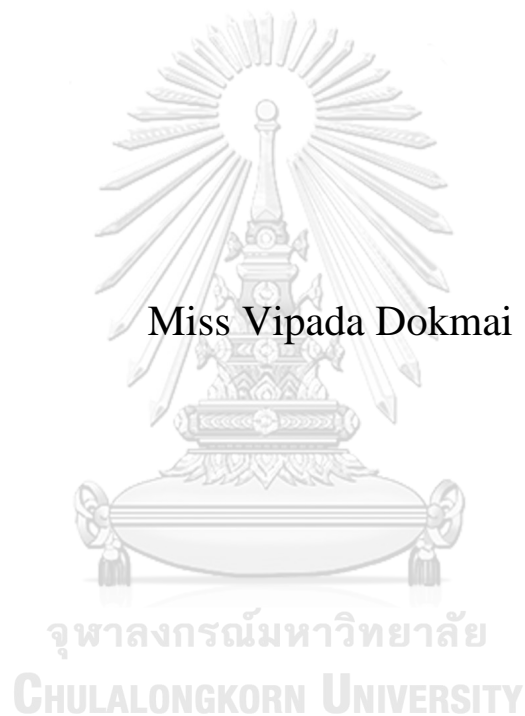


STUDY OF INTERACTIONS BETWEEN MAGNESIUM SILI-
CATE PARTICLE AND DIAMOND-
LIKE CARBON USING ATOMIC FORCE MICROSCOPY



Miss Vipada Dokmai

A Dissertation Submitted in Partial Fulfillment of the Requirements
for the Degree of Doctor of Engineering in Chemical Engineering
Department of Chemical Engineering
FACULTY OF ENGINEERING
Chulalongkorn University
Academic Year 2020
Copyright of Chulalongkorn University

การศึกษาปฏิสัมพันธ์ระหว่างอนุภาคแมกนีเซียมซิติเลตกับคาร์บอนคล้ายเพชรด้วยกล้องจุลทรรศน์
แรงอะตอม



วิทยานิพนธ์นี้เป็นส่วนหนึ่งของการศึกษาตามหลักสูตรปริญญาวิทยาศาสตรดุษฎีบัณฑิต
สาขาวิชาวิศวกรรมเคมี ภาควิชาวิศวกรรมเคมี
คณะวิศวกรรมศาสตร์ จุฬาลงกรณ์มหาวิทยาลัย
ปีการศึกษา 2563
ลิขสิทธิ์ของจุฬาลงกรณ์มหาวิทยาลัย

Thesis Title STUDY OF INTERACTIONS BETWEEN MAGNESIUM SILICATE PARTICLE AND DIAMOND-LIKE CARBON USING ATOMIC FORCE MICROSCOPY

By Miss Vipada Dokmai

Field of Study Chemical Engineering

Thesis Advisor Associate Professor VARONG PAVARAJARN, Ph.D.

Thesis Co Advisor Witchukorn Phuthong, Ph.D.

Accepted by the FACULTY OF ENGINEERING, Chulalongkorn University
in Partial Fulfillment of the Requirement for the Doctor of Engineering

----- Dean of the FACULTY OF
ENGINEERING
(Associate Professor SUPOT
TEACHAVORASINSKUN, D.Eng.)

DISSERTATION COMMITTEE

----- Chairman
(Chanchana Thanachayanont, Ph.D.)

----- Thesis Advisor
(Associate Professor VARONG PAVARAJARN, Ph.D.)

----- Thesis Co-Advisor
(Witchukorn Phuthong, Ph.D.)

----- Examiner
(Professor SARAWUT RIMDUSIT, Ph.D.)

----- Examiner
(Rungthiwa Methaapanon, Ph.D.)

----- Examiner
(Assistant Professor Paravee Vas-Umnuay, Ph.D.)

CHULALONGKORN UNIVERSITY

วิภาดา ดอกไม้ : การศึกษาปฏิสัมพันธ์ระหว่างอนุภาคแมกนีเซียมซิลิเกตกับคาร์บอนคล้ายเพชรด้วยกล้องจุลทรรศน์แรงอะตอม. (

STUDY OF INTERACTIONS BETWEEN MAGNESIUM SILICATE PARTICLE AND DIAMOND-LIKE CARBON USING ATOMIC FORCE MICROSCOPY) อ.ที่ปรึกษาหลัก :

รศ.ดร.วรงค์ ปวรอาจารย์, อ.ที่ปรึกษาร่วม : ดร.วิฑูกร กูทอง

ปฏิสัมพันธ์ระหว่างอนุภาคและพื้นผิวต่างๆภายใต้สภาวะบรรยากาศได้ถูกศึกษาโดยใช้สเปกโตรสโคปีของแรงที่อยู่บนพื้นฐานการใช้กล้องจุลทรรศน์แรงอะตอม งานวิจัยนี้มุ่งเน้นไปที่กลไกการยึดเกาะและปัจจัยที่มีผลกระทบต่อการศึกษาของอนุภาคบนพื้นผิว อนุภาคที่สนใจประกอบด้วยอนุภาคแมกนีเซียมซิลิเกต (แป้งฝุ่น) และอนุภาคซิงค์ออกไซด์ ซึ่งมีสมบัติที่น่าสนใจและมีผลกระทบต่อสิ่งแวดล้อมหลายประการ แรงยึดเกาะได้ถูกเริ่มวัดโดยใช้หัววัดกล้องจุลทรรศน์แรงอะตอมชนิดซิลิกอน และซิลิกอนที่เคลือบด้วยฟิล์มคาร์บอนคล้ายเพชรเคลงบนพื้นผิวของอนุภาคแป้งฝุ่นที่ถูกปรับปรุงด้วยกรดไฮโดรคลอริกหรือสารออกฤทธิ์ไนโซเลนต่างๆ วิธีการปรับปรุงเหล่านี้เปลี่ยนแปลงความชอบน้ำและความไม่ชอบน้ำของอนุภาค ผลการทดลองแสดงให้เห็นว่าค่าแรงยึดเกาะแบ่งออกเป็นสองกลุ่มซึ่งคาดเดาได้ว่ามาจากพื้นผิวสองประเภทของอนุภาคแป้งฝุ่นอันได้แก่พื้นผิวด้านหน้า (ไม่ชอบน้ำ) และพื้นผิวด้านขอบ (ชอบน้ำ) การดูดซับและความแข็งแรงของการยึดเกาะที่ได้จากอนุภาคที่มีความชอบน้ำกับพื้นผิวที่มีความชอบน้ำจะมากกว่าอนุภาคที่ไม่ชอบน้ำกับพื้นผิวที่ชอบน้ำและมากกว่าอนุภาคที่ไม่ชอบน้ำกับพื้นผิวที่ไม่ชอบน้ำ การกระจายตัวแบบสองกลุ่มนี้พบได้ในอนุภาคซิงค์ออกไซด์ที่เราสามารถแยกแยะความแตกต่างของพื้นผิวได้อย่างชัดเจนจากรูปร่างของอนุภาค โดยที่พื้นผิวที่มีขั้วอยู่ที่บริเวณด้านบนและด้านล่างของอนุภาคซิงค์ออกไซด์ขนาดไมครอน ในขณะที่พื้นผิวที่ไม่มีขั้วจะมาจากซิงค์ออกไซด์ชนิดแท่งขนาดนาโน นอกเหนือจากนั้นยังมีการศึกษาปฏิสัมพันธ์ของหัววัดของกล้องจุลทรรศน์แรงอะตอมที่ถูกปรับด้วยหมู่ฟังก์ชันที่ปลายที่แตกต่างกันเพื่ออธิบายความสัมพันธ์ระหว่างปฏิสัมพันธ์ของการยึดเกาะและกลไกการดูดซับ ผลที่ได้เน้นคล้ายคลึงกับอนุภาคแป้งฝุ่นคือปฏิสัมพันธ์ของสารมีขั้ว-มีขั้วจะมากกว่าสารมีขั้ว-ไม่มีขั้วและมากกว่าสารไม่มีขั้ว-ไม่มีขั้ว อย่างไรก็ตามการกระจายตัวของอิเล็กตรอนและการจัดเรียงอะตอมบนพื้นผิวที่มีผลต่อแรงยึดเกาะของอนุภาคเช่นกัน โดยภาพรวมงานนี้แสดงให้เห็นว่าแรงระหว่างโมเลกุลนั้นสำคัญต่อปฏิสัมพันธ์ของยึดเกาะระหว่างอนุภาคกับพื้นผิว โดยเฉพาะอย่างยิ่งแรงแวนเดอร์วาล์วและผลของความไม่ชอบน้ำ

จุฬาลงกรณ์มหาวิทยาลัย
CHULALONGKORN UNIVERSITY

สาขาวิชา วิศวกรรมเคมี
ปีการศึกษา 2563

ลายมือชื่อนิสิต
ลายมือชื่อ อ.ที่ปรึกษาหลัก
ลายมือชื่อ อ.ที่ปรึกษาร่วม

5871419121 : MAJOR CHEMICAL ENGINEERING

KEYWORD Force spectroscopy Adhesion Hydrophobic character Surface
D: modification Talc treatments ZnO particles

Vipada Dokmai :
STUDY OF INTERACTIONS BETWEEN MAGNESIUM SILICATE PA
RTICLE AND DIAMOND-
LIKE CARBON USING ATOMIC FORCE MICROSCOPY. Advisor:
Assoc. Prof. VARONG PAVARAJARN, Ph.D. Co-advisor: Witchukorn
Phuthong, Ph.D.

Interaction between particles and different surfaces under ambient condition is studied using AFM-based force spectroscopy. This work focuses on the adhesion mechanism and factors affecting particle-surface adhesion. The particles of interest consist of magnesium silicate (talcum powder) and zinc oxide (ZnO) particles, which have very attractive properties and are widely used in several applications. The adhesion force measurements were first carried out using silicon/silicon coated with DLC probes pressed on talc particles modified with hydrochloric acid or different organosilanes. These modifications change hydrophobicity and hydrophilicity of the particles. The results show that the adhesion forces are distributed in a bimodal fashion. It is postulated that they originate from two types of surface of talc particles, i.e., face surface (hydrophobic character) and edge surface (hydrophilic character). The adsorption and adhesion strength are in the following trend: hydrophilic-hydrophilic > hydrophilic-hydrophobic > hydrophobic-hydrophobic. Similar bimodal distribution was also observed for ZnO particles, of which could be distinguished by controlling the shape of particles. The polar surface is obtained from the top and bottom of micron-sized ZnO powder while the nonpolar surface is obtained from the side plane of ZnO nanorods. Moreover, interaction with AFM probes that were chemically modified with different terminal functional groups was also investigated, in order to describe relationship between the adhesion interactions and adsorption mechanism. The results show the same trend as in talc particles, i.e., polar-polar interaction is stronger than polar-nonpolar interaction, and the weakest adhesion was observed from nonpolar-nonpolar interaction. However, electronic distribution and the atomic arrangement on the surface also affect the adhesion. In general, this work demonstrates that the intermolecular forces are important for the particles-surface interactions, especially van der Waals forces and hydrophobic effect.

Field of Study: Chemical Engineering

Student's Signature

Academic Year: 2020

.....
Advisor's Signature

Year:

.....
Co-advisor's Signature

.....

ACKNOWLEDGEMENTS

I would like to sincere gratitude to my thesis advisor and co-advisor, Assoc.Prof. Varong Pavarajarn and Dr. Witchukorn Phuthong, at Department of Chemical Engineering, Chulalongkorn University and Department of Physics, Faculty of Science, Kasetsart University, for his helpful, extensive guidance, valuable suggestion, deep discussion and encouragement to pass obstacles throughout of this work. Besides her advisor and co-advisor, the author would like to thank another co-advisor, Dr. Worasom Kundhikanjana for her extensive knowledge, helpful discussion, technical advice, and valuable recommendations about AFM analysis.

Furthermore, I would also like to thank Dr. Chanchana Thanachayanont as the chairman, Prof. Sarawut Rimdusit, Asst. Prof. Dr. Paravee Vas-Umnuay and Dr. Rungthiwa Methaapanon for their useful discussions and participation as thesis committee.

The author received the full-expense scholarship from the Thailand Science Research and Innovation through Research and Researchers for Industries Program (RRI) which collaborated with Western Digital Thailand Co., Ltd. Also, this work is also partially financial support by Chulalongkorn University. I also appreciate technical support and the special facilities from Center for Scientific and Technological Equipment (CSTE), Suranaree University of Technology (SUT), the Synchrotron Light Research Institute (Public Organization), Thailand and National Nanotechnology Center (NANOTEC).

Furthermore, I also extend my thanks to the Center of Excellence in Particle Technology and Material Processing, Department of Chemical Engineering, Chulalongkorn University for their partial support and all my friends who always provide assistance and encouragement.

Finally, I would like to especially thank and appreciate my parents who always love, support and advise throughout the course of my life.

Vipada Dokmai

TABLE OF CONTENTS

	Page
ABSTRACT (THAI)	iii
ABSTRACT (ENGLISH).....	iv
ACKNOWLEDGEMENTS	v
TABLE OF CONTENTS.....	vi
LIST OF TABLES	ix
LIST OF FIGURES	x
CHAPTER I INTRODUCTION.....	1
CHAPTER II THEORY AND LITERATURE REVIEWS	4
2.1 Particles of interest	4
2.1.1 Magnesium silicate	4
2.1.2 Zinc oxide (ZnO).....	8
2.2 Principle of AFM analysis.....	9
2.3 Particle adhesion theory	15
2.3.1 Van der Waals forces.....	15
2.3.2 Electrostatic forces in vacuum and air.....	16
2.3.3 Effect of relative humidity on adhesion.....	17
2.3.4 Effect of contact area on adhesion.....	17
2.3.5 Effect of temperature on adhesion.....	18
2.4 Adhesion measurement and control	18
CHAPTER III EFFECTS OF CATALYST SURFACES ON ADSORPTION REVEALED BY ATOMIC FORCE MICROSCOPE FORCE SPECTROSCOPY: PHOTOCATALYTIC DEGRADATION OF DIURON OVER ZINC OXIDE	23
3.1 INTRODUCTION	25

3.2 METHODOLOGY	29
3.2.1 Synthesis of ZnO particles	29
3.2.2 Sample preparation for AFM imaging and force spectroscopy.....	30
3.2.3 Chemical functionalization of AFM probe surface	31
3.2.4 AFM measurements and analyses	34
3.2.5 Charge distribution model	35
3.3 RESULTS AND DISCUSSION.....	35
3.3.1 Characterization of ZnO particles	35
3.3.2 Characterization of the modified AFM probes.....	40
3.3.3 Adhesion measurements from AFM-based force-distance curves.....	44
3.3.4 Estimation of Hamaker constants from AFM-based force-distance curves	
57	
3.3.5 Simulation of charge distribution of the probe-modifying molecules	61
3.4 CONCLUSION	69
CHAPTER IV AFM-BASED FORCE SPECTROSCOPY STUDY OF HYDROPHOBIC/ HYDROPHILIC ATTRACTION'S INFLUENCE ON TALCUM ADHESION	71
4.1 INTRODUCTION.....	73
4.2 EXPERIMENTAL DETAILS.....	76
4.2.1 Particle modification	76
4.2.2 Characterizations	77
4.2.3 Sample preparation for AFM imaging and force spectroscopy.....	78
4.2.4 Chemical functionalization of AFM tip surface.....	78
4.2.5 AFM Measurements and analyses.....	80
4.3 RESULTS AND DISCUSSION.....	82
4.3.1 Morphology of talc particles	82
4.3.2 Characteristic of surface-modified talc	85
4.3.3 Characteristic of the modified AFM probes.....	89
4.3.4 Effects of modified surface on the talc structure.....	89
4.3.5 Adhesion measurements.....	92

4.4 CONCLUSION	107
CHAPTER V CONCLUSION AND RECOMMENDATION.....	108
5.1 Conclusions	108
5.2 Recommendation and Future directions	109
REFERENCES	111
APPENDICES	123
APPENDIX A Adhesion measurements after classification and statistical tests ..	124
APPENDIX B Linear model fits for the correlations between the maximum adhesion forces within the observed ranges by Si-tip/DLC-tip and the contact angle of unmodified/modified talc particles.....	126
VITA.....	127



LIST OF TABLES

	Page
Table 1 gives a summary of interactions that have been measured using the AFM..	14
Table 2 Adhesion energies (aJ) between functionalized/non-functionalized probes and ZnO surfaces.	48
Table 3 Summary of adhesion energies determined between functionalized/non-functionalized probes and ZnO surfaces.....	51
Table 4 Estimated Hamaker constant between ZnO surfaces and various AFM terminated surfaces.	59
Table 5 The water contact angle of different surface-modified talc particles	92
Table 6 Summarize of adhesion force obtained between different tip types and surface-modified talc.	96
Table 7 Estimated Hamaker constant between talc-modified surface and AFM tips.	104
Table 8 Estimated Hamaker constant between the different terminated surfaces of AFM tip and modified/unmodified talc particles.....	106

LIST OF FIGURES

	Page
Figure 1 Magnesium silicate surface [8].	5
Figure 2 Crystal structure of talc [26].	7
Figure 3 Schematic representation of atomic force microscope [37].	10
Figure 4 The characteristic of I_{PSD} vs. Z_p curves are converted to force vs. distance curves when (a) for hard tip and sample without surface forces and (b) hard materials with a long-range repulsion [40].	11
Figure 5 Schematic diagram of the cantilever and tip movement during the approach and retract parts of a force spectroscopy experiment.	12
Figure 6 Schematic drawing of a chemically modified tip with functional groups X that provide a specific interaction on the sample surface.	21
Figure 7 Change in charge depending on pH of the buffer [54].	22
Figure 8 Molecular structure of diuron.	29
Figure 9 Molecular structures of APTMS (A), CPTMS (B), and HDTMS (C).	33
Figure 10 Morphology of ZnO particles. (A) and (C) SEM images, (B) and (D) AFM deflection images of conventional hexagonal ZnO particles and nanorod particles, respectively.	38
Figure 11 AFM topography images of ZnO particles. (A) and (D) AFM topography images, (B) and (E) height profiles of conventional hexagonal ZnO particles and ZnO nanorod particles, (C) and (F, G) the distributions of the conventional ZnO particles' side length and the ZnO nanorods' diameter and side length, respectively.	39
Figure 12 XPS Spectra of the functionalized AFM probes and high resolution Si2p and O1s XPS spectra of the Si AFM probes after silanization process with APTMS (A), CPTMS (B), and HDTMS (C). The N1s spectrum is also included for the probe modified with APTMS (A) and the Cl2p XPS spectrum for the probe modified with CPTMS (B).	41
Figure 13 FTIR Spectra of the functionalized AFM probes. Graphs showing FTIR spectra of the Si AFM probes modified with (A) APTMS, (B) CPTMS and (C) HDTMS, respectively.	43

Figure 14 Force-distance curves for the interactions between functionalized/non-functionalized probes and ZnO surfaces. Representative force-distance curves between the surfaces of (A) conventional hexagonal ZnO particles, and (B) ZnO nanorod particles, and the modified probes with NH ₂ , Cl, and CH ₃ terminals and the unmodified Si probe. The force curves were shifted in vertical axis for clarity of the plots.....	46
Figure 15 Adhesion energies of the interaction between AFM probes modified with (A) APTMS, (B) CPTMS, (C) HDTMS, and various ZnO surfaces. Results for interactions between unmodified Si AFM probes and ZnO surfaces are shown in (D).	53
Figure 16 Force-distance curves for the interactions between functionalized/non-functionalized probes and ZnO surfaces. Graphs showing the representative force-distance curves between the surfaces of (A) Zn-terminated face, and (B) O-terminated face of conventional hexagonal ZnO particles, and the probe modified with NH ₂ , Cl, and CH ₃ terminals as well as unmodified Si probe.....	56
Figure 17 Molecular structure, electronic distribution and normalized fractional charge of the AFM probe-functionalizing molecules: (A) APTMS, (B) CPTMS, and (C) HDTMS. Note that blue and red margins of the scale represent levels of maximal positive and negative charge density normalized within a given molecule, respectively.	64
Figure 18 Talc composition structure	76
Figure 19 AFM-probe surface modification with (A) 11-Mercaptoundecanoic acid and (B) HDTMS to form carbonyl (-COOH) and methyl (-CH ₃) groups on the outermost layer, respectively.	80
Figure 20 The representative SEM-micrographs and AFM topographic images of talc: (A and E) unmodified talcum powder, (B and F) acid treatment, (C and G) surface modified with APTMS and (D and H) surface modified with HDTMS, respectively. The color scale in E through H represents 0 nm (darkest) 850 nm (brightest).....	83
Figure 21 FTIR spectra of surface-modified talc in each condition.	87
Figure 22 High-energy resolution Si2p, O1s and Mg1s XPS spectra of talc particles after surface modification with (A) unmodified talc, (B) HCl treatment, (C) APTMS and (D) HDTMS.	88
Figure 23 Surface affinity test of (a) unmodified talc particles, (b) HCl-treated talc, (c) APTMS-grafted talc and (d) HDTMS-grafted talc.....	90

Figure 24 The representative force-distance curves between unmodified/modified talc particles and (A) silicon and (B) diamond-like carbon (DLC) probe.....	94
Figure 25 Histogram represent the bimodal fashion of the adhesion force obtained between Si /DLC tips and unmodified/modified talc particles.....	98
Figure 26 Adhesion forces of the interactions between functionalized/non-functionalized probes and modified talc particles with (a) APTMS and (b) HDTMS.	100
Figure 27 An example of the force and tip-sample separation (F-d) curve from the unmodified talc powder that interacted with the COOH-terminated probe.....	103



CHAPTER I

INTRODUCTION

The particles' adhesion on the substrate surface is among major concerns in many electronics industries such as mechanical parts, semiconductors, coating processes, and data storage industries [1]. The interference of contaminating particles that attach any electronic component within a product can significantly disrupt the entire system's function, leading to defective items and manufacturer's loss [2, 3]. Generated during the manufacturing process and taken in by workers when entering the manufacturing facility, these specks of atmospheric dust physically attract to or form chemical bonds with the part's surface. However, the prevention of physical attraction or chemical bonding has not been effectively achieved [4].

This work focuses on the microelectronic industry issue: adherent magnesium silicate or talcum particles on the insulating diamond-like carbon (DLC) layer on a silicon substrate or directly on the substrate. Unsurprisingly found as a contaminant in microelectronic circuits, talcum is a material used in a wide variety of industries, including cosmetics, construction, and metallurgy, filler, drug component, or even confectionery production (an anti-adhesive and an anti-caking agent) [4, 5]. In addition to the space-filling and strengthening application, a magnesium silicate can absorb both acid and alkali metal catalyst due to its high specific surface area [6, 7]. Free hydroxyl groups, the most reactive group on the magnesium silicate surface [8], provide the sites for physical adsorption of organic particles and quickly react chemically with multiple

substances [9]. Simple water or solvent cleaning cannot remove talcum from the surface because it is soft and insoluble in water or ethanol [10].

Consequently, an understanding of its adhesion mechanism on the metallic surfaces would allow us to devise effective methods to eliminate the small particles from the solid surfaces of microelectronic relevance. A perspective in the adhesion mechanism's elucidation involves determining the interaction between both talcum and substrate; a few analytical techniques can achieve this. We proposed using Atomic Force Microscopy (AFM), a scanning probe technique that performs a raster scanning of the tip that the cantilever's end on the sample surface. The interaction between the tip and the surface causes the cantilever to deflect. The cantilever deflection reflects a laser beam incident on the cantilever's back to a photosensitive diode detector, which measures the deviations and interprets them as the small interaction force (in pN to nN) that depends on tip-sample separation distance (in nm). In controlling this force to a setpoint value for each data point of scanning, it is possible to map the surface topography and other mechanical properties, e.g., elasticity [11, 12]. AFM has been employed in many fields such as nanomaterials, electronic parts, thin film growth, heterogeneous catalysis, and biological and biomedical research [13, 14].

In this dissertation, we used AFM to measure the interactions between particles and surfaces to investigate how the talcum particles adhere to the surface of interest. Besides, we explored the use of AFM to examine the interaction between ZnO particles (catalyst surface), another particle type with a more definitive surface controlled by synthetic methods, and the mimicked side chains of the toxic molecule in its heterogeneously photocatalytic degradation [15, 16].

Objectives of the research:

1. To study the interaction between magnesium silicate particles and DLC surface for understanding the adhesion mechanism.
2. To identify the dominant type of forces.

Scope of the research:

- The particles of interest that used in this research is composed of the commercial talcum powder ($3\text{MgO}\cdot 4\text{SiO}_2\cdot \text{H}_2\text{O}$), conventional ZnO particle (synthesized ZnO powder) and synthesized ZnO nanorods. Talc was chemically modified (acid treatment and silanization process) to improve the chemical property, and the adhesion force both before and after surface-modified talc needs to be investigated and compared.
- Both silicon sharp tip and the silicon coated with DLC tip were used in this work. For surface topographic images, AFM was operated in tapping mode while the adhesion measurements (force-distance curves) or the surface interaction forces were obtained from contact mode operation. Also, tip surface chemical functionalization will be done in order to investigate the specific molecular interactions.
- The adhesion behaviors were measured in ambient condition.

Expected benefits:

1. The experimental findings provide the comprehensive understanding the adhesion mechanism between particle and surface of interest.
2. This work is creative to design new materials or improve the new feature for industrial application.

CHAPTER II

THEORY AND LITERATURE REVIEWS

In this section, theory and literature review related to the fundamental of magnesium silicate, talcum, zinc oxide, particle adhesion forces and principle of AFM are described as follow.

2.1 Particles of interest

2.1.1 Magnesium silicate

Magnesium silicate is a compound of magnesium oxide (MgO) and silicon dioxide (SiO₂) in various fractions. It is the magnesium salt of silicic acid containing an unspecified amount of water (MgO•SiO₂•nH₂O). This compound occurs as a fine, white, odorless and tasteless which is synthesized by several methods such as precipitation, hydrothermal, mechano- chemical dehydration [17]. Generally, amorphous magnesium silicate undergoes transformation to different crystalline states upon thermal treatment. Regardless of the solubility characteristics, magnesium silicate is practically insoluble in ethanol, ether and water, but it is partially soluble in some strong acids [18]. Besides, it has high capacity to absorb paraffin oil and is used as industrial adsorbent as well. The surface of magnesium silicate carries free hydroxyl groups (silinol groups), which is the most reactive groups on the surface. They provide the sites for physical adsorption of organic particles and can easily react chemically with multiple substances. In terms of substituting with new atom groups, its provides potential for surface modification and exhibit tendency to adsorb on their surface

various compounds [19]. The surface composition of magnesium silicate can be shown in Fig.1.

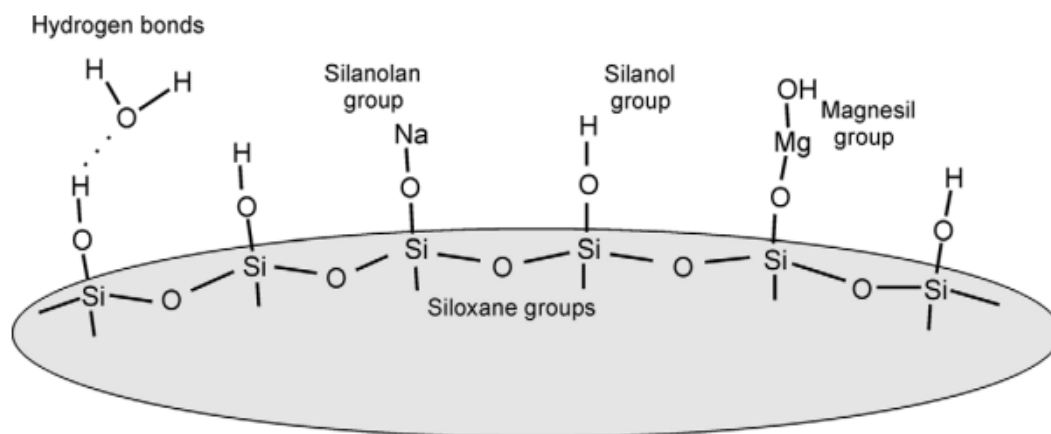


Figure 1 Magnesium silicate surface [8].

Magnesium silicate represents the most important materials in the pharmaceutical, food, and cosmetics industries. It could be used as a filler and pigment in dispersive paints, as an adsorbent in affinity chromatography. In addition, magnesium silicate is also used in the production of confectionary as an anti-adhesive and anti-caking agent [20]. In terms of particle morphology, magnesium silicate displays both primary and secondary particles. Not only exhibit a smooth surface or spherical shapes but also show a small diameter or no sharp edges. The particle size distribution was reported with many bands which depending on the type of magnesium salt that used in preparation methods. Generally, magnesium silicate that exposed to temperatures of 750 °C transforms from amorphous form to the magnesium silicate minerals enstatite (MgSiO_3) and forsterite (Mg_2SiO_4) [21]. When the temperature reaches 1100 °C and above, other polymorphs are formed. However, when magnesium silicate is kept in double-distilled, deionized water for 6 months at 85 °C, it maintains amorphous structure. This work uses two types of magnesium silicate including talcum

and forsterite mineral which are important in many applications. Each of the particles have specific properties as followed:

Firstly, talc is a naturally occurring mineral, mined from the earth, finely powdered and grayish white in color. Generally, talc is composed of magnesium, silicon, oxygen and hydrogen. Chemically, it is a hydrous magnesium silicate with a chemical formula of $\text{H}_2\text{Mg}_3(\text{SiO}_3)_4$ or $\text{Mg}_3\text{Si}_4\text{O}_{10}(\text{OH})_2$. As a pure mineral, the elemental composition of talc is SiO_2 63.5%, MgO 31.7%, and H_2O 4.8%. It corresponds to a formula weight of 393.3 g/mol, specific gravity of 2.7 to 2.8 and a melting point of 900 °C to 1000 °C [22]. For commercial grade, talc is produced by open pit or underground mining of talc rocks and processed by crushing, drying, and milling. The other minerals contamination including iron, nickel, manganese, chromium, aluminum, and titanium are separated from talc by flotation or elutriation. Geological formation of talc rock results from the alteration of magnesia and silica under the main parameters are temperatures and pressures. The hydrothermal alterations may lead to the other mineral phases such as tremolite and serpentine minerals, including chrysotile [23].

Talc powder is extensively used as filler for plastic, in the cosmetic industry in face, body, and foot powders, starch or boric acid, for medicine and toiletry preparations. In addition, it is also used as an additive to clay in ceramic manufacture and consumer products. The specific properties of talc such as hydrophobicity, and inertness are also well established and beneficial in wet environment. This material is thermally stable up to 900 °C and inert in most chemical reagents [24]. Initially, the unit cell of talc was studied and reported to be monoclinic, but further studies have

concluded that the unit cell is triclinic [25]. The crystal structure of talc is shown as Fig.2. The material is composed of a brucite (MgO) sheet between silicon-oxygen layers, each layer is electrically neutral and weakly bonded together, especially under shear deformation. Complexes of silicon oxide groups form layers of planar lattices in which each tetrahedron shares three corners with the adjacent tetrahedrons. Therefore, three oxygen atoms of each tetrahedron belong simultaneously to two silicon atoms, while the fourth oxygen atom belongs to one tetrahedron only.

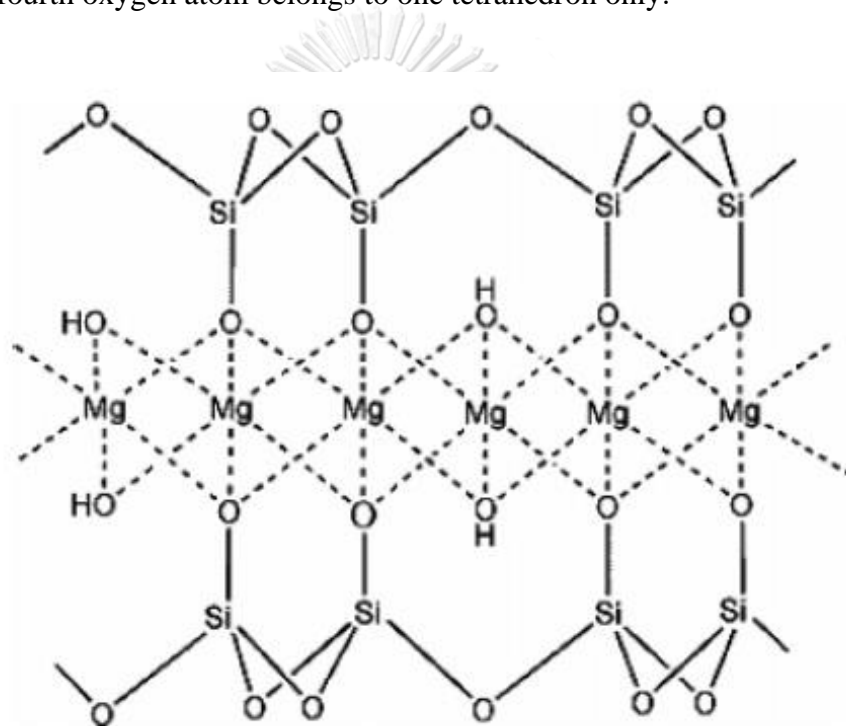


Figure 2 Crystal structure of talc [26].

Moreover, it well known that talc is the softest mineral with a hardness of 1-1.5 on the Mohs' scale. The surface properties seem to be a slippery feel, which depends on the source of the talc material. It is a fatty substance to the touch and a bad electrical and thermal conductor. As for the particle morphology, there is a variety of shapes, which depends on the sources of talc and methods for preparation. However, the majority of particle is displayed of smaller crystals growing on the surface when viewed

at least 3000x. The average particle size distributions were also found to be less than 15 μm , depending on the source of talc.

2.1.2 Zinc oxide (ZnO)

Zinc oxide (ZnO) has a broad range of applications, e.g., gas sensing, solar cells, micro-electronic devices, light emitting diodes, photocatalysts, due to its wide band gap and high transparency [27, 28]. ZnO can exist in different crystal structures and surface morphologies, depending on the synthesizing methods. ZnO is nearly insoluble in water or alcohol, but it is soluble in acids and alkalis. It exhibits excellent piezoelectric, optical properties and stability

Generally, the hexagonal wurtzite structure of ZnO is known as the thermodynamically stable phase under ambient conditions [29]. There is a semiconductive transition metal oxide with well-defined sizes, structures and shapes which have been extensively developed for various reactions. Presently, ZnO nanostructure exhibit interesting properties including high catalytic efficiency and strong adsorption. It is able to degrade a wide range of recalcitrant organic and inorganic pollutants due to its ability to generate highly oxidizing and reducing species [30]. Multiple low-Miller indexed surface of ZnO particles exposed to toxic substances have been found to influence the adsorption as well as its photodegradation, apart from activities relevant to photogenerated charge carriers. Two forms of ZnO, i.e., conventional particles with zinc- and oxygen- terminated polar surfaces as the dominating planes, and nanorods with mixed-terminated

In this work, the use of ZnO as a catalyst for degradation wastewater pollutants through photocatalytic oxidation process was emphasized. The effect of adsorption and

degradation on different surfaces of ZnO have been reported in the previous investigations [31]. The many results indicated that the exposing surface of ZnO and types of molecule to interact with its surface are importance key on the degradation pathway. Interestingly, the multiple facets of ZnO directly affect the interactions between molecules and surface of catalyst during the reaction. The atomic arrangements and electronic structure in each plane have been found to affect the adsorption mechanism and catalytic activity [32]. Molecular configurations of diuron adsorbed on the three ZnO particle surfaces determined by the density functional theory (DFT) calculation were found to be surface-dependent [33]. The configurations allowed us to conjecture about specific molecular portion within a diuron likely to be attacked by hydroxyl radicals to form a specific intermediate based preferentially on the exposed ZnO facets. However, the insight into the molecular arrangement and interaction of the pollutants during adsorption on different ZnO particle surfaces would necessitate quantitative verifications using appropriate surface characterization techniques/methods [34].

2.2 Principle of AFM analysis

The atomic force microscope (AFM) is not only a tool for high-resolution imaging of the topography of solid surfaces, but also a powerful instrument for measuring the force-versus-distance curves. The study of interaction forces with the AFM has led to deeper understanding of many biological and physical processes down to single molecule level [35]. It is essential to provide the information of local material properties such as hardness, elasticity, adhesion and surface charge densities [36]. This technique is not only used to measure the small samples but also reduced the danger of

contamination and surface roughness due to small of contact areas. The schematic representation of AFM is shown in Fig.3.

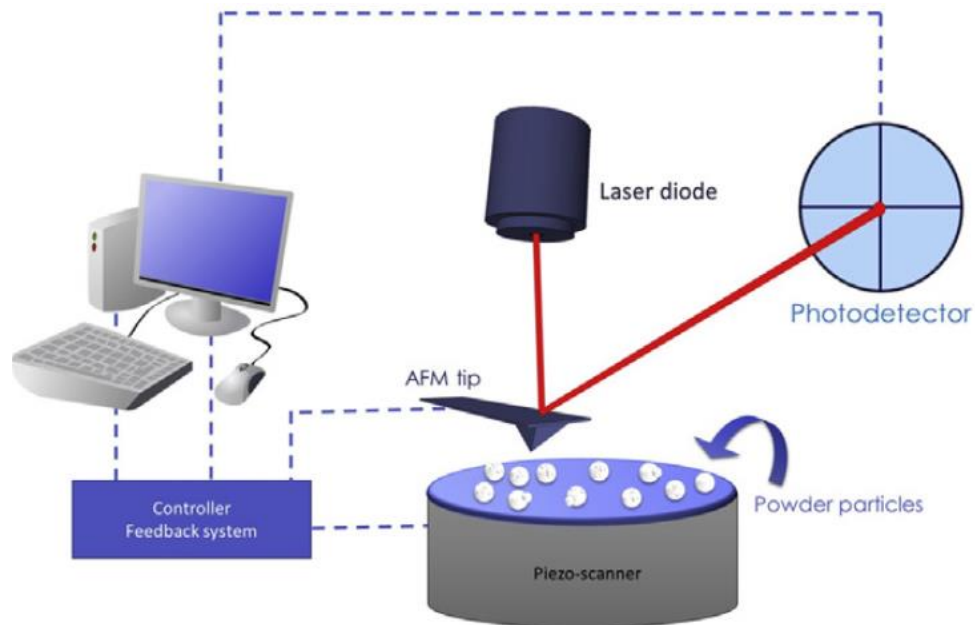


Figure 3 Schematic representation of atomic force microscope [37].

Mostly, the AFM is usually operated to work in two different mode as contact and tapping mode. These modes use different contact forces on the cantilever depending on the interaction between the tip and sample. In tapping mode, the cantilever is oscillated on sample surface at resonant frequency and usually scanned over the surface to produce image in three dimensions. While the contact mode both the AFM probe and sample surface come in to with separation distance less than 0.5 nm. However, the AFM tip is able to investigate an extremely small interaction area (using tip radius in the range of 5-50 μm), and this gives it a high sensitivity to small forces [38]. This technical report introduces the data collected in force curves and the standard steps that used in converting the data for a quantitative force analysis. The direct result of force measurement is the photodiode current (I_{PSD}) and height position of the piezoelectric

translator (Z_p) [39]. It can be converted this information into force and distance curve as seen in Fig.4.

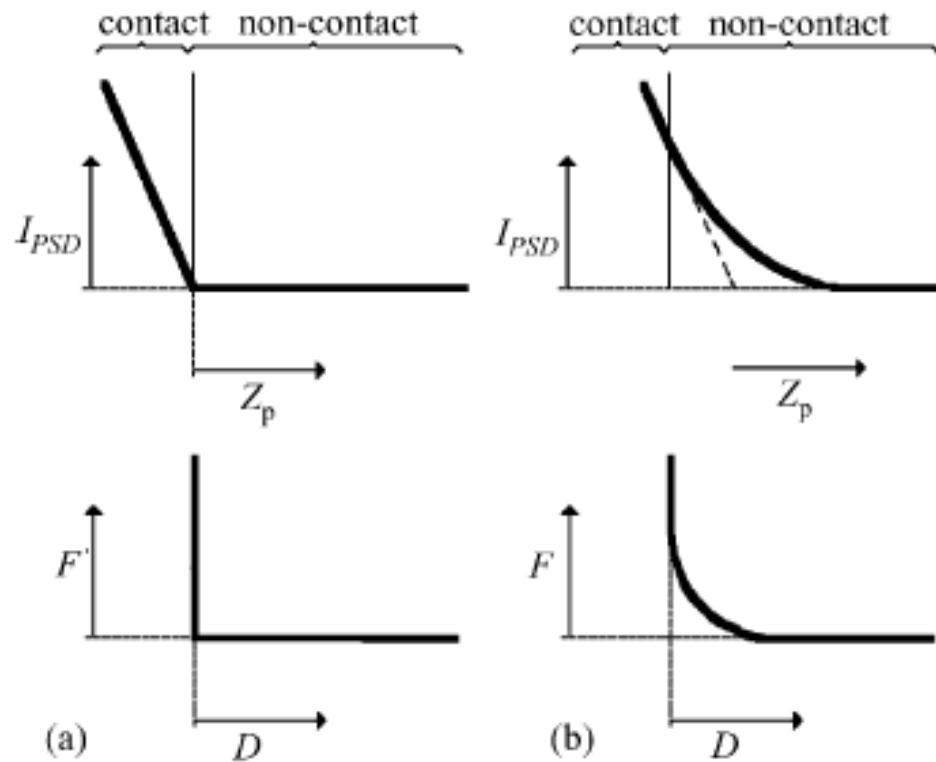


Figure 4 The characteristic of I_{PSD} vs. Z_p curves are converted to force vs. distance curves when (a) for hard tip and sample without surface forces and (b) hard materials with a long-range repulsion [40].

In force spectroscopy measurement, the movement of the cantilever and tip during the force spectroscopy measurement in contact mode is shown in Fig.5. Point (a) the sample is initially far away from the probe, the cantilever is at an equilibrium (zero cantilever deflection) and no measurable interaction between them. Upon approaching the surface, the cantilever moves downward to the sample, resulting in the “jump to contact” is observed at point (b). If the attractive force of the tip-sample interaction exceeds the normal spring constant of the cantilever, the tip will be snap into

contact with the sample. Point (b) to (c) displays the increasing of tip-sample interaction, the sample moves upward until a predetermined maximum normal load is reached. The retraction of the sample will lead to the decrease in the interaction, the tip keeps in contact with the sample because of the adhesion, and the maximum adhesion force was detected at point (d). When the normal spring constant overcomes the attractive force gradient, the cantilever snaps back to its original position [41].

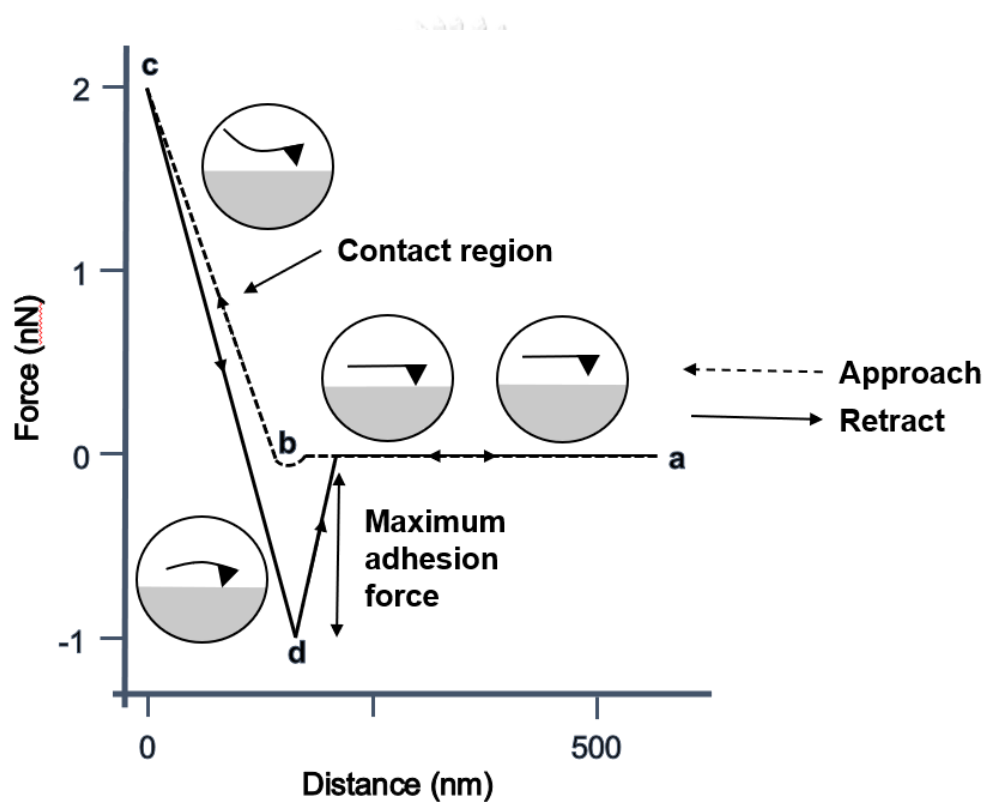


Figure 5 Schematic diagram of the cantilever and tip movement during the approach and retract parts of a force spectroscopy experiment.

Normally, the force profiles can be indicated that if the sample and/or tip are soft surfaces the force curve is in general not linear anymore. The deformation region will be appearing. Such soft samples include for example cells, bubbles, or microcapsules and the soft surface such as the flexible polymers etc. However, for hard

surface materials, the obtained force curve is certainly linear. The appearance of adhesion will be observed when contact is established, due to the participation of surface forces (van der Waals). Table 1 summarizes of the interactions that have been measured using the AFM.

To date, force curves are used by many researchers to characterize materials and single molecules. The measurement may be repeated at different locations to build up a map of the tip-surface interaction, or can be repeated at the same point to give a full statistical understanding of the interaction [42]. Additionally, this technique can be analyzed the force curve in different conditions such as in liquid, vacuum and ambient air.

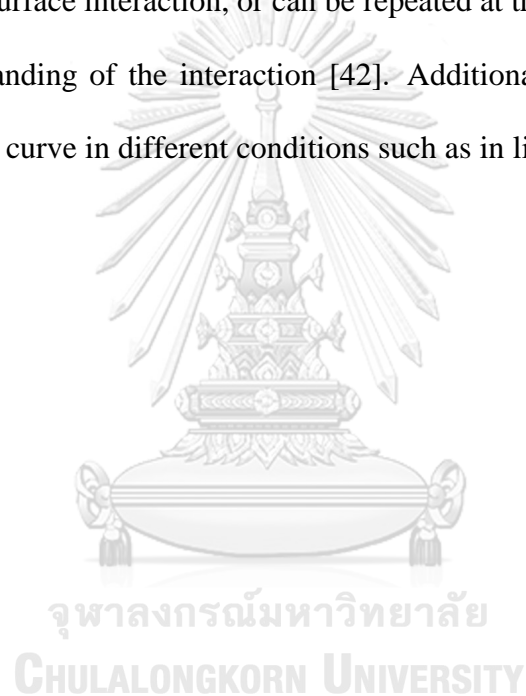


Table 1 gives a summary of interactions that have been measured using the AFM

Step	The movement	Interaction
APPROACH	Tip far away 10-100microns	<ul style="list-style-type: none"> ▪ No interaction
	Tip approaching few microns	<ul style="list-style-type: none"> ▪ Electrostatic forces ▪ Long-range interactions from adsorbed molecules.
	Tip close to surface nanometers to atomic distances	<ul style="list-style-type: none"> ▪ Van der Waals ▪ Capillary forces in air ▪ Chemical potential ▪ Magnetic
CONTACT	Tip indenting sample	<ul style="list-style-type: none"> ▪ Stiffness Young's modulus, elastic response ▪ Viscoelastic response variable rates or indentation depth
RETRACT	Tip lifting off surface few atomic distances to nanometers	<ul style="list-style-type: none"> ▪ Adhesion
	Tip further away nanometers to hundreds of nanometers	<ul style="list-style-type: none"> ▪ Stretched molecules between tip and surface.
	Tip far from surface 1-5 microns	<ul style="list-style-type: none"> ▪ Connections broken between the tip and surface, no further interaction. ▪ Adhesion strength can be measured between attached molecules and the surface when the attachments break.

2.3 Particle adhesion theory

Particle adhesion phenomena played a role in a variety of scientific and engineering applications. Particles are deposited on the surfaces by combined action of diffusion, sedimentation and other factors such as electrical charges and local electrostatic fields. Adhesion of particles to such surface as well as to other surfaces in production environments need to be understood. Because the effective ways for preventing and cleaning contaminated surfaces may be created [43]. Currently, contamination of product surfaces by particles during the process leading to significant losses of product yield and reliability. Many industries are becoming a concern of this problem, especially, microelectronic manufacturing. Generally, adhesive forces result from molecular and electrostatic interaction and are influenced by the surrounding medium and the composition. Although the adhesion of solid particles on the solid surfaces is commonly found, the small particles adhesion and adhesive force are not well defined. Therefore, in this section drawn the force of adhesion which related to small particle as follow:

2.3.1 Van der Waals forces

The vdW interaction, the ubiquitous intermolecular attraction between macroscopic bodies [44], played an important role in our observed adhesion phenomena (in the absence of external electric/magnetic fields). Originated from electrodynamic interactions between atomic or molecular dipoles within the interacting entities, the vdW potential comprises three components based on whether the dipoles are instantaneous/induced (associated with nonpolar molecules) or permanent (associated with polar molecules): Keesom interaction (permanent dipoles Vs. permanent dipoles),

Debye interaction (permanent dipoles Vs. induced dipoles), and London or dispersion interaction (induced dipoles Vs. induced dipoles) [45]. These forces are the attraction forces between atom or molecule, related to material composition or physical appearance. The interaction between solid bodies can simply be calculated by using the principle of molecular interactions, which depends on particle-surface geometries. As a result, the relationships of interactions force in various surfaces are following.

$$F = \frac{AR}{6d^2}$$

Where A is a material constant (the Hamaker constant), R is the radius of contact and d is a separation distance. In case of the van der Waals interaction for identical materials, in vacuum and in another medium, is always attractive [46].

2.3.2 Electrostatic forces in vacuum and air

In gaseous environments, two types of electrostatic interactions may cause increased particle adhesion. The first type arises when the difference in the work functions of two different materials resulting in a contact potential. When two solids are separated by a small gap, electrons from the material with the lower work function are transferred to the material with the higher one. The other electrostatic interaction occurs due to the electric charge on particle or the substrate surface. Sometimes, electrostatic forces may be induced by polarization. If a charged particle is at a distance from an uncharged surface, the charged particle will induce an equal charge of opposite sign within the material also at a distance from the surface [24]. The attractive force can be calculated as followed

$$F_{At} = \frac{q^2}{4R^2}$$

Where q is the charge of particle and $2R$ the distance between the charge centers.

2.3.3 Effect of relative humidity on adhesion

Adhesion of particles of many materials to solid surfaces, but variation in adhesion with relative humidity was not consistent. It is obvious from many research discussion that relative humidity of the ambient air should strongly influence the adhesion of solid particles to solid surfaces [47]. The equation has been found approximately as followed.

$$F = [75 + 0.68(\%RH)]d$$

Where $\%RH$ is the percentage relative humidity and d is the particle diameter in centimeters, giving a force in dynes. This equation is for hard materials and clean surfaces in air. Because the humidity of the ambient air is adsorbed at particle surfaces, these surface layers increase condensed water in the contact zone. The effect of water meniscus that are formed between two surfaces is also reduced because the relative humidity (RH) was maintained under the critical values of 40%, reported to give rise to an additional attraction [48].

2.3.4 Effect of contact area on adhesion

In terms of particle size, the adhesion forces increase with particle size, generally. For removing, larger particles were easier to eliminate than smaller particle retained on the surface by lower adhesion forces. Because the smaller particles can be

agglutinated together, even at low relative humidity, while the greater particles ran free [49].

In addition, many studies investigated the effect of surface roughness on adhesion. The results indicated that the adhesion forces decrease with increasing surface roughness. Since, it is decreasing of the real contact area between solid surfaces. The effective contact area is increased and may result in increased adhesion. Likewise, some research believed to be due to the presence of electrostatic charge [50].

2.3.5 Effect of temperature on adhesion

In terms of the micro- nanoelectromechanical system, the adhesion force becomes mainly dominant. The temperature is one of the most important effect on the adhesion force. Many studies have been reported that the mean adhesion force first increases with the increase in temperature under ambient air and the temperature below 100 °C. The increase in adhesion is associated with the capillary force. At high temperature, the adhesion force tends to decline and remains stable. It is believed that the increasing temperature resulting in broke the van der Waals bonds [51].

2.4 Adhesion measurement and control

This section was collected the previous investigations on the adhesion measurement with various conditions. Also, the effective ways to remove the particles in recent years will be established. Particle-surface adhesion forces is required an understanding for a lot of technologies. Several researchers are greatly interesting because of its necessary for industrial applications. The most significant viewpoint in particle adhesion will be described as followed.

Cher Lin Clara Tan et al. (2014) studied the adhesion of dust particles to common indoor surfaces in an air-conditioned environment. They use the polyvinyl chloride (PVC) sheet, microscope glass slide, aluminum foil and copper tape as substrate materials. The actual dust particles were deposited via vacuuming on the substrates before attachment to AFM cantilevers. The adhesion forces were measured the deflection by AFM technique. Also, the effect of surface roughness in each substrate was considered. The result indicated that van der Waals forces are primarily predominant in adhesion of dust and activated carbon. If the materials are non-electrical conductor, the electrostatic force is significantly presented. In addition, the surface roughness has strongly affect the adhesion due to involving with contact area between AFM tip and particles [46]. However, adhesion reduction was investigated by many ways. For example, TIANMAO LAI et al. (2016) reported that coating surface materials with thin organic films, fluorocarbon films and DLC film can be used to reduce the adhesion. In this paper, the effect of reducing adhesion force by the DLC film coating which were studied by recording F/D curves with an AFM. The tip shapes are different contact geometries including a flat tip, a sharp tip and spherical tip. The results can be concluded that the surface roughness also takes effect on reducing the adhesion force. Also, the DLC film plays a role in reducing the wear, tear and decreasing surface energy [52]. Besides, adhesion reduction can be done by surface charged neutralization. Hans-Jurgen Butt et al. (1991) investigated electrostatic interaction in water. They pointed out that in an aqueous medium the electrostatic forces should be considered. Because the most of surface are charged, which results from the dissociation of surface groups or the adsorption of ions onto the surface. Naturally, the electrostatic force is repulsive, it depends on the distance between particle and surface

as well as electrolyte. The results suggested that the adhesion forces can be decreased when increasing salt concentrations due to reducing the electrostatic force.

Additionally, the adhesion forces can be achieved by chemical surface modification of surface. In terms of using an AFM to study the single molecular interactions, chemically modified AFM tips has been growing interest. In Force Microscopy, AFM probes are functionalized to make them sensitive to a specific molecular interaction as well as to improve tip parameters and enhance the tip efficiency. Functionalization of AFM tips with Self-Assembled Monolayer (SAMs) is the common method for surface modification which relies on the chemical reaction of functional groups on the surface of the silicon tip with a various compound to form covalent bonds. This strategy is usually applied for modified a tip with only one molecule probe such as silanization reaction, as seen in Fig.6. This method can be developed the tip to high sensitivity for measurement the single molecule and to specific samples. However, the strategies for modifying the surface with some functionalization can be done via many ways such as adsorption or an electrografting process [53].

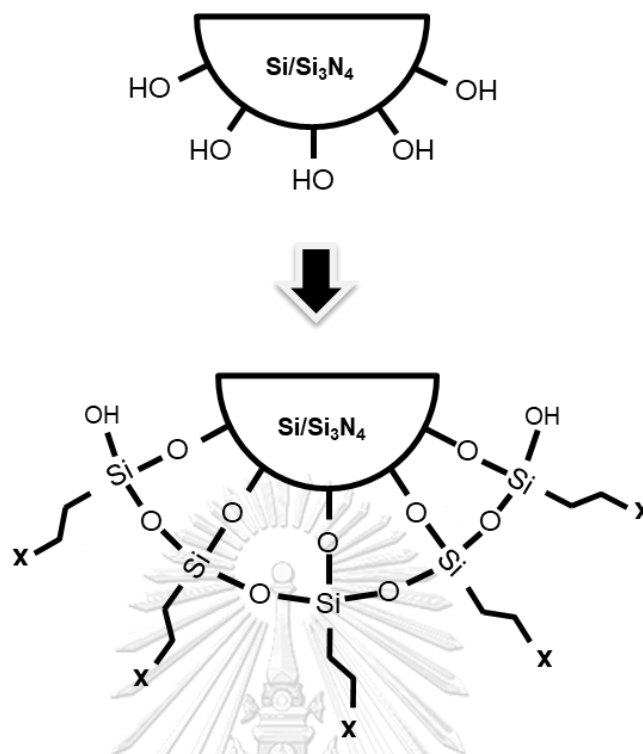


Figure 6 Schematic drawing of a chemically modified tip with functional groups X that provide a specific interaction on the sample surface.

In addition, surface modification methods are also used to study the molecular interaction in liquid medium. Vezenov et al. (2012) studied the simple of methods for functionalization to attach the surface. Immobilization of molecules is one of the most effective ways to introduce chemical groups. For example, immersing target sample into the different variant of reagent (different pH values). The surface was functionalized with some groups (-COOH, -CH₃, -OH, and -CH₂-OH) leading to directly affected the adhesion forces, especially working in liquid. The surface charged can be highly changed when using different pH as shown in Fig.7.

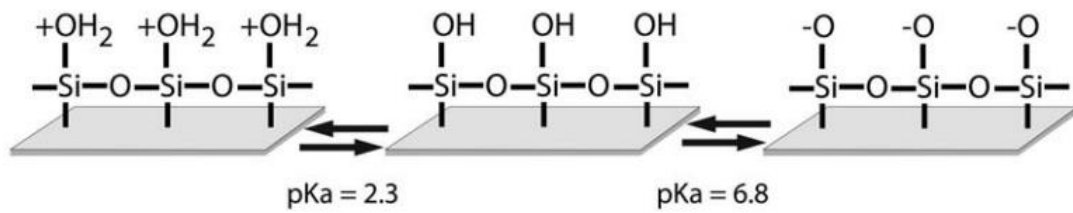


Figure 7 Change in charge depending on pH of the buffer [54].

Adhesion forces can be changed by the effect of chemical composition on the surfaces. Because a part of the surface will be covered by the new receptor or ligand molecules [54]. All of the studies should be noted that the interaction of individual molecule can be investigated by AFM technique as compared to other method. Because of its ability to control the loading or group of the participants by several strategies.

CHAPTER III

**EFFECTS OF CATALYST SURFACES ON ADSORPTION
REVEALED BY ATOMIC FORCE MICROSCOPE FORCE
SPECTROSCOPY: PHOTOCATALYTIC DEGRADATION OF
DIURON OVER ZINC OXIDE**

*Vipada Dokmai^a, Worasom Kundhikanjana^b, Narong Chanlek^c, Kitiphat
Sinthiptharakoon^d, Udom Sae-Ueng^e, Witchukorn Phuthong^{*f} and Varong
Pavarajarn^{*g}*

^a Center of Excellence in Particle and Materials Processing Technology, Department of Chemical Engineering, Faculty of Engineering, Chulalongkorn University, Bangkok 10330, Thailand

^b School of Physics, Institute of Science, Suranaree University of Technology, Nakhon Ratchasima 30000, Thailand

^c Synchrotron Light Research Institute (Public Organization), Nakhon Ratchasima 30000, Thailand

^d National Nanotechnology Center (NANOTEC), National Science and Technology Development Agency (NSTDA), 111 Thailand Science Park, Phahonyothin Road, Khlong Nueng, Khlong Luang, Phatum Thani 12120, Thailand

^e National Center for Genetic Engineering and Biotechnology (BIOTEC), National Science and Technology Development Agency (NSTDA), 113 Thailand Science Park, Phahonyothin Road, Khlong Nueng, Khlong Luang, Phatum Thani 12120, Thailand

^f Department of Physics, Faculty of Science, Kasetsart University, Ladyao, Chatuchak, Bangkok 10900, Thailand

KEYWORDS: Force spectroscopy, Atomic force microscopy, Adsorption, Photocatalytic degradation, Diuron, Zinc oxide

Published: 20 Jun 2020, Phys. Chem. Chem. Phys., 2020, 22, 15035-15047

ABSTRACT: Controlling adsorption of a heterogeneous catalyst requires a detailed understanding of the interactions between reactant molecules and the catalyst surface. Various characteristics relevant to adsorption have been theoretically predicted but have yet to be experimentally quantified. Here, we explore a model reaction based on diuron [3-(3,4-dichlorophenyl)-1,1-dimethylurea] photo-degradation over a ZnO particle catalyst. We used atomic force microscope (AFM)-based force spectroscopy under ambient conditions to investigate interactions between individual functional groups of diuron (NH₂, Cl, and CH₃) and surfaces of ZnO particles (polar Zn and O-terminated, and nonpolar Zn-O terminated). We were able to distinguish and identify the two polar surfaces of conventional ZnO particles and the nonpolar surface of ZnO nanorods based on force-distance curves of functionalized probe/surface pairs. We posit that the reaction involved physisorption and could be described in terms of Hamaker constants. These constants had an order-of-magnitude difference among the

probe/surface interacting pairs based on polarity. Hence, we confirmed that van der Waals interactions determined the adsorption behavior. We interpreted the electronic distribution models of the probe-modifying molecules. The functional group configurations inferred the diuron adsorption configurations during contact with each ZnO facet. The adsorption affected characteristics of the reaction intermediates and the rate of degradation.

3.1 INTRODUCTION

More than 60% of industrial catalytic processes are based on heterogeneous catalysts, which allow for convenient separation of the catalyst from the product stream. Hence, this feature has enabled the development of straightforward continuous chemical processes. In basic heterogeneous catalytic reactions, liquid reactants first adsorb to solid catalyst surfaces, react, and transform into liquid products. The products then desorb from the catalyst into the fluid phase. Additional steps are associated with absorption and transfer of light energy in semiconducting materials; hence, heterogeneous photocatalysis is a complex oxidation process based on oxidation of adsorbed species by highly active hydroxyl radicals. These radicals are produced from reactions between photogenerated holes (h^+), which are formed when a semiconducting catalyst is irradiated with a light having an energy higher than its bandgap [55] and water surrounding the catalyst [56]. However, in considering the steps both before and after charge transfer, the adsorption of reactants onto the surface of the catalyst is a rate-limiting step for many heterogeneous photocatalysts. Therefore, several systematic studies for a given reaction are required to understand atomic/molecular interactions at adsorption sites to design catalysts that can precisely control the reaction. It was found

by synchrotron-radiation-based infrared nanospectroscopy that the oxidation and reduction activity of a catalyst correlates with particle regions [57]. A high amount of active edges intentionally created on a catalyst have also proven to effectively improve its catalytic activity [58].

Among various heterogeneous photocatalytic reactions, the degradation of diuron [3-(3,4-dichlorophenyl)-1,1-dimethyl urea] was selected as a reaction model in this work for two reasons. First, diuron is a highly toxic agricultural herbicide pollutant with a long half-life in water [59]. Second, reactions arising from different catalyst/reactant interactions generate intermediates that have different toxicities. Some intermediates, such as 3-(3,4-dichloro-hydroxyphenyl)-1-(dihydroxymethyl)-1-methylurea, are potentially more toxic than their parent compounds [60]. This degradation can be photocatalyzed by zinc oxide (ZnO) particles, a common metal oxide photocatalyst. The size, structure, and shape (e.g. nanoplates, dumbbell microrods) of ZnO particles can be controlled by a variety of synthetic methods [61-63]. ZnO single crystals, microparticles and nanoparticles have a hexagonal wurtzite structure, which is a thermodynamically stable phase under ambient conditions [64]. Multiple low-Miller indexed surfaces of ZnO particles exposed to diuron have been found to influence adsorption and photodegradation of reactants and activities of photogenerated charge carriers. Two forms of ZnO have been shown to produce different degradation intermediates, namely conventional particles with either zinc- or oxygen- terminated polar surfaces and nanorods with mixed-terminated nonpolar surfaces [60]. Differences in the molecular configurations of diuron adsorbed on these three types of ZnO particle surfaces have been determined by density functional theory (DFT) calculations. Different functional groups within a diuron molecule align

differently towards various facets of the two ZnO particle types. These configurations led us to consider the specific parts of diuron molecules likely to be attacked by hydroxyl radicals and preferentially form specific intermediates. To gain insight into the molecular arrangement and interactions of diurons during adsorption on different ZnO particle surfaces requires quantitative studies by appropriate surface characterization methods [65].

The origins of the interactions within the surface of ZnO, for both single crystal and nanoparticles, have been experimentally examined by several techniques, such as scanning probe microscope (STM) methods. Four low Miller indexed surfaces — (0001), (000 $\bar{1}$), (10 $\bar{1}$ 0), and (11 $\bar{2}$ 0) of single crystal ZnO have been successfully imaged by STM, although these have been hindered by low sample conductivity [66, 67]. In addition to information about electronic states, STM investigations have yielded insights into the ZnO local surface structure and defects e.g., atomic terraces and step edges, at high precision [68, 69]. This method also allowed us to observe surface structures that appeared to have bulk-like termination at polar Zn-(0001) and O-(000 $\bar{1}$), surfaces [70, 71]. In addition to STM, dynamic scanning force microscopy (SFM), which is a kind of atomic force microscope (AFM) imaging mode has been used. The technique was used to examine the surface of polar Zn-(0001) facets, which also adopt a triangular surface reconstruction with long and parallel step edges and transition regions [72]. Despite the ability to obtain images at high resolution, the optimal operation conditions for STM and SFM mean that experiments must be performed in an ultrahigh vacuum, which is unlike the optimal working conditions of ZnO photocatalysts. In addition, to map the surface features of the ZnO nanoparticles at room temperature, surface defects (such as metal ion sites) can be viewed as Lewis acids

(electron acceptors) and Bronsted acids (proton donors). Molecular probe-assisted solid-state nuclear magnetic resonance (NMR) has recently been used to determine the concentration of surface oxygen vacancies and exposed Zn ions at acidic surface sites within various facets of ZnO nanoplates, nanorods, and nanopowders [73]. The methods yield information on type, strength, concentration, and distribution (on different facets/surfaces) of discrete acidic sites on ZnO photocatalysts. However, these techniques are not a direct measure of the degree of interaction during adsorption, which is also affected by the reactant molecules.

Notably, AFM-based force spectroscopy is suitable for application in any environment and can be used to determine interaction strengths between ‘molecules’, including organic and biomaterials, and chemically modified/unmodified ‘surfaces’ in their ideal/close-to-ideal working conditions [74, 75]. In this work, we used this technique to determine the strength of interactions between AFM probes functionalized with amine, chloride, and methyl groups to reflect the various functional groups of diuron. The molecular structure of diuron is shown in Fig.8. We examined the interactions of these functionalized probes with three main ‘surfaces’ of wurtzite ZnO particles, i.e., zinc-terminated (0001), oxygen-terminated (000 $\bar{1}$), and mixed-terminated (10 $\bar{1}$ 0) surfaces. We quantified the interactions, correlated them with the normalized electronic distribution of the probe-functionalizing molecules, and discuss these in the context of our previous DFT simulations and the obtained intermediates in our previous work [60]. Referring to diuron photodegradation based on ZnO particle catalysts as the reaction model, this technique might be extended to investigate adsorption in other heterogeneous reactions.

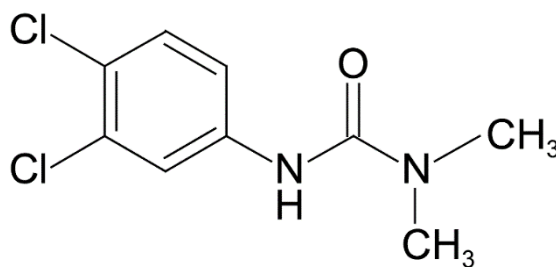


Figure 8 Molecular structure of diuron.

3.2 METHODOLOGY

3.2.1 Synthesis of ZnO particles

Conventional ZnO particles that have hexagonal faces were synthesized by a sol-gel method adapted from previous reports [76, 77]. The precursor solution was prepared by mixing 1.58 mL of diethanolamine, 0.25 mL of deionized water, 5 mL of ethanol and 0.18 mL of hydrochloric acid. Used as an acid-catalyzed sol, the zinc acetate solution was prepared by dissolving 3.29 g of zinc acetate ((CH₃COO)₂Zn•H₂O; Ajax Finechem Pty Ltd.) in 20 mL of ethanol at room temperature. The precursor was then gradually dropped to the turbid zinc acetate solution at room temperature with an airtight seal to prevent the evaporation of ethanol, and stirred gently until the solution became transparent. After that, the clear mixture was left to age for 24 hrs at room temperature before being dried in an oven at 80°C for 8 hrs to allow the mixture to transform into a solid gel. This gel was further aged at room temperature for 120 hrs to obtain the sufficient number of particles with complete hexagonal faces. The aged gel was then calcined at 600°C for 3 hrs in a furnace to obtain white powder.

ZnO nanorods were synthesized by a hydrothermal method modified from the previous work [78, 79]. First, the 27.5 % (w/v) zinc acetate solution was prepared by

dissolving zinc acetate in deionized water and stirred gently at room temperature. The precursor solution was then prepared by mixing 4 mL of the zinc acetate solution with 6 mL of 8 M sodium hydroxide aqueous solution. After that, 2 mL of the precursor solution was mixed with polyethyleneglycol (PEG, laboratory grade, Sigma-Aldrich) and 20 mL of ethanol to obtain the turbid solution. The mixture was transferred to a Teflon-liner of an autoclave reactor (for hydrothermal synthesis) before heating at 140°C for 1 hr under an autogenous pressure. After the reactor was cooled down at room temperature, the white precipitate was filtered and washed with ethanol. The precipitate was further washed with deionized water, and finally left to dry at 60°C for 8 hrs. It was proved that the obtained powder was as active as the conventional ZnO particles despite being prepared without calcination [60]. Morphologies of both powders were imaged with a field emission scanning electron microscope (FE-SEM, Carl Zeiss, AURIGA, Germany).

3.2.2 Sample preparation for AFM imaging and force spectroscopy

Owing to the particulate nature of the ZnO samples, several sample preparation steps were optimized to achieve good immobilization of both ZnO particles and minimal imaging of contaminants. For AFM measurements of conventional ZnO particles, 1-g portions of the powder were first dispersed by suspension in 10 mL of ethanol and sonicated for 2 h. Immediately after sonication, 2 μ L of the suspension was loaded onto a freshly cleaved mica substrate, which was heated to 70 °C, and then incubated further for 3 h at 70 °C in the same environment. The loaded particles were briefly sonicated (3–5 s) in deionized water to remove the excess particles that were potential contaminants and then dried at 100 °C for 30 min. For AFM imaging of the ZnO nanorods, the powder was deposited on the substrate by spin coating. First, a 0.5-

g portion of the ZnO nanorods was suspended in 10 mL of ethanol and sonicated for 30 min. Then, 1 mL of the suspension was dropped at a rate of 40 drop/min onto a silicon substrate that was previously attached to a custom-made rotating stage at a speed controlled by a regulated DC power supply. Finally, the sample was dried in an oven at 120 °C. During the process optimization and AFM experiments, the surface morphologies were examined by FE-SEM.

3.2.3 Chemical functionalization of AFM probe surface

We chemically modified AFM tips by a self-assembled monolayer (SAM) method, through which molecules of interest were deposited on the AFM tip, forming covalent bonds with the surface [80]. Three organosilane molecules were used to functionalize the silicon tips: 3-aminopropyltrimethoxysilane (APTMS, 97%, Aldrich) for amine (NH₂), 3-chloropropyl-trimethoxysilane (CPTMS, ≥ 97%, Aldrich) for chloride (Cl), and hexadecyltrimethoxysilane (HDTMS, ≥ 85%, Aldrich) for methyl (CH₃) groups. The molecular structures of these organosilane molecules are shown in Fig.9. This procedure consisted of two steps, i.e., pretreatment of the tip surface and silanization [81]; schematic diagrams of the tip after pretreatment and silanization are shown in Fig.12. A pretreatment was performed to remove organic contaminants and generate hydroxyl groups at the tip surface. In this step, the probes were washed with ethanol and deionized water, dried in an oven at 120 °C for 10 min, and then immersed in 0.5 M NaOH for 20 min, in 0.1 M HCl for 20 min, and in 0.5 M NaOH for 10 min. Afterwards, the tips were rinsed with 0.1 M HCl and deionized water and then dried in an oven at 120 °C for 10 min. The probes were additionally immersed in Piranha solution (7:3 concentrated H₂SO₄:30% H₂O₂) for 30 min, washed with deionized water several times, and left to dry in an oven at 120 °C for 10 min. In the silanization step,

the pretreated tips were immersed in the 5 mM of APTMS, HDTMS or CPTMS toluene solution (QR&C, Chem-Supply Pty Ltd.) for 12 h at room temperature and the lid was covered to prevent evaporation of toluene; this allowed the silane compounds to chemisorb to the tip surface. The probes were next washed with toluene twice to remove residual silane molecules that were weakly adsorbed to the probe surface. Then, the probes were rinsed twice with a mixture of toluene and ethanol (1:1) and with pure ethanol twice; this step was necessary to remove residual silane/toluene molecules from the probe [82]. Finally, the probes were dried in an oven for 20 min at 120 °C to complete formation of the thin layer.



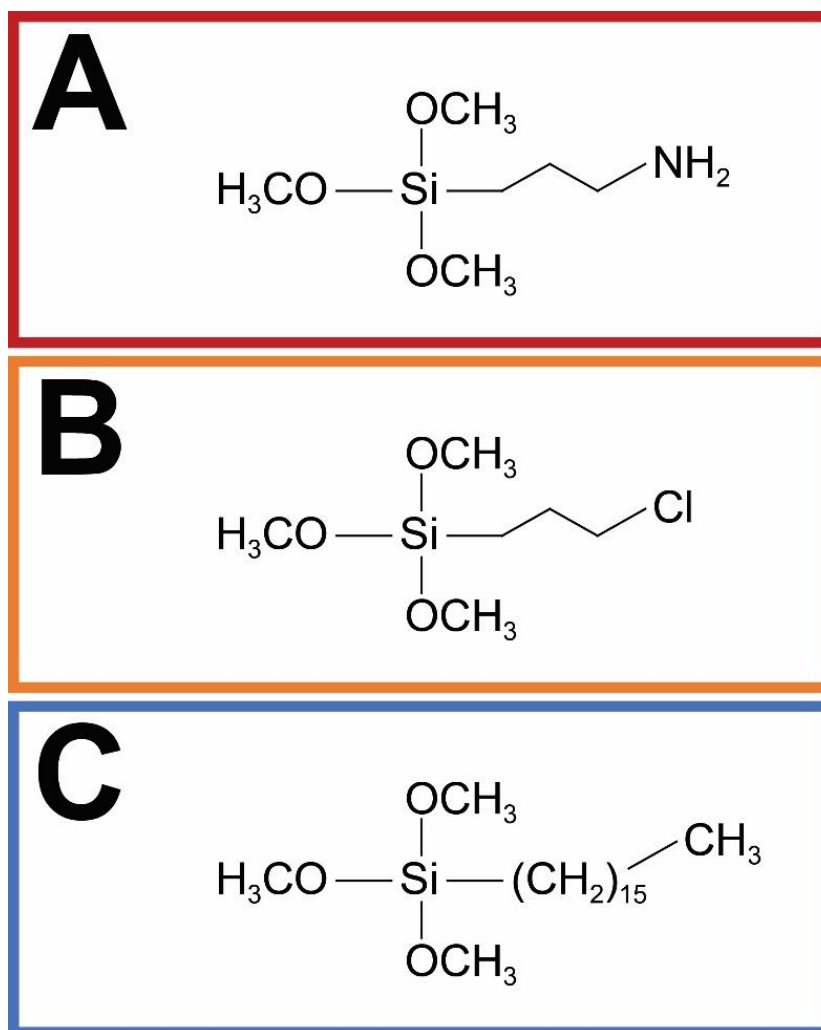


Figure 9 Molecular structures of APTMS (A), CPTMS (B), and HDTMS (C).

The elemental compositions on our functionalized coating were characterized by X-ray photoelectron spectroscopy (XPS, ULVAC-PHI, PHI 5000 VersaProbe II) with Al K α radiation (1486.6 eV) as the excitation source at the BL5.3 SUT-NANOTEC-SLRI joint research facility, Synchrotron Light Research Institute (SLRI), Thailand. It should be noted that the X-ray beam (10 μm in size) was focused on the cantilever of the AFM probe (50 μm in width and 450 μm in length). To confirm the nature of functional groups on the tip surface, attenuated total reflection (ATR-FTIR, Nicolet iN10, USA), was performed by pressing a microtip germanium (Ge) ATR

crystal onto the probe carrier in the area that had undergone the aforementioned pretreatment and silanization procedures.

3.2.4 AFM measurements and analyses

AFM imaging and force spectroscopy were performed using an XE-120, Park AFM, (Park Systems Corp., South Korea). For measurements of each tip/sample interacting pair, two types of AFM probes were used. First, topography images were obtained in non-contact mode with a tip (ACTA, Applied NanoStructures, USA) having a nominal radius of approximately 6 nm mounted on a silicon V-shaped cantilever with a spring constant of 56 N/m. All images were acquired under ambient conditions, at room temperature and atmospheric pressure at a scan rate of 0.20 Hz. The scan size used to locate the particles/particle clusters was approximately 4 μm x 4 μm for conventional ZnO particles, and 1 μm x 1 μm for ZnO nanorods. After the particle position on the substrate was determined, the probe was switched to a silicon tip (ContAl, Budget Sensors, Innovative Solutions Bulgaria Limited, Sofia, Bulgaria) with nominal spring constants in the range of 0.07-0.4 N/m. Through the use of a thermal tuning method, the modified and unmodified AFM probes were calibrated in air over a glass slide substrate at room temperature and their cantilever spring constants were determined. Images were obtained in contact mode to locate the ZnO surface based on their previously determined particle positions. Force versus cantilever displacement curves (or force curves) were acquired by recording the cantilever deflection while the sample surface was moved towards (approach curve) or away (retract curve) from the tip. In each acquired force curve, zero force was defined based on the portion of the curve where the separation between the tip and the sample was large and there was no detected deflection of the cantilever. We obtained 50 to 70 force curves from different

areas/particles within each type of ZnO particle surface to achieve good statistical validation. Throughout all AFM experiments, the relative humidity was controlled to be within $35 \pm 3\%$, and the temperature was maintained at $25 \pm 2^\circ\text{C}$.

3.2.5 Charge distribution model

The charge distributions on each single tip-functionlizing molecule (APTMS, CPTMS and HDTMS) were simulated using density functional theory calculations in the Dmol3 program in the Materials Studio 6.0 package. The generalized gradient approximation (GGA) with the Perdew-Wang 1991 (PW91) functional was used. A set of polarization functions (DNP) was set up as the basis set with the cutoff radius of 4.4 Å. The electron basis set was used for all elements. The maximum energy charge, the maximum force, and the maximum displacement were set at 1×10^{-5} Eh, 2×10^{-3} Eh/Å, and 5×10^{-3} Å, respectively.

3.3 RESULTS AND DISCUSSION

3.3.1 Characterization of ZnO particles

We used two synthesis methods to separately produce two types of ZnO particles in high purity, which were confirmed to be single crystals with hexagonal wurtzite structures by X-ray diffraction and high-resolution TEM imaging [83]. Each type of particle is associated with a unique dominating surface of specific Miller indices available for interactions: (1) Zn-(0001) or O-(000 $\bar{1}$), terminated surfaces from the hexagonal faces of the conventional ZnO particles obtained from the sol-gel method; and (2) Zn-O mixed-terminated (10 $\bar{1}$ 0) surface from the side facets of the relatively long cylindrical nanorods prepared by the hydrothermal method [84]. The Zn-(0001) and O-(000 $\bar{1}$),

terminated surfaces represent surfaces with uniformly dispersed and partial positive charges at Zn-ion lattice sites and partial negative charges at O-ion lattice sites. Conversely, the Zn-O mixed-terminated ($10\bar{1}0$) surface is a nonpolar surface owing to the zero effective charge resulting from alternating planes of Zn and O ions that stack along the c-axis (despite an approximate equal amount of Zn and O ions). The surface morphologies of the ZnO particles synthesized by the two different methods were examined by FE-SEM and AFM techniques. First, as shown in a representative SEM micrograph (Fig.10A), an AFM deflection image (Fig.10B; the corresponding topography image given in Fig.11), the conventional ZnO particles were octahedral, hexagonal based prisms. A distance across the hexagonal cross-sectional surface was determined as a height profile along the blue line in Fig.11B, resulting in a length of $\sim 2.6 \mu\text{m}$ that corresponds to a side length of $\sim 1.2 \mu\text{m}$ approximated using an ideal hexagon face. We expect that the hexagonal base of the remaining ZnO microprisms will expose either polar Zn-(0001) or the polar O-($000\bar{1}$), surfaces in the direction of growth, and their side facets are the Zn-O surface ($10\bar{1}0$). Many of the ZnO nanorods grew out of the nuclei (Fig.10C); however, we were able to obtain equivalent AFM images owing to the effects of the additional sample preparation steps. Since the small ZnO particles that were detrimental to AFM imaging (as imaging contaminants) tend to fall off the substrate in our extra steps of sample preparation, the hexagonally prismatic ZnO particles that are sufficiently large and strongly attached to the surface then allow us to resolve their particulate structure using AFM imaging. However, the octahedral particles only exhibit low aspect ratio which is the characteristic morphology of ZnO particles produced by the sol-gel

synthetic route that uses a short gel aging time (of ~ 5 days). We did not use AFM (or SEM) to study dimensions of the other six side-facets of these particles since they appeared to emanate from an original point in a cluster. Although increasing a gel aging time could result in a longer column of the prismatic particles as well as the side-facet area, we did not employ this method to study the side facet because the emanation of micrometer columns of the clustered particles is not suitable for AFM imaging [85]. Similar to the conventional ZnO particles, the emanating characteristics of the as-synthesized ZnO nanorods that were observed in the SEM micrograph (Fig.10C) would make it difficult to obtain meaningful AFM images. Therefore, for successful acquisition of the AFM images from the conventional ZnO powder, additional sonication to disperse the clustered ZnO nanorod particles before spin coating to attach the dispersed particles to the substrate were included in sample preparation. Consequently, the individual ZnO nanorods tended to lie horizontally and stack on one another due to surface energy minimization. This morphological study of conventional ZnO particles and nanorods allows us to control which surfaces of the ZnO particles are presented and their locations with respect to the modified/unmodified probes for the AFM-based force spectroscopy. In the representative topography image of the ZnO nanorods (shown in Fig.11D) corresponding to Fig.10D, a representative height profile, which is generated along a transect represented by a red line in Fig.11E. It should be noted that, according to SEM analyses based on 60 particles, the average size of the conventional ZnO particles was 1.14 μm with the standard deviation of 0.20 μm , measured from one side of the hexagon to the opposite side. For the nanorods, the average diameter and length were 52.4 and 216.3 nm,

with the standard deviation of 4.4 and 24.1 nm, respectively. The size distributions of the ZnO particles are shown in Fig. 3.4. Due to a geometrical inaccessibility of the AFM tip to the two hexagonal face of the nanorods, we only used AFM (or SEM) to determined dimensions of their height in the direction parallel to that of AFM tip approach/retract. The variation in size of the ZnO particles should not affect the AFM-based force spectroscopy results because size of the AFM tips (c.a. 10 nm) was much smaller than the size of the investigated facets.

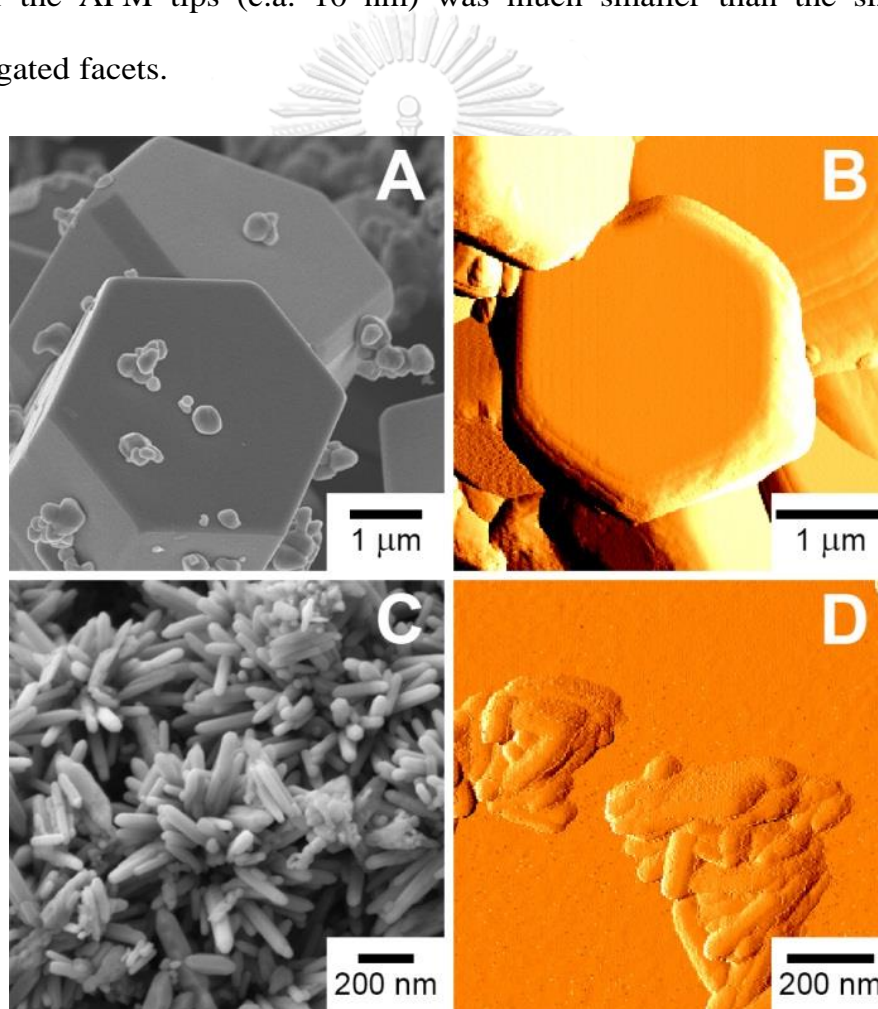


Figure 10 Morphology of ZnO particles. (A) and (C) SEM images, (B) and (D) AFM deflection images of conventional hexagonal ZnO particles and nanorod particles, respectively.

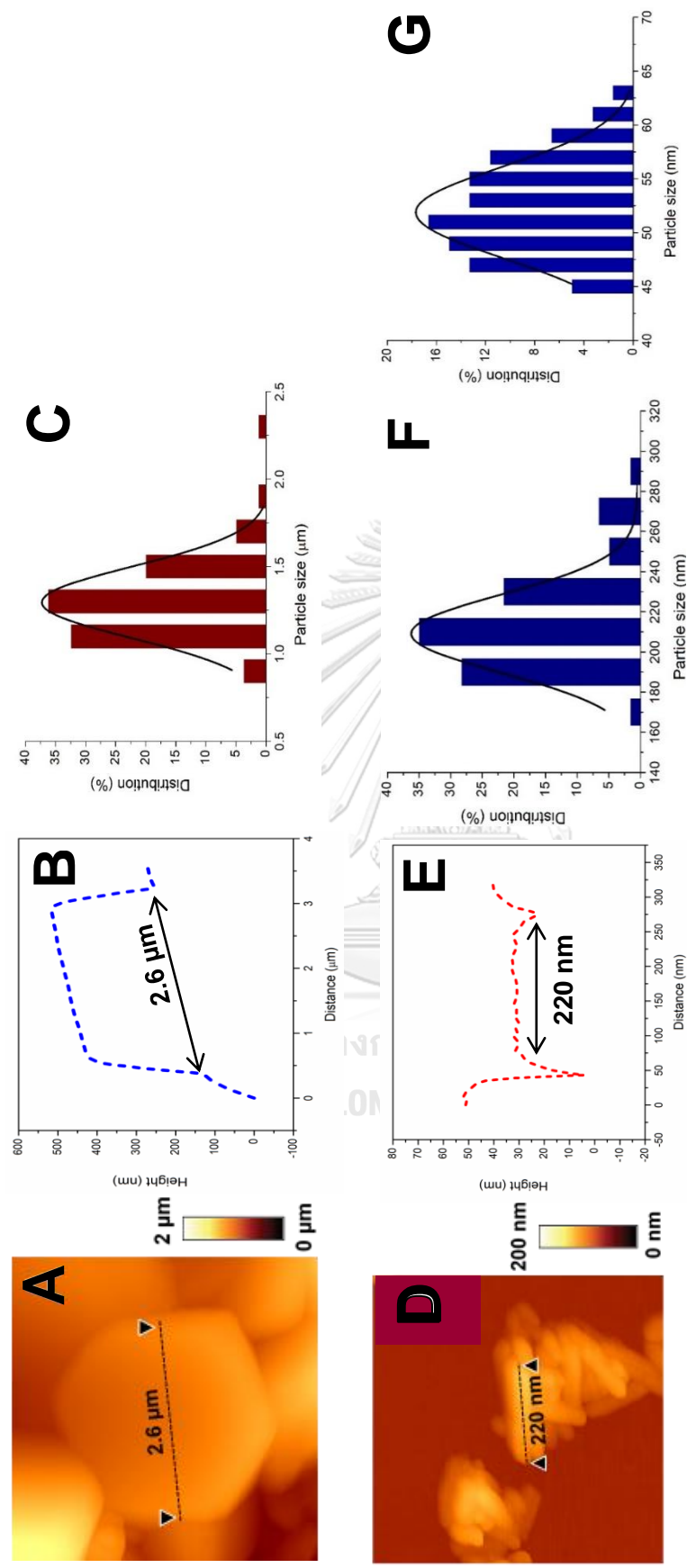


Figure 11 AFM topography images of ZnO particles. (A) and (D) AFM topography images, (B) and (E) height profiles of conventional hexagonal ZnO particles and ZnO nanorod particles, (C) and (F, G) the distributions of the conventional ZnO particles' side length and the ZnO nanorods' diameter and side length, respectively.

3.3.2 Characterization of the modified AFM probes

To confirm the structures of APTMS, CPTMS, and HDTMS, which respectively present amine, chlorine and methyl terminal groups, adhered to the AFM probe surface after surface modification, we performed high-resolution XPS and ATR-FTIR. The XPS spectra of the AFM probes functionalized with APTMS, CPTMS, and HDTMS, are shown in Fig.12A, 12B, and 12C, respectively. The Si2p XPS spectra of all the modified probes were fitted into two peaks: (i) at a binding energy of 103.0 eV (labeled in red) corresponding to the Si(-O)₄ binding environment of the native silica layer of the tip [86]; and (ii) at 102.2 eV (labelled in blue) corresponding to Si-O bonding in silanes [87]. The latter peak only appeared after surface modification, indicating successful attachment of silanes to the surface of the Si probes. These results were verified from the O1s spectra, which were fitted to three peaks at 533.6, 531.9, and 530.9 eV. These peaks have been shown to associate with oxygen in Si-OH, Si-O-Si in silica, and Si-O in silanes and are labelled in green, red, and blue, respectively [88, 89]. The observed signal corresponding to silica was higher than that corresponding to silane providing an indication of a very thin layer of silanes attached to each AFM probe surface, as expected from coating by the SAM technique. The atomic ratios between Si-O bonding of silane to that of Si-O-Si of silica in the tips modified with APTMS, CPTMS, and HDTMS were determined (from the ratio between the area under the two curves) to be almost identical (~0.37, ~0.36, and ~0.37, respectively). Hence, similar areal densities of silanes were achieved on each of the modified probe surfaces. Although the presence of a small amount of Si-OH suggested that the surfaces were not entirely covered by silanes, the signals corresponding to

silanes were much greater than those of Si–OH. Thus, the majority of functional groups on the surface were silanes. Furthermore, grafting of APTMS and CPTMS was confirmed by the presence of nitrogen (N1s, Fig. 12A) and chlorine (Fig. 12B) on the surface. The Cl2p core level spectra were fitted to a doublet of Cl2p_{3/2} and Cl2p_{1/2} peaks at 200.0 and 201.6 eV, respectively [90].

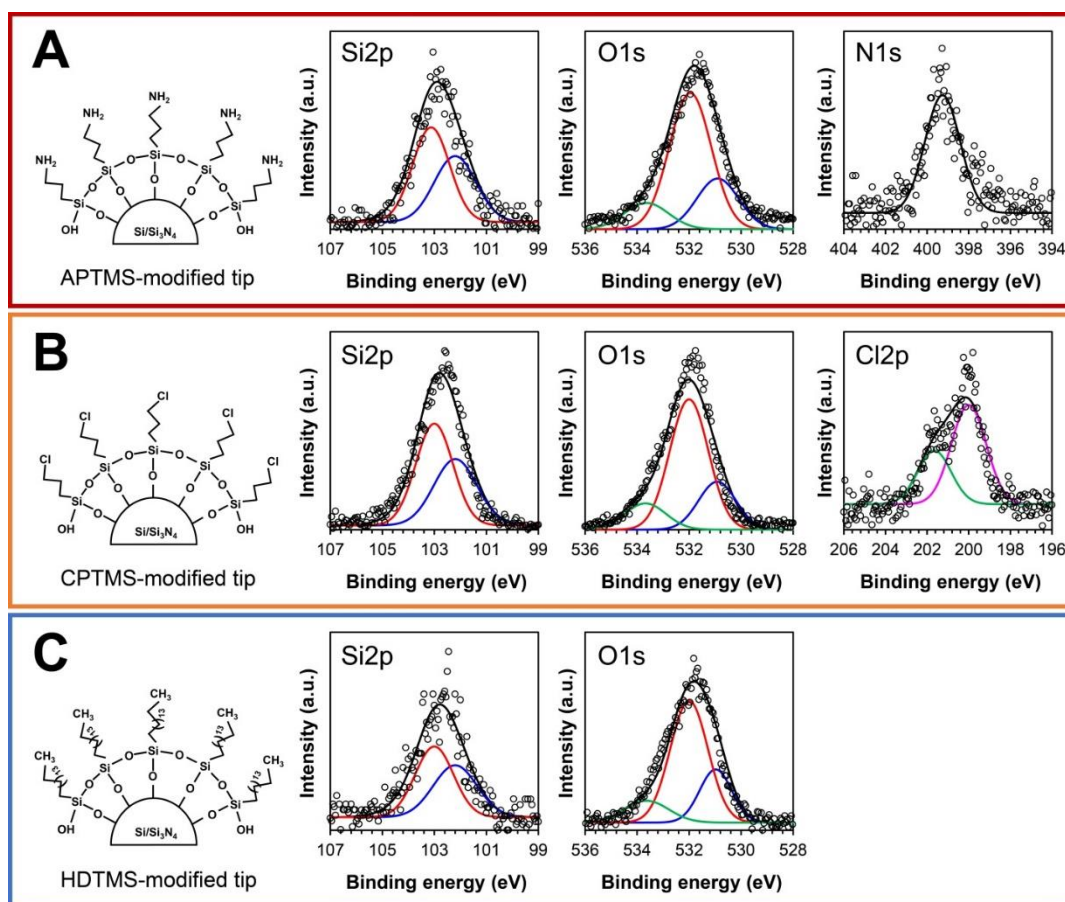


Figure 12 XPS Spectra of the functionalized AFM probes and high resolution Si2p and O1s XPS spectra of the Si AFM probes after silanization process with APTMS (A), CPTMS (B), and HDTMS (C). The N1s spectrum is also included for the probe modified with APTMS (A) and the Cl2p XPS spectrum for the probe modified with CPTMS (B).

In the SAM process, ATR-FTIR was used to complement XPS to confirm the surface modification of the AFM probes. While XPS analysis was performed on the tips that were used in AFM experiments, due to insufficient thickness of modified layer for FTIR detection, the ATR-FTIR spectra were obtained from another set of tips modified using increased silane concentration to increase the signals, as seen in Fig.13. For the modification with APTMS, as shown in Fig. 3.6A, all major FTIR signals corresponding to APTMS, i.e., the stretching and bending vibrations of NH_2 at 1562 and 3352 cm^{-1} [91], the C–N stretching vibration at 1323 cm^{-1} [91], the C–H stretching vibration in CH_2 and in CH_3 groups at 2839 and 2939 cm^{-1} [92], as well as the bending vibrations of the $-\text{CH}_2-$ groups at 1460 cm^{-1} [91, 93], were detected on the AFM tip after the modification. The signal of Si–O–Si at 1080 cm^{-1} was also detected, but it included the contribution from the existing native silica layer on the tip. The ratio between the signal from NH_2 at 1562 cm^{-1} and that from $-\text{CH}_2-$ backbone at 1460 cm^{-1} of pure APTMS was found to be 1.73, and it remained roughly the same, i.e., 1.93 from the APTMS-modified tip, which suggested that amine group remained unchanged after the SAM process. On the other hand, the signal ratio between that from CH_3 at 2939 cm^{-1} to that from the $-\text{CH}_2-$ backbone decreased from 2.23 to 1.02 after the modification. This confirmed that CH_3 in the methoxy group of APTMS was removed by the condensation with silanol group on the surface of the tip during SAM process; hence, silicon-side of APTMS was grafted to the tip, leaving the amine as the terminal functional group protruding from the surface.

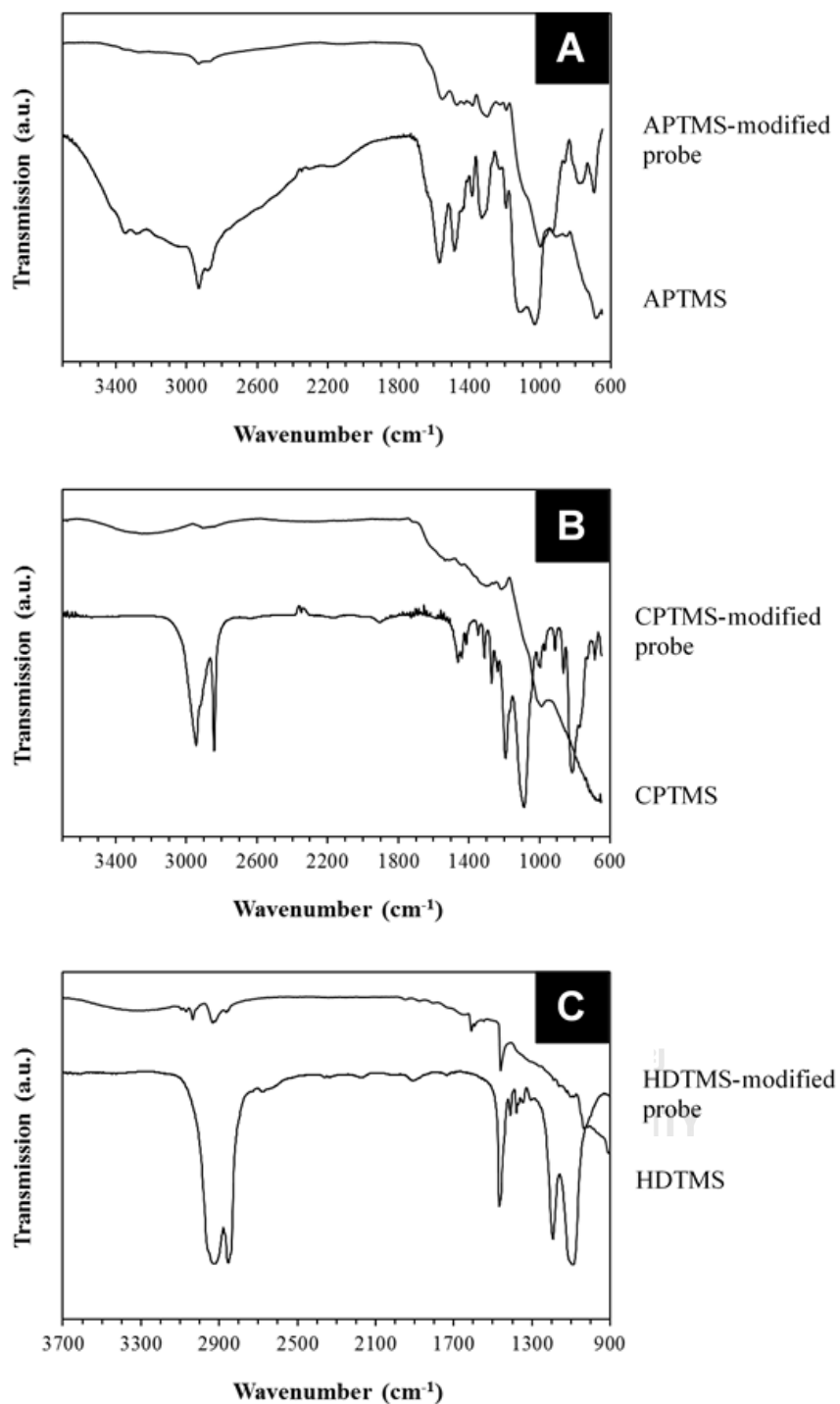


Figure 13 FTIR Spectra of the functionalized AFM probes. Graphs showing FTIR spectra of the Si AFM probes modified with (A) APTMS, (B) CPTMS and (C) HDTMS, respectively.

Comparable behavior was expected for modification with CPTMS and HDTMS because of the similarity in molecular structures of APTMS, CPTMS, and HDTMS. Unfortunately, although the XPS analysis clearly confirmed the presence of chlorine on the CPTMS-modified tip, the signal for C–Cl bonding at 698 cm^{-1} was not detected because C–Cl signal is very small in nature relative to signals from other functional groups [94]. Nevertheless, other signals from the backbone of silanes, e.g., C–H stretching and bending vibrations of CH_2 at 2839 and 1460 cm^{-1} , were still detected. The significant decrease in the CH_3 -to- CH_2 signal ratio after the modification with CPTMS (i.e., from 3.63 to 0.50) was also observed. For the HDTMS modification, although the CH_3 signal at 2939 cm^{-1} was drastically decreased by the grafting of the silicon-side of HDTMS to the surface, the CH_3 signal from the aliphatic end of the molecule was still clearly visible. Hence, the AFM tips were successfully functionalized. APTMS, CPTMS, and HDTMS were attached to the tips as monolayers with similar areal densities. More importantly, we were able to expose either amine, chloride, or methyl moieties as the terminal functional groups of each probe.

3.3.3 Adhesion measurements from AFM-based force-distance curves

Force-distance curves were determined for adhesive interactions between Zn-(0001), O-(000 $\bar{1}$), and Zn-O mixed-terminated ($10\bar{1}0$) surfaces of the ZnO particles and these different tips. Moreover, we complemented our study by analyzing interactions between the aforementioned surfaces with a bare Si probe. During the approach direction, a force converted from cantilever deflection qualitatively induced a small adhesion between the small probe and stiff surface, which is characteristic of the Derjagin–Muller–Toropov (DMT) model [40]. Our force-distance curves showed hysteretic characteristics because the force-

distance curves in the retraction direction did not fully overlap their corresponding curves in the approach direction. The balance between the cantilever spring force and the interaction force was not maintained temporarily when the probe jumped to contact (JTC) with the surface during the approach, and jumped off contact (JOC) from the surface during its retraction [95], although in our experiments, the JOCs were more pronounced than JTCs as shown in Fig.14. After coming into contact with the surface from approach, the tip was then withdrawn, and the external force used to retract the probe was counterbalanced by the adhesive force attracting the probe to remain on the surface [96]. The adhesive force reached its maximum value ($F_{Ad, max}$) when it was on the verge of being overcome by the external pulling force, as indicated by the lowest point of the retraction curve. At this cantilever displacement, the probe pulls off sharply. When comparing an identical ZnO surface/facet of representative force-distance curves, the maximum adhesion forces resulting from the NH₂ terminated probes were greater than those from the Cl, and CH₃ equivalents, respectively (see in Fig.14). These were also greater than those of the unmodified tips. Out of all force-distance curves that we obtained, the maximum $F_{Ad, max}$ of ~3.05 nN stemmed from an interaction between the NH₂-terminated probe and a hexagonal face of the conventional ZnO particle. Conversely, the minimum $F_{Ad, max}$ of ~0.48 nN is given by the interaction between the unmodified Si probe and the ZnO nanorods.

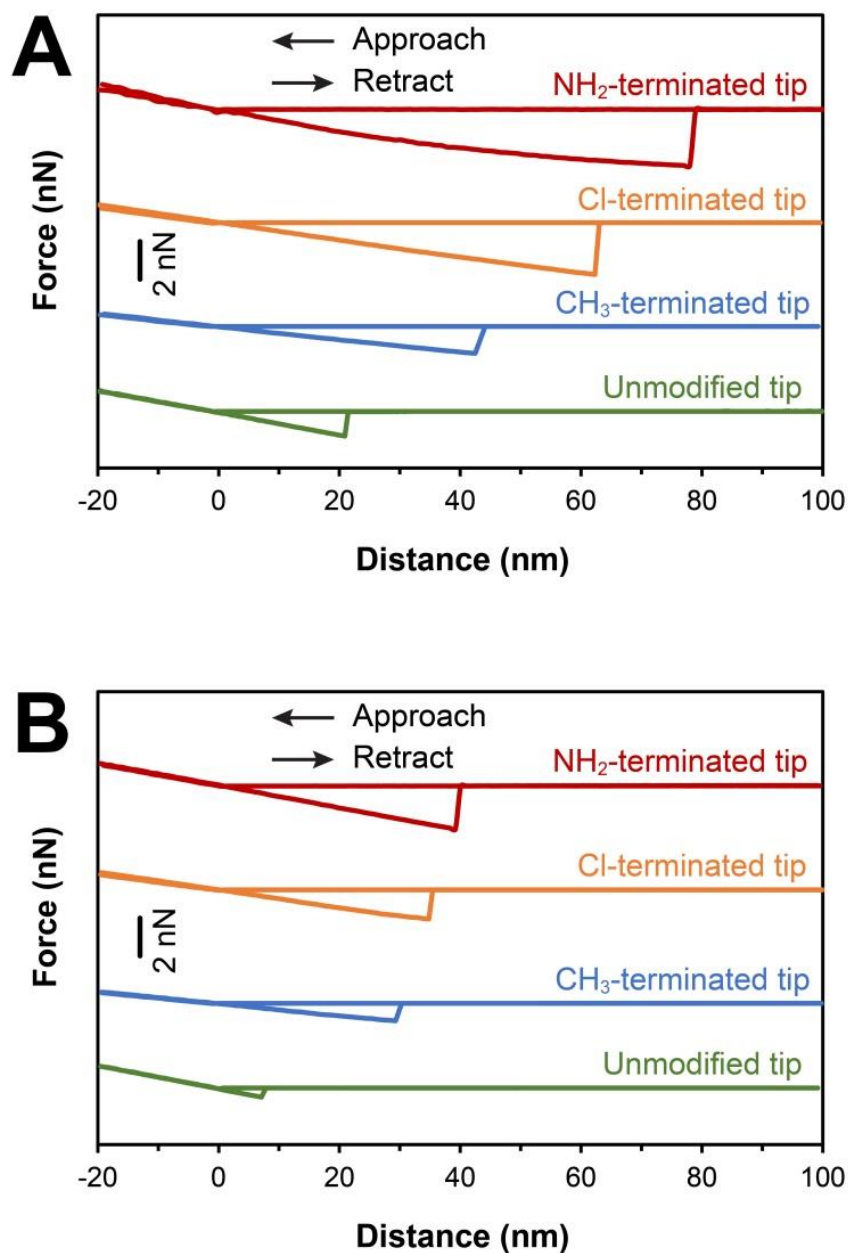


Figure 14 Force-distance curves for the interactions between functionalized/non-functionalized probes and ZnO surfaces. Representative force-distance curves between the surfaces of (A) conventional hexagonal ZnO particles, and (B) ZnO nanorod particles, and the modified probes with NH₂, Cl, and CH₃ terminals and the unmodified Si probe. The force curves were shifted in vertical axis for clarity of the plots.

To more precisely quantify the interactions for each pair of modified probe tips and ZnO surface type, we assessed the adhesion energy, defined as the area under the retract portion of the force-distance curve. We note that although it is possible to calculate the adhesion energies from individual force-distance curves, we obtained them conveniently from our data acquisition program (XEI, Park Systems) after we found that both methods provide identical adhesion energies. Owing to the magnitude of force (nN) and distance range (nm) of interactions in the context of force spectroscopy, the adhesion energy was in the range of aJ (10^{-18} J). Extracting adhesion energies from eight pairs of interacting functionalized/non-functionalized probes and ZnO surfaces, the averages and standard deviations were exhibited in Table 2. we found general trends for adhesion energies to be in accord with various aspects within our expectations.

Table 2 Adhesion energies (aJ) between functionalized/non-functionalized probes and ZnO surfaces.

Particles or surface	Type of tip modification							
	NH ₂ -terminated		Cl-terminated		CH ₃ -terminated		Unmodified Si tip	
	\bar{x}^a	S.D. ^b	\bar{x}^a	S.D. ^b	\bar{x}^a	S.D. ^b	\bar{x}^a	S.D. ^b
Conventional ZnO powder	90.03	29.28	60.12	20.2	7.07	3.83	5.74	2.74
				9	104			
ZnO nanorods	44.11	4.15	21.84	3.75	6.28	0.75	1.42	0.40
					69			

^aMeans of adhesion energy, ^bStandard Deviation, ^cSample size. The statistical analysis was performed using Origin software.

First, on average, the hexagonal surfaces of the conventional ZnO particles interacted with both unmodified/chemically modified AFM probes more strongly than exposed Zn-O mixed-terminated ($10\bar{1}0$) surfaces of the ZnO nanorods (Student's *t*-test for unequal standard deviation; for each modified/unmodified tip, $p < 0.05$). Interacting with polar molecule-terminated probes, the polar hexagonal ZnO faces resulted in $\sim 45\text{-}50$ aJ higher adhesion energy than the nonpolar facet of ZnO nanorods. Despite a small increase of $\sim 1\text{-}2$ aJ when interacting with the nonpolar molecule-terminated probe, the polar hexagonal ZnO surfaces contributed to a $\sim 2\text{-}4$ aJ increase in adhesion energy with respect to the 1.42 ± 0.4 aJ adhesion energy derived from the nonpolar ZnO nanorods. Second, the interactions between the modified probes and the ZnO surfaces—both hexagonal prismatic ZnO particles and ZnO nanorods—are greater than those between the unmodified Si probe and both surfaces. The modification of the Si tip could increase the adhesion energy up to $\sim 2\text{-}80$ aJ for the interaction with the conventional ZnO particles and up to $\sim 5\text{-}43$ aJ for the interaction with the ZnO nanorods. Among the modified probes, the NH_2 -terminated probes interacted with the faces of the ZnO particles more strongly than did the Cl-terminated probes; the polarity switching of charged terminals at the probe could amount to $\sim 20\text{-}30$ aJ of the increased adhesion energy. Both the polar-molecule-modified probes interacted more strongly than the nonpolar CH_3 functionalized probes. In the case of ZnO hexagonal surfaces, an attachment with polar molecules to the tip raised $\sim 55\text{-}85$ aJ of adhesion energy, with respect to an attachment with nonpolar molecules, while adding $\sim 18\text{-}40$ aJ in the case of ZnO nanorods. When considered both lowest and highest adhesion energies, modification of the Si probe tip with amine terminal appears to increase the strength of

interaction for more than an order of magnitude. The adhesion energies were elevated by ~82-87 aJ for the interaction with ZnO hexagonal facets, and by ~41-43 aJ for the interaction with ZnO nanorods. The difference between the highest and lowest adhesion energies derived from probes interacting with the same ZnO surface was approximately an order of magnitude. Notably, the standard deviations of the adhesion energies extracted from the hexagonally prismatic particles were relatively high at ~30% of the average adhesion energies for each probe.

To analyze how adhesion energies, particularly from interactions with conventional ZnO particles, were distributed, all the data with their percentage distributions are shown in Fig. 3.8. Unlike the interactions between the ZnO nanorods with modified/unmodified probes, the interactions resulting from prismatic ZnO particles yielded bimodally distributed adhesion energies. Within each interacting pair of conventional ZnO particles and a given terminal probe, we then divided the adhesion energies into two groups with the use of an average value of the entire adhesion energies as the cut-off. As a result, the mean values of the adhesion energy in one mode were 1.5–2.5 times as great as those in another, as listed in Table 3.

Table 3 Summary of adhesion energies determined between functionalized/non-functionalized probes and ZnO surfaces.

Particles or surface	Adhesion energy ($\times 10^{-18}$ J)			
	Type of tip modification			
	NH ₂ -terminated	Cl-terminated	CH ₃ -terminated	Unmodified Si tip
Conventional ZnO particles: the population with lower adhesion energy	62.82 \pm 1.41	44.42 \pm 8.37	3.71 \pm 0.79	3.24 \pm 1.04
	120.41 \pm 1.41	83.32 \pm 2.48	11.25 \pm 0.65	8.50 \pm 0.27
Conventional ZnO particles: the population with higher adhesion energy	44.11 \pm 4.15	21.84 \pm 3.75	6.28 \pm 0.75	1.42 \pm 0.40

*Note that these data were obtained by averaging results from at least 60 force-distance curves for each interacting pair.

These two modes of interactions might reflect the coexistence of two types of hexagonal facets: the positively charged Zn-(0001) face and a negatively charged O-(000 $\bar{1}$) face, exposed to the AFM probe. However, it was unclear which surface contributed to which energy mode. To determine the extent of adhesive strength that corresponded to either ZnO hexagonal surface, we examined the interactions on commercially available Zn-(0001) and O-(000 $\bar{1}$) surfaces of a single crystal ZnO wafer that had been grown hydrothermally and polished (ZnO Wafer; Semiconductor Wafer Inc), each of which will be addressed as a ZnO ‘standard’ surface hereafter. The distributions of adhesion energies obtained from interactions between the standard Zn-terminated and O-terminated ZnO surfaces and various modified/unmodified probes are shown together with those from the surfaces of ZnO particles in Fig.15.

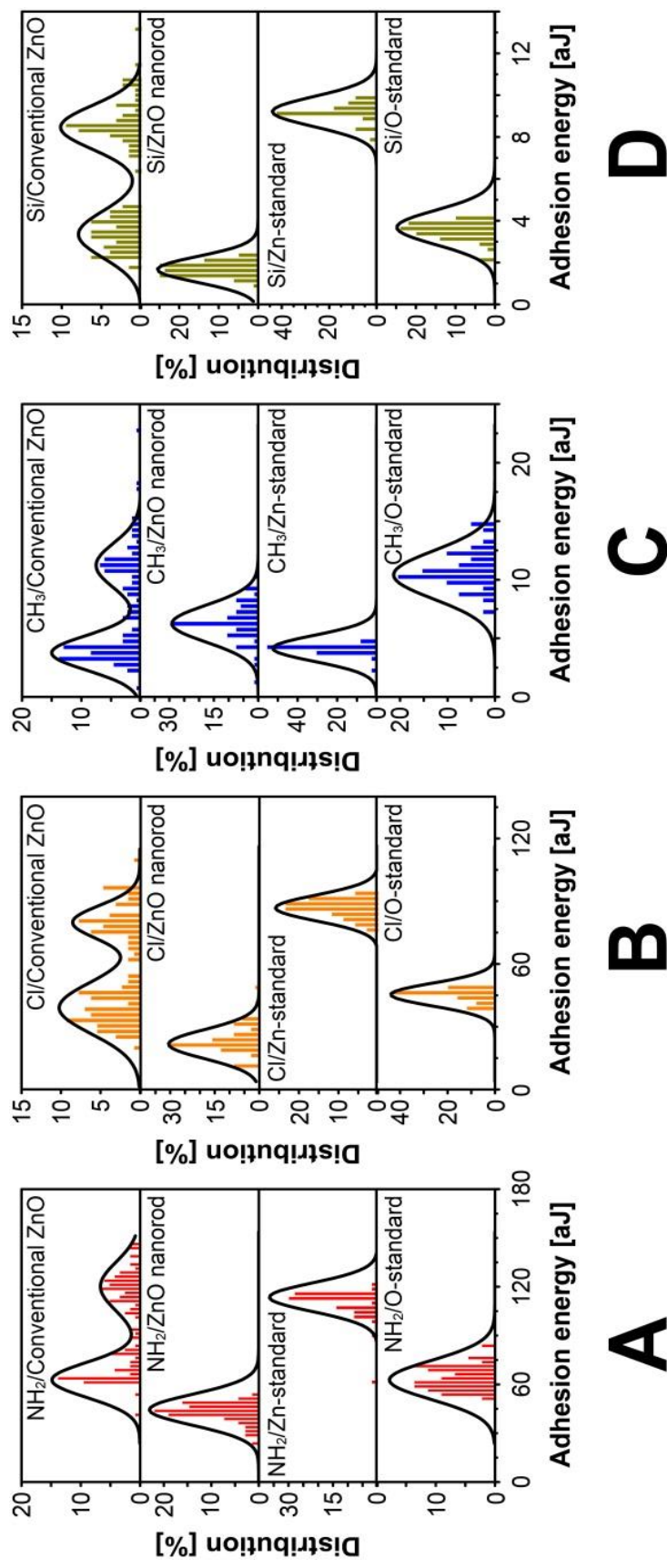


Figure 15 Adhesion energies of the interaction between AFM probes modified with (A) APTMS, (B) CPTMS, (C) HDTMS, and various ZnO surfaces. Results for interactions between unmodified Si AFM probes and ZnO surfaces are shown in (D).

To firmly associate the two hexagonal facets of conventional ZnO particles with either the positively charged Zn-(0001) or the negatively charged O-(000 $\bar{1}$) face, we performed multiple statistical tests (student's *t*-tests for unequal standard deviation, using the 5% significance level) for the eight modes derived from four interactions between the conventional ZnO particles and various modified/unmodified probes. The adhesion energy mean of each mode was compared to the adhesion energy mean of the 'corresponding' interaction pair, which we defined as a pair between the probe with the same modification and the standard (either Zn-terminated or O-terminated) ZnO surface on the condition that the pair's adhesion energy mean had initially appeared close to the considered mode's adhesion energy mean. According to our statistical comparison presented in Appendix A, there was no significant difference between the adhesion energies of the lower-energy mode that resulted from conventional ZnO particles and the 'corresponding' adhesion energies given by the standard O-terminated surface, when both interacting with the unmodified probe and the probes modified with polar molecules (distributions of each 'corresponding' pair shown in the top and bottom rows of Fig.15A, 15B, and 15D, respectively). Analogous to the lower-energy mode, the adhesion energies of the high-energy mode that emerged from the interactions of the ZnO hexagonal faces with these probes were not significantly different from the 'corresponding' interactions which were between the standard Zn-terminated surface with the same functionalized/non-functionalized tips (distributions of each 'corresponding' pair shown in the top and the third rows of Fig. 15A, 15B, and 15D, respectively). The interactions with the tip with nonpolar-molecule terminals, nonetheless, brought a dissimilar trend. As exhibited in the top and third rows of Fig.15C, the adhesion energy of the low-energy mode produced by the ZnO hexagonal

facets was not significantly different from that caused by the ‘corresponding’ standard Zn-terminated ZnO surface. Comparably, the adhesion energy of high-energy mode (the top row of Fig.15C) was not significantly different from the ‘corresponding’ adhesion energy from the standard O-terminated ZnO surface (the bottom row of Fig.15C). Taken together, these results indicate that for conventional ZnO particles, the interactions between the positively charged Zn-(0001) hexagonal facets and either a unmodified probe or a probe modified by polarized molecules gave rise to greater adhesion energies than the negatively charged O-(000 $\bar{1}$) counterparts. On the other hand, when interacting with nonpolar-terminated probe, the O-(000 $\bar{1}$) hexagonal faces generate greater adhesion energies than their Zn-(0001) analogues. The force distance curves after classifying the Zn-terminated and O-terminated facets of ZnO conventional particles are shown in Fig.16.

We noted two tendencies: when interacting with the polarized functionalized probe, the standard Zn-terminated surface had approximately twice as much adhesion energy as those of the standard O-terminated surface for amine- and chloride-functionalized probes. Although the absolute adhesion energies were much smaller, a similar trend appeared in the interaction between the unmodified Si tip with both standard ZnO surfaces. In contrast, when interacting with the nonpolar methyl-terminal probe, the mean adhesion energy resulting from the standard O-terminated surface was greater than that from the standard Zn-terminated surface.

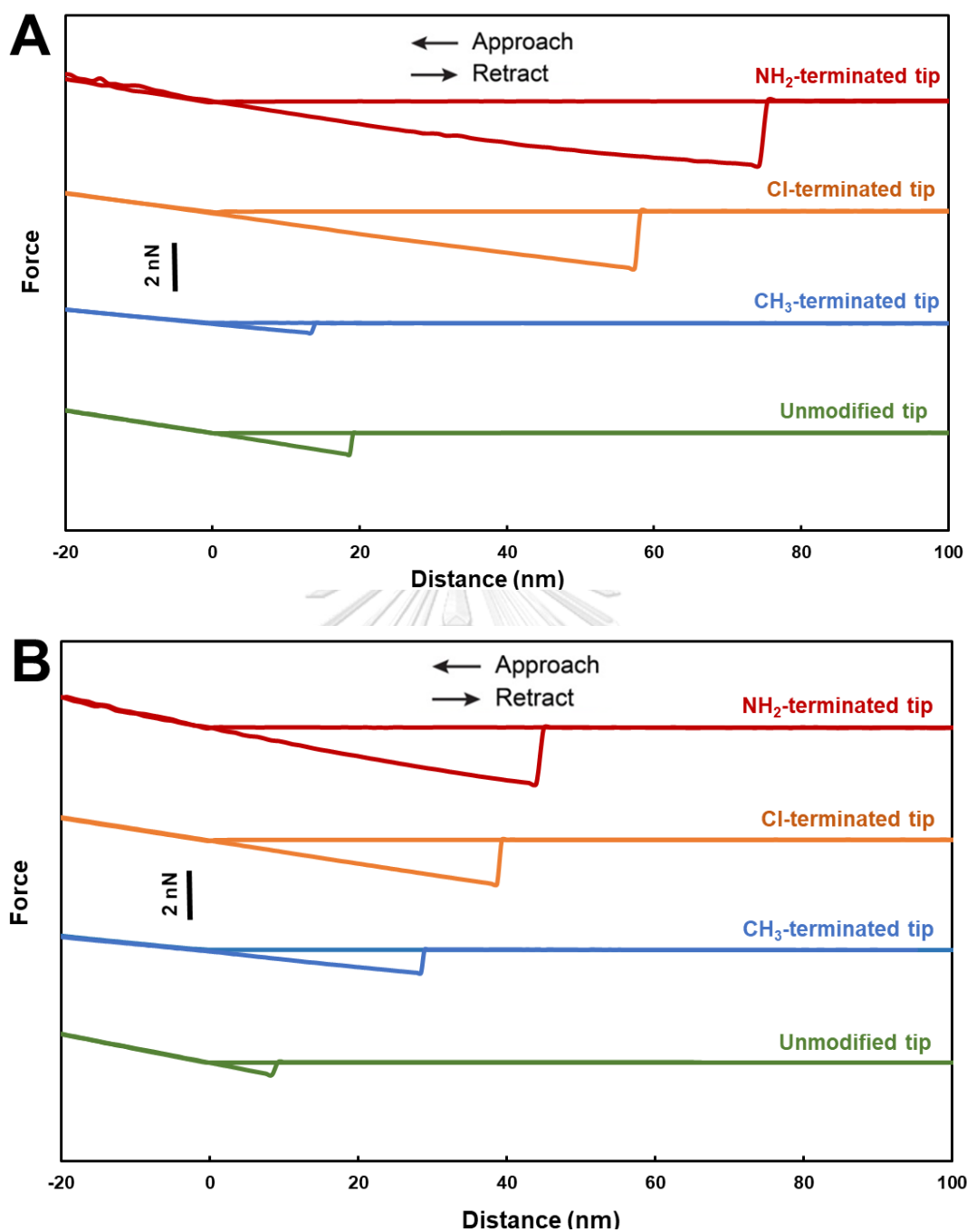


Figure 16 Force-distance curves for the interactions between functionalized/non-functionalized probes and ZnO surfaces. Graphs showing the representative force-distance curves between the surfaces of (A) Zn-terminated face, and (B) O-terminated face of conventional hexagonal ZnO particles, and the probe modified with NH₂, Cl, and CH₃ terminals as well as unmodified Si probe.

3.3.4 Estimation of Hamaker constants from AFM-based force-distance curves

Adhesion force and adhesion energy reflect the combined effects of several interactions, including intermolecular electrostatic attraction/repulsion, capillary action, and van der Waals (vdW) contributions [97]. The effects of the water meniscus that formed between the tip and the sample are excluded because the relative humidity (RH) was maintained under the critical value of 40%, which is reported to give rise to an additional attraction [98]. In the absence of external electrical/magnetic fields, we hypothesized that vdW interactions [99] play an important role in our observed adhesion phenomena:

$$F_{Adhesion} = F_{Electrostatic} + F_{Capillary} + F_{vdW} + \dots \quad (1)$$

The vdW potential originates from electrodynamic interactions between atomic or molecular dipoles within interacting entities and can be classified into three contributions based on whether the dipoles are permanent or instantaneous/induced. A permanent dipole occurs in a polar molecule in which certain atoms attract electrons more than the others, whereas an instantaneous dipole is associated with a nonpolar molecule that can be temporarily and occasionally polarized when electrons are drawn from one atom to another. The vdW contributions include Keesom interactions (i.e., permanent dipoles to permanent dipoles), Debye interactions (i.e., permanent dipoles to induced dipoles), and London or dispersion interactions (induced dipoles to induced dipoles), all of which can be analytically combined and described by the Hamaker constant (A_H), which is a constant derived from pair-wise summation over all the interacting atomic/molecular dipoles in the bodies [100]. We proceeded to use DMT

theory and calculated the Hamaker constant modeled after vdW interactions between a sphere (representing the AFM probe) in contact with a flat or smooth surface (representing the ZnO particle facets). When the tip radius was substantially greater than the tip-sample separation ($R \gg d$), the vdW force (F_{vdW}) can be estimated as:

$$F_{vdW} = -\frac{A_H R}{6d^2} \quad (2)$$

where A_H is the Hamaker constant, R is the tip radius, d is the tip-sample separation distance. The Hamaker constant was derived from the JTC portion in the approach direction of the force versus the tip-sample separation distance ($F-d$) curve.

The calculated Hamaker constants under each condition are associated with a modified probe and an unmodified Si tip, as listed in Table 4. Consistent with the trend observed in the adhesion energies, our derived Hamaker constants of the interactions between polar molecule-terminated probes and polar surfaces were greater than those when either the probe terminal or the surface was polar. These polar-polar interactions were greater still than those between the polar molecule-terminated probes and the nonpolar surface or between the nonpolar molecule-terminated probes and the polar surfaces. The Hamaker constants in the case of unmodified Si tip against either the polar Zn (7.21×10^{-20} J) or O (5.20×10^{-20} J) facets of the hexagonal ZnO surface were in agreement with the value of 7.38×10^{-20} J of ZnO against silica at room temperature in free space [101] that was estimated by Lifshitz theory based on information on the frequency-dependent dielectric properties of the two interacting materials and the medium in between. A slight reduction of the determined Hamaker constant from the theoretical value is attributed to the difference in the medium (air, which has greater

dielectric constant than the perfect vacuum used in the theoretical estimation), and inhomogeneity within the two interacting bodies: (1) SiO₂ at the surface/core Si within the unmodified Si tip (Vs. bulk SiO₂ for the calculation input) and (2) Zn-terminated/O-terminated surfaces (Vs. bulk ZnO for the calculation input), at the experiments. A notable reduction of the Hamaker constant to 1.69×10^{-20} J was found in the case of the nonpolar mixed-terminated Zn-O (10 $\bar{1}$ 0) surface of the ZnO nanorods.

Table 4 Estimated Hamaker constant between ZnO surfaces and various AFM terminated surfaces.

Surface	Calculated $A_H (\times 10^{-20} \text{J})$			
	Type of tip modification			
	NH ₂ -terminated	Cl-terminated	CH ₃ -terminated	Unmodified Si tip
Zn-terminated surface	22.57 ± 1.07	17.90 ± 0.89	1.53 ± 0.21	7.21 ± 0.72
O-terminated surface	14.82 ± 0.68	11.78 ± 0.53	2.43 ± 0.24	5.20 ± 0.57
Mixed-terminated surface	3.13 ± 0.16	2.80 ± 0.12	0.34 ± 0.10	1.69 ± 0.23

Furthermore, we found that modification of the probe surface by different silane molecules altered the vdW interactions as indicated by changes in the Hamaker constants. Modifications that increased the polarity of the probes appeared to increase the Hamaker constants whereas the opposite is true when the probes were modified to

be less polar. The Hamaker constants derived from the interaction between a polar NH₂- or Cl-terminated probe and a polar Zn-terminated or O-terminated surface were approximately an order of magnitude higher than those from the interactions between polar molecule-terminated probes and the nonpolar Zn-O mixed-terminated (10 $\bar{1}$ 0) surface and the interactions between the nonpolar CH₃-terminated probe and the polar surfaces. Moreover, the Hamaker constants in this group—NH₂- or Cl-terminated probes versus Zn-terminated or O-terminated surfaces—were also approximately two orders of magnitude greater than that obtained from the interactions between the nonpolar CH₃-terminated probe and the nonpolar surface of ZnO nanorods. Our results were consistent with the relative magnitudes of the intermolecular electrostatic interactions contributing to the estimated vdW attraction free energy. In other words, the ratio of the Keesom force to the Debye and dispersion (London) forces was approximately 100:10:1 [102]. Therefore, the trends for the Hamaker constants in the interactions between the modified probes and surfaces of the ZnO particles are consistent with the relative strengths of the vdW interactions, as classified by the polarity or effective dipole moment of the two interacting atoms/molecules. Our observed trends for the Hamaker constants were consistent with the measured adhesion energies for most of the ‘corresponding’ interacting probe-surface pairs. This result suggests that vdW interactions are a major factor influencing preferential adsorption during catalytic degradation of diuron. First, the interaction of polarized NH₂- or Cl-terminated tips, with a positively charged Zn-(0001) face resulted in greater Hamaker constants than that of a negatively charged O-(000 $\bar{1}$) face and that of a nonpolar Zn-O mixed-terminated (10 $\bar{1}$ 0) surface. Second, at the same surface, irrespective of its polarity, the interaction with the most negative NH₂-terminated probe yielded a greater

Hamaker constant than those of the negative Cl-terminated probe or the nonpolar CH₃-terminated probe. Third, for the interaction with the nonpolar methyl group, the Hamaker constants from the O-terminated surface of the conventional ZnO particle was highest and lowest for the Zn-terminated surface of the nanorods.

3.3.5 Simulation of charge distribution of the probe-modifying molecules

Although a similar trend of adhesion energies and Hamaker constants suggested a polarity-dependent interaction between different facets of wurtzite ZnO and various functional group terminals representative of diuron molecules, their slightly different trends pertinent to the methyl-terminated probes (onto the ZnO nanorod surface versus onto Zn facets of ZnO hexagonal prismatic particles) have led us to analyze the electronic charge distributions of all the probe-terminal silane molecules to gain insight into the potential physical or chemical origins. We performed ab initio calculations (for details, see “Materials and Methods”) and obtained a three-dimensional map of electron density for an entire molecule and the normalized fractional charge of each atom within a molecule for APTMS, CPTMS, and HDTMS, as shown in Fig.17. It should be noted that the ab initio calculations were performed as free molecule in vacuum. Hence, it was assumed that the surrounding air did not drastically interfere with the electron density of the molecule. It was also assumed that the binding of silanes onto the AFM tip did not significantly affect electron density at the terminal functional groups. According to the XPS results discussed in Fig.12, amine, chloride, and methyl functional groups were the outermost terminal groups at the ends of the AFM probes modified with APTMS, CPTMS, and HDTMS, respectively. As a consequence, when the tip approached/withdrew from the surface, we anticipated our designated terminal groups to be perpendicular to the ZnO facets. In the amine-terminated probe that had

the highest adhesion energy among the functionalized probes (Fig.15), the amine terminal as depicted in the electronic distribution of APTMS in Fig.17A (where the fractional charges of N-atom and H-atom are -0.449 and c.a. $+0.177$, respectively), was expected to expose either two H-atoms or a lone-pair of electrons on the sp^3 hybridized N atom upon approach/ retraction. However, because of the electrostatic intermolecular attraction between the different apparent charge types, the amine group electron lone-pair attached to a positively polarized Zn-(0001) face. Conversely, the H-atom turned its end towards the negatively polarized O-(000 $\bar{1}$) face [103, 104]. In a configuration favorable for adhering to O-(000 $\bar{1}$) facets of hexagonal ZnO, the effective interaction with the NH_2 -terminated probe was reduced, compared with that of the configuration that adhered to Zn-(0001) facets. This difference is attributed to repulsion between electron-rich N atoms and the oxygen face. The terminal group of APTMS is likely to twist to different parts towards various surfaces of different polarities; thus, allowing us to infer a practical course of diuron adsorption at the photocatalyst ZnO surface during its degradation.

Similar to the probe with polarized NH_2 terminals (modified with APTMS), the polarized Cl-terminated probe also resulted in a large adhesion energy when interacting with the ZnO conventional particles and nanorods because both the APTMS and CPTMS molecules that were used to modify the probes have the same chemical structure as silane (Fig.17A and 17B). The differences among the adhesion energies of the interactions with ZnO particles are attributed only to their functionalized amine and chloride terminals. The ability to produce strong adhesion with ZnO facets also depends on the collective effects of other atoms in proximity within the end group of the

molecule [105]. The nitrogen atom in APTMS is adjacent to two hydrogen atoms and a carbon atom whereas the chlorine atom in CPTMS only binds a carbon atom; the resultant electron density of nitrogen or chlorine within the configurations is represented by the calculated fractional charge that reflects the polarity of the terminal. The fractional charge of the nitrogen atom in APTMS is -0.449 (Fig.17A), whereas that of the chlorine atom in CPTMS is -0.183 (Fig.17B). Therefore, the interaction between the amine-terminated probe and all ZnO surfaces might be expected to be stronger than any interactions of the chlorine-terminated probe. Nevertheless, we noted strong adhesion between the chloride-terminated probe and the negatively polarized O-($000\bar{1}$) face. Chloride should be repelled from oxygen-terminated facets; the hydrogen atoms adjoining the same carbon atom as chlorine (with the fractional charges of $+0.137$ and $+0.138$), are instead expected to turn toward the surface.

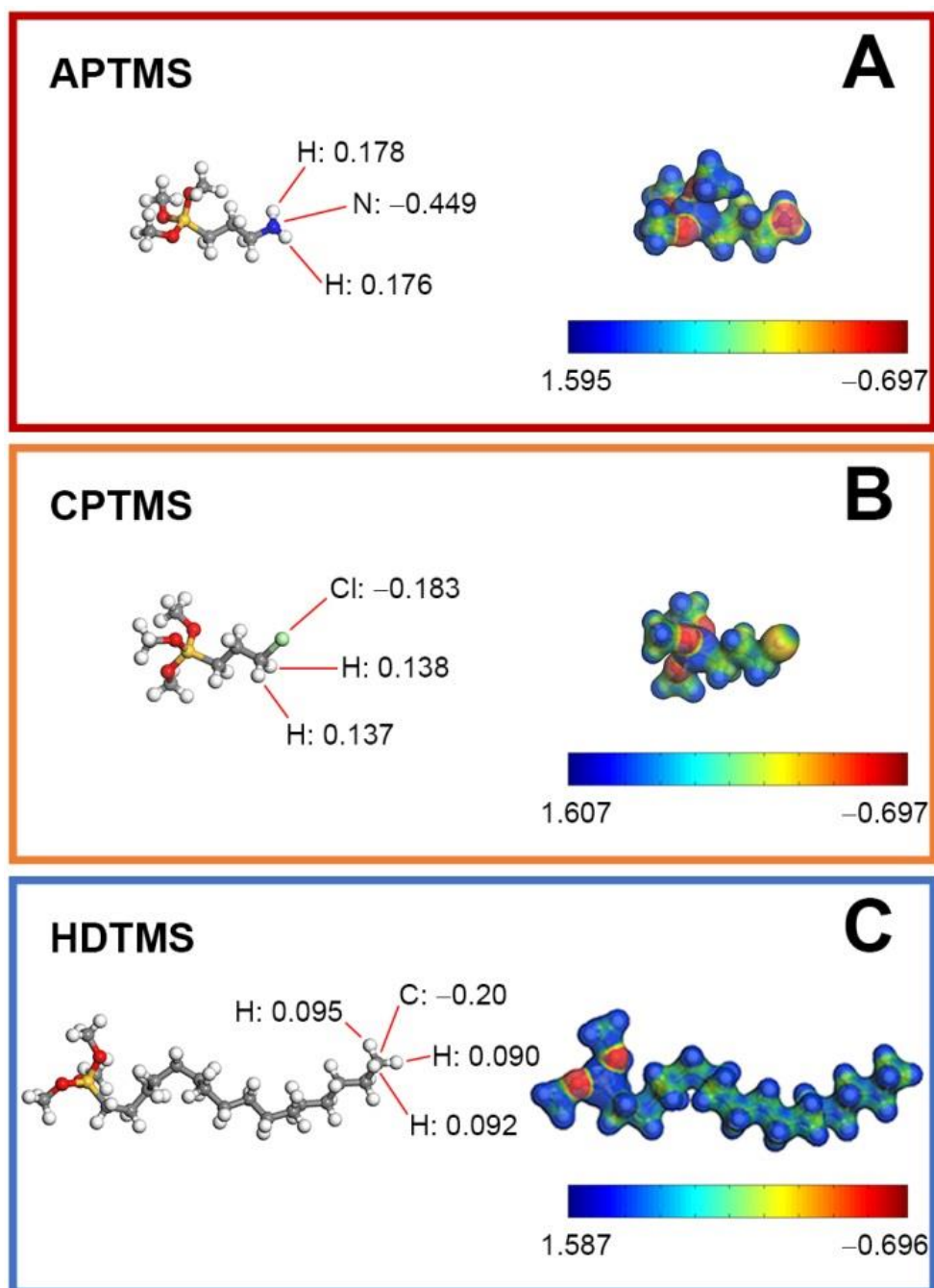


Figure 17 Molecular structure, electronic distribution and normalized fractional charge of the AFM probe-functionalizing molecules: (A) APTMS, (B) CPTMS, and (C) HDTMS. Note that blue and red margins of the scale represent levels of maximal positive and negative charge density normalized within a given molecule, respectively.

For the nonpolar methyl-group the adhesion energy resulting from its interactions with O facets was stronger than that with Zn facets whereas the adhesion energy associated with ZnO nanorods lay between these two values [69, 106]. The HDTMS molecule that was used to functionalize the probes also had a similar chemical structure to that of APTMS, except for a longer alkyl chain, as shown in Fig.17C. The 3D electron density map of the HDTMS sidechain represents a mostly neutral carbon backbone with a fractional charge close to zero. These carbon atoms are sp^3 hybridized with either nearby carbon atoms or hydrogen atoms, which are positively polarized as indicated by a fractional charge of $\sim+0.09$. Therefore, the strongest adhesion energy results from the interaction of the methyl group with the oxygen-terminated face of conventional ZnO particles. This strong adhesion is attributed to interactions between the three hydrogen atoms of the methyl terminals with the negatively polarized oxygen hexagonal facet [107, 108]; this interaction is expected to dominate the repulsion between the neutral carbon atom and the facet owing to steric hindrance of the methyl group's hydrogen atoms. In a similar manner, the attraction between the positively polarized Zn hexagonal face and the carbon atom of the methyl terminal is hindered by steric effects of the hydrogen atoms (Fig.17C). The attraction might also be opposed by a slight repulsion between these hydrogen atoms, each of which has a positive fractional charge of ~0.09 (Fig.17C). These interactions (including steric effects) specific to the HDTMS terminal of the probe might make them less adhesive to the Zn facets than the oxygen facets of the conventional ZnO particles. However, it is not relevant to the vdW measurements that were performed by interactions during the approach portion of the force and tip-sample separation curve. In addition, our results that $E_{ad, Zn-O(10\bar{1}0)} > E_{ad, Zn-(0001)}$ for interactions of the CH_3 -terminated probe suggest that the

approaching/adhering configuration of methyl-groups at the nonpolar Zn-O mixed-terminated ($10\bar{1}0$) surfaces might change the interaction distance (between the interacting atoms), thereby altering the intermolecular interactions.

As indicated by the low adhesion forces and adhesion energies in general, the nonpolar Zn-O mixed-terminated ($10\bar{1}0$) surfaces of the ZnO nanorods interacted less strongly with most of the modified probes than either the Zn-(0001) and O-(000 $\bar{1}$) facets of the conventional ZnO particles. As an approximate result of the alternating zinc and oxygen atoms on the nanorod surfaces, the charge balance decreased the density of dangling bonds or surface vacancies at the surface compared with those on polar hexagonal facets; thus, making the nonpolar surface more stable [109, 110]. The interaction with the HDTMS-functionalized probe, which is also nonpolar had a lower adhesive strength than those of probes with polar APTMS or CPTMS terminal groups. It has been reported that interactions are adhesive when the tip and surface have the same polarity; however, we found the adhesion energy between the nonpolar methyl-terminated probe and nonpolar ZnO facets of the nanorods to be ~ 6.28 aJ, which is not as high as the adhesion energy between the polarized chloride- or amine-terminated probe and the polar Zn or O hexagonal surface. We attribute this low adhesion energy to the interaction (between the nonpolar ZnO nanorod surface) with the nonpolar terminal molecules that also had a low surface energy [72]. However, the observed trends of the adhesion energies between the functionalized tips and all ZnO surfaces: Zn-terminated, O-terminated and Zn-O terminated, were identical, i.e., $E_{ad,NH_2} > E_{ad,Cl} > E_{ad,CH_3}$.

The experimental results suggest that different parts of the diuron molecule adhered to (at least) three facets of ZnO. The vdW interactions make the main contribution to diuron adsorption; however, the relative magnitude of the three vdW-contributing collective electrostatic interactions depends on the atomic arrangement of the catalyst surface and the functional group that approaches the surface. For interactions of the polar surface of ZnO (i.e., zinc- or oxygen-terminated surfaces), parts of the diuron molecule with permanent dipole character (such as nitrogen or chlorine atom) might give rise to Keesom interactions. Such interactions are approximately an order of magnitude greater than those of induced dipoles, i.e., those induced by the methyl groups. Therefore, to maximize the adhesion with the zinc-terminated surface, diuron molecules are likely to adsorb in a planar configuration with the aromatic ring and both of its chlorine atoms lying parallel to the surface. The aliphatic chain is likely to turn so that the nitrogen or oxygen atom are directed towards the surface. Consequently, intermediates resulting from attack of hydroxyl radicals on either the aromatic or aliphatic side of the diuron will be formed. At the oxygen-terminated surface, the repulsion between oxygen on the surface and parts of the diuron molecule are enriched in negatively charged atoms, such as nitrogen and chlorine atoms. This effect tends to be counteracted by the attraction from hydrogen atoms adjacent to nitrogen atoms. The diuron molecules achieve a balanced state by adopting an adsorption configuration that aligns the aliphatic side towards the oxygen-terminated surface and tilts the aromatic side perpendicular to the surface, pushing the atomic origin of the repulsion as far as possible. As a result, the intermediates formed on this facet are expected to have their aromatic side preserved and the aliphatic side will be oxidized by hydroxyl radicals.

During diuron adsorption on a mixed-terminated surface, the Debye interactions between the molecular portions that have permanent dipoles (i.e., nitrogen or chlorine atom), and the nonpolar surface are an order of magnitude greater than the London interaction between the methyl groups and the surface. Hence, the adsorption configuration of diuron molecules, in general, is presumed to be similar to that on a zinc-terminated surface, i.e., a planar configuration to maximize attractions between nitrogen and the surface, and between both chlorine atoms and the surface. Consequently, degradation intermediates generated by attack on either the aromatic or aliphatic side by hydroxyl radicals might also be expected. However, interactions between diuron and the nonpolar mixed-terminated surface should be weaker than interactions that occur when diuron molecules adsorb on to the polar Zn-terminated surface, according to polarity of the molecule-surface pair. The prediction based on our force spectroscopy is in line with previous DFT simulations, which found the adsorption energy of diuron molecules on a mixed-terminated surface to be the least favorable, among the three facets of ZnO particles [60]. In addition, considering the atomic charge at the surface localized at the position of adsorption, the diuron molecules bent to share the same type (positive or negative) of charge and minimize repulsive forces. This effect reduces the adhesion strength and the probability of radical attack, respectively. This reduction also lowers the degradation rate of the Zn-O mixed-terminated surface of the ZnO nanorods. Further decreases of the degradation rate might explain previous anomalous results from photocatalytic degradation experiments. Despite an order of magnitude larger specific surface area (area per mass), nanorods appears to have a degradation rate comparable with that of conventional ZnO hexagonal particles [60]. The findings in this work should be applicable to address abnormal

behaviors observed in other photocatalytic materials as well, e.g., two sets of anatase TiO₂ with roughly the same adsorption capacity but showed three-times difference in catalytic activities [111]. It should also contribute to the difference in the degradation, including degradation rate and degradation pathways, on different photocatalyst, e.g., ZnO or TiO₂ [60, 112, 113]. This issue is especially important for the degradation of toxic compounds because the pathway with increased toxicity must be avoided.

3.4 CONCLUSION

We have established the potential for application of AFM imaging to visualize catalytic particles and AFM-based force spectroscopy to examine physical adsorption of reactant molecules onto a catalyst surface in heterogeneous catalytic reactions. As demonstrated in a reaction of diuron degradation catalyzed by ZnO, AFM probes chemically modified with terminal molecules that represent various functional groups of diuron (reactant) were applied to facets of ZnO particulate prisms (catalyst) that exhibited different polarities. A notable difference between the adhesion energies in a systematic study of these interacting functionalized probe/surface pairs allowed us to distinguish the two polar surfaces of conventional ZnO particles. Furthermore, the similar trends of the adhesion strengths and Hamaker constants indicate that vdW forces are the main interaction controlling adsorption of diuron molecules to the ZnO catalytic surface. These interactions corroborate the nature of preferential interactions and the adsorption configuration of the functional groups within the reactant molecules and specific adsorption sites of the catalyst surface. This technique might also be used to systematically study interactions that occur when a reactant adsorbs on a catalyst surface for other heterogeneous reactions in which the catalyst is classified as structure-sensitive. A precise understanding of adsorption might enable the catalyst surface to be

tailored for fine tuning of the adsorption configuration to improve the overall catalytic activity.



CHAPTER IV

**AFM-BASED FORCE SPECTROSCOPY STUDY OF
HYDROPHOBIC/ HYDROPHILIC ATTRACTION'S
INFLUENCE ON TALCUM ADHESION**

Vipada Dokmai¹, Kitiphath Sinthiptharakoon², Witchukorn Phuthong^{3,*} and Varong Pavarajarn^{1,*}

¹ Center of Excellence in Particle and Materials Processing Technology, Department of Chemical Engineering, Faculty of Engineering, Chulalongkorn University, Bangkok 10330, Thailand

² National Nanotechnology Center (NANOTEC), National Science and Technology Development Agency (NSTDA), 111 Thailand Science Park, Phahonyothin Road, Khlong Nueng, Khlong Luang, Phatum Thani 12120, Thailand

³ Department of Physics, Faculty of Science, Kasetsart University, Ladyao, Chatuchak, Bangkok 10900, Thailand

KEYWORDS: Force spectroscopy, Adhesion, Hydrophobic character, Surface modification, Talc treatments

Submitted: Surface and Coatings Technology

ABSTRACT: Since the hydrophobicity characteristics of clay minerals are important. It is believed to be influential in its properties such as surface property, polarity, surface wettability and agglomeration property. In this work, the chemically modified of talc particles through acid treatment and grafting with different organosilanes coupling agents were investigated. An AFM-based force spectroscopy has been used to measure the adhesive interactions. According to the HCl-treated talc, the breaking of Si-O-Si bonds was found, increasing a large number of silanol groups on the particle's surface. Similarly, grafting APTMS on talc particles leads to the enhancement of hydrophilic components (amino groups) on the surface, resulting in highly adhesive forces. These methods achieve for the improvement of the adhesion interactions. And the decrease of hydrophobic portion on talc structure gives rise to the relatively strong adhesion on talc surface. In contrast, the small adhesion was observed in HDTMS-grafted talc particles due to their hydrophobic-hydrophobic attractions. The degree of hydrophobicity was estimated from the contact angle measurements. In this study, two exposing surfaces (basal planes and edges) of talc can be postulated and predicted from the strength of adhesion force. The Hamaker constant, which exhibits the strength of vdW interactions, can be derived from F-d curves. The noticeably differences in two orders of magnitude of the curves can be clearly seen when using the tip-surface functionalization with self-assembled monolayers terminating in strong hydrophobic and hydrophilic groups. This result indicates that intermolecular interactions, such as hydrophobic effect dominates the adhesive force. The understanding of particle-surface interactions will give many advantages to clay mineral's applications, such as filler materials, clay-polymer composites, mineral processing, etc.

4.1 INTRODUCTION

In addition to its emerging roles in material composites or two-dimensional nanomaterials, a typical clay mineral, Talcum [$\text{Mg}_3\text{Si}_4\text{O}_{10}(\text{OH})_2$] or Talc, has been traditionally in demand for many industries including catalyst, pharmaceuticals, paper, plastics, wastewater treatment and cosmetics production, because it has various favorable properties [114-116]. Filler materials, where the talc particulates are combined in the matrix such as polymer blends, relies on talc's dispersion and aggregation behavior, in a great degree [117, 118]. In wastewater treatment, talcum was shown to remove more heavy metal ions per volume of input water than mesoporous silica [119]. Together with other advantageous attributes such as thermal stability, the communal property that enables these effective uses of talcum is adsorption which depends on the solid structure (along with its interactions) at the talc surface.

In the monoclinic crystal structure of talc consisting of layers of brucite (magnesium hydroxide) octahedral sandwiched between silica tetrahedron sheets stacked on each other, as shown in Fig.18, the nonpolar layers of silica tetrahedron, also called siloxane (Si-O-Si) are mostly exposed on the surface. However, the presence of Si-O-Si groups on talc surface makes it difficult to dissolve it in organic solvents [120]. Moreover, the external oxygen atoms on the siloxane surface of talc are relatively weak electron donors and interact weakly with water molecules [121, 122]. The hydrophobicity of siloxane surface was also confirmed by the adsorption of aromatic hydrocarbon [123]. Therefore, the existence of siloxane structure can significantly affect agglomeration behavior and dispersion stability of colloidal clay minerals [124]. On the other hand, some portions of the talc surface contain hydroxyl groups such as Si-OH and Mg-OH, which are hydrophilic and dispersible in aqueous solutions. The

contact angles of siloxane and hydroxyl surfaces, examined using molecular dynamics simulation (MDs), that were found to be 105° for tetrahedral surface, but zero for the octahedral surface [125, 126] established that the siloxane surface is associated with the hydrophobic character of the mineral while its hydrophilicity arises from the hydroxyl groups [127]. These results suggest that adsorption on talc surfaces can be adjusted to suit with specific applications through various surface modifications.

Alternating the chemical structure at the Talc surface can be achieved with an assortment of coupling agents [128]. Many reports showed that acid treatment improved talc's adsorption capability. In these works, the impurities on talc surfaces were eliminated using organic acids, resulting in the cleaner talc surfaces; the authors attributed the enhanced adsorption of the cleansed surfaces to the uncovered internal pores within the talcum powder [129]. In filler application, the interfacial interaction between the talc (as a strength-reinforcing agent) and polymer matrix (e.g. polypropylene) was altered using organofunctional silanes treatment [130, 131], yielding the increased mechanical properties characterized by tensile strength, friction and Young's modulus [132]. However, an accurate manipulation of talc surfaces with chemicals such as acids or organosilane requires a solid understanding of the interaction that the modified talc surfaces would generate respect to unmodified talc surfaces.

In recent years, advanced analytical methods have enabled studies on the clay minerals at micro and nanoscale [45, 133], including atomic force microscopy (AFM) for particle's surface characterization and adhesion force measurement. With regards to other clay minerals, the specific faces of layered silicates was identified based on the different magnitudes of the interaction forces in both air and aqueous solution [134].

The surface potentials of edge and basal planes of chrysotile and kaolinite were estimated by fitting AFM force curves with a model from DLVO theory [135]. In these works, each force as well as the point of zero charge (PZC) corresponding to each plane varied with pH of the aqueous medium [134, 136]. The dependencies of the surface charge of two faces (of the minerals) on solution pH was consistent with the specific interactions derived from the model [137]. Similar to kaolinite and other minerals, talc's surfaces dominated by siloxane and hydroxyl groups are hardly distinguished by elementary analytical techniques. Compared to previous work, the surface modification of AFM tips with the extremely hydrophilic/hydrophobic molecules have also been conducted for quantifying these interactions. Although the surface interactions, described in terms of wettability, of talcs were investigated using MDs [138], the surface interaction forces or interfacial adhesions have not been experimentally characterized. In the present study, we modified talc particles with the aforementioned coupling agents and investigate the interaction forces and adhesion mechanism using AFM-based force spectroscopy in ambient conditions. This work will provide grounds for a comprehensive understanding of how certain surface modification of talc particles affects the interaction between talc surfaces, leading to the improvement of wettability or binding adjustment.

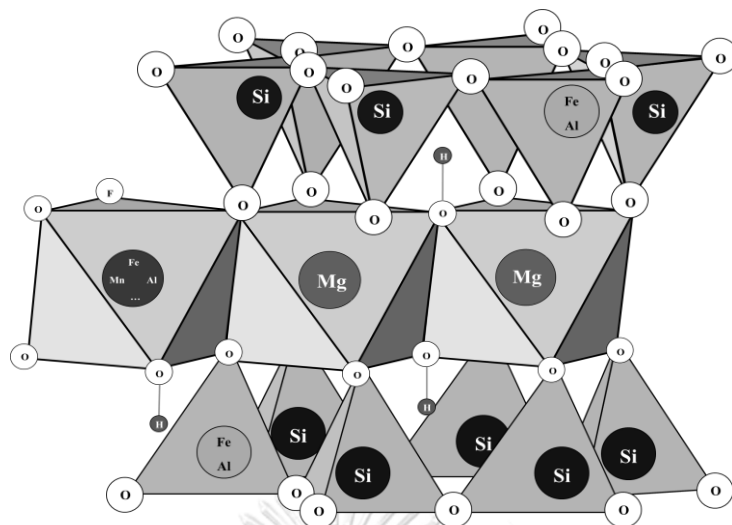


Figure 18 Talc composition structure

4.2 EXPERIMENTAL DETAILS

4.2.1 Particle modification

Acid treatment

For the acid treatment, talcum powder (hydrous magnesium silicate, $\text{Mg}_3(\text{Si}_4\text{O}_{10})(\text{OH})_2$, $\leq 100\%$, Sigma-Aldrich – referred to as ‘talc’ hereafter) was immersed in hydrochloric acid (HCl, 37%, QRëC, Chem-Supply Pty Ltd.) with the powder-to-acid-ratio of 1 g/ 10 mL in a glass reactor under magnetic stirring at $80 \pm 2^\circ\text{C}$ for 2 h. Then, the modified particles were filtered, washed with deionized water (18 M Ω .cm resistivity with a Millipore Milli-Q filtration system), and dried at 70°C for 48 h in a vacuum drying oven.

Organosilanes grafting

Five g of talc was introduced into 400 mL of ethanol under magnetic stirring. The mixture was vigorously stirred until a homogeneous dispersion solution was obtained. 5 mM of 3-Aminopropyltrimethoxysilane (APTMS, 97%, Sigma-Aldrich)

and Hexadecyltrimethoxysilane (HDTMS, $\geq 85\%$, Sigma-Aldrich) were added to the solution, stirred at room temperature for 24 hours, and the solution was aged for additional 24 hours to allow a complete permeation of organosilane in talc [128]. After that, the solution was centrifuged for 10 minutes at a speed of 10,000 rpm; the ethanol was removed. The remaining gel was finally dried in an oven at 80°C for 20 minutes

4.2.2 Characterizations

Before and after various surface modifications, talc samples were subject to detailed characterizations. The surface morphologies were examined using Scanning Electron Microscopy (SEM, JSM-7610F, JEOL, Japan) at 5 kV. The surface topography and surface interaction forces of the samples were investigated by atomic force microscopy (AFM, XE-120, Park AFM, Park Systems Corp., Korea). The chemical bonds and the functional groups attached on the surface were determined using Fourier Transform Infrared Spectroscopy (FTIR, Nicolet iN10, USA). The spectra were obtained in the range from 500 to 4000 cm^{-1} , running 64 scans at a resolution of 4 cm^{-1} . The surface wettability of talc samples was identified from contact angle measurement (OCA40, dataphysics TC/TPC 150, Germany) using the sessile drop method. 100 mg of each talc sample was mechanically pressed to form a pellet of 1 mm thickness and 1 cm diameter by hydraulic pressure. The drop images were recorded by a video camera and an image analysis system. The contact angle (θ), averaged from 8 drops, were used to report for the contact angle the corresponding talc sample.

4.2.3 Sample preparation for AFM imaging and force spectroscopy

Silicon wafer was used as a planar substrate in adhesion force measurements. Before particle deposition, the substrate was rinsed with ethanol and deionized water and dried in an oven for 10 minutes at 120°C. Two g of unmodified/modified talc sample was first deposited onto the cleansed substrate in a confined space. The pile of the talc sample on the substrate was then randomly drifted by nitrogen blow and incubated further for 30 minutes in the same closed space. After that, the sample was rinsed with deionized water to remove the excess particles which were potential contaminants before left to dry at 120°C for 30 minutes. The surface morphologies of all samples were examined using SEM prior to AFM measurement.

4.2.4 Chemical functionalization of AFM tip surface

The surface of AFM probes was functionalized based on Self-Assembled Monolayers (SAMs), in which one end of the molecule forms covalent bonds with the tip surface, leaving the other end exposed with the specific functional group. We focus on grafting molecules with high degree of polarity and nonpolarity on the probe to determine the adhesive interactions between the 2 different probe terminals and various talc particles. For the probe with highly polarized terminal, in which 11-Mercaptoundecanoic acid (95%, Sigma-Aldrich) was used [139]. Briefly, the gold-coated tip (ContGB-G, Budget Sensors, Innovative Solutions Bulgaria Limited, Sofia, Bulgaria) was first immersed in a Piranha etching solution (concentrated H₂SO₄: 30% H₂O₂ in the ratio 7:3) for 10 minutes, washed 3 times with deionized water and ethanol, and then dried under a nitrogen flow for 10 minutes to remove organic contaminants. Lastly, the tip was immersed in 4 mM of 11-Mercaptoundecanoic acid for 12 hours for

the monolayers that were terminated with COOH functional groups to covalently form on gold surface, resulting in the COOH-terminated tip. On the other hand, HDTMS was used to form methyl-terminated monolayers on the AFM probe (CH₃-terminated tip), that have nonpolar or superhydrophobic characteristic due to their long chain of hydrocarbon. The procedure consisted of two main steps, a pretreatment of the probe surface and the silanization process. The pretreatment was performed to remove organic contaminants on the tip surface. In this step, the silicon tip was first washed with ethanol and water, dried in an oven at 120°C for 10 minutes, and then immersed in 0.5 M NaOH for 20 minutes, in 0.1 M HCl for 20 minutes, and in 0.5 M NaOH for 10 minutes. After that, they were rinsed with 0.1 M HCl and deionized water before left to dry in an oven at 120°C for 10 minutes. The activation for generating hydroxyl group on the tip surface was performed through an immersion of the tip in a Piranha solution for 30 minutes before SAM formation. In the silanization step, the pretreated tip was immersed in a 5 mM of HDTMS solution which had been prepared by dissolving the as-received HDTMS solution in dehydrated toluene (QRëC, Chem-Supply Pty Ltd.), for 12 hours at room temperature. The schematic representations for the proposed configurations of probe surface after modification are shown in Fig.19.

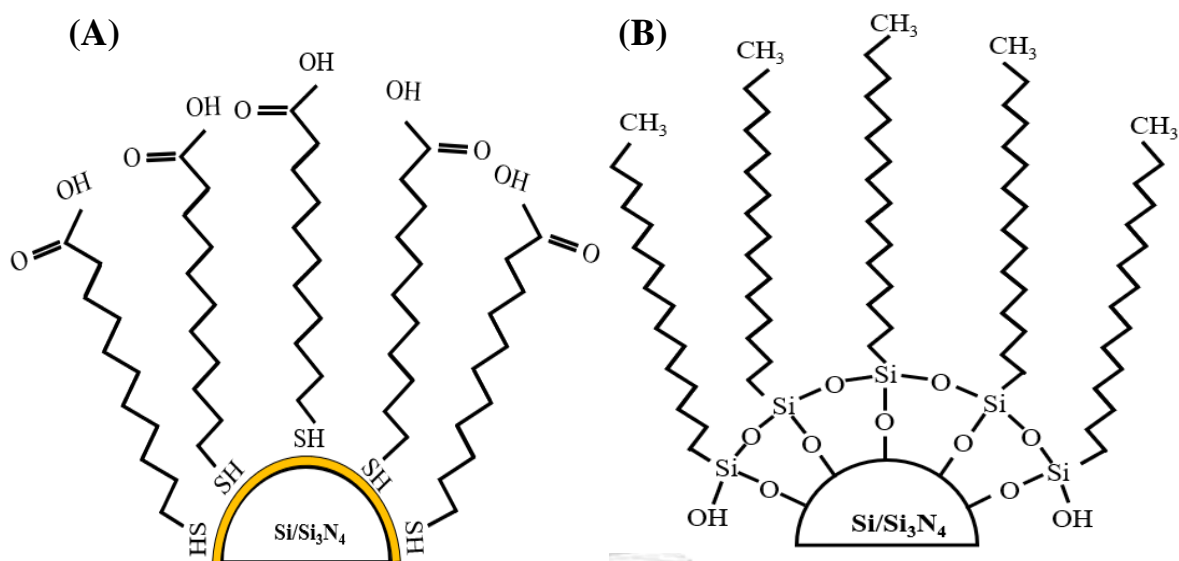


Figure 19 AFM-probe surface modification with (A) 11-Mercaptoundecanoic acid and (B) HDTMS to form carbonyl (-COOH) and methyl (-CH₃) groups on the outermost layer, respectively.

4.2.5 AFM Measurements and analyses

An AFM measurement was performed in non-contact mode for imaging the surface topography of the sample using the V-shaped silicon cantilevers (ACTA, Applied NanoStructures, USA), of which the nominal spring constant is 48 N/m and tip radius is < 10 nm. All images were acquired in ambient condition (at room temperature and atmospheric pressure). The resolution of each image is 512 x 512 lines, with a scan rate of 0.2 Hz. The scan size that were used to locate the particles/particle clusters was approximately 3 x 3 μm². AFM images were processed using Scanning Probe Image Processing (SPIP) software (Image Metrology, Lyngby, Denmark). For the adhesive force measurement, the system was switched to operate in the contact mode. The contact-mode silicon probe and the contact-mode DLC-coated silicon probe (ContAl, Budget Sensors, Innovative Solutions Bulgaria Limited, Sofia, Bulgaria) with

nominal spring constants (k) of between 0.07 and 0.4 N/m (from supplier) as well as the surface-modified probes previously mentioned were used throughout the experiments. Before conducting the force measurements, these probes were calibrated by using thermal tuning method, which was performed in air over a glass slide substrate at room temperature. The actual spring constants of the silicon probe and the DLC-coated silicon probe varied in the range of 0.187-0.211 N/m and 0.226-0.258 N/m, respectively. A maximal adhesion force can be extracted from a force-distance curve, which records the interaction force at various vertical positions the probe when the probe approaches the sample and retracts. The primarily acquired data of the photodiode voltages (V) at the piezoelectric's height positions (Z), were converted to the force-distance curves. In each experimental condition, 60-70 curves were obtained for a good statistical validation. Throughout all AFM experiments, the relative humidity was controlled in the range of $30 \pm 2\%$, the temperature was kept at 25 ± 2 °C.

4.3 RESULTS AND DISCUSSION

4.3.1 Morphology of talc particles

To examine the effects of coupling agents on talc particle morphology, we acquired SEM micrographs and AFM topographic images before and after surface modification in Fig.20A-D and 20E-H. The SEM micrographs were employed to inspect talc readily available after the treatment for a wider perspective inspection while the representative AFM images were used to consider individual talc particulates attached on the silicon substrate and to locate the region to perform force spectroscopy reported in the section below. Compared with the unmodified talc with $\sim 4\text{-}5\ \mu\text{m}$ lateral length represented in Fig.20A, talc that was treated with hydrochloric acid shown in Fig.4.3B appear in planar pellets reduced size of $\sim 300\ \text{nm}$ (or less) – $3\ \mu\text{m}$. The stacking of talc lamellar platelets is not as ordered, that is, the majority of fragmental sheets are randomly piled. The ordered Vs. random stacking features were also observed in the AFM images of the representative single pellets also shown in Fig.20E and 20F. The lateral extent (width/length) of the lamellar in HCl-treated talc were smaller ($\sim 50\text{-}300\ \text{nm}$) than that of the unmodified talc ($\geq 300\ \text{nm}$). The decrease in talc particle size after HCl treatment was likely due to the cracks of the larger platelet as several fissures were observed in the remaining (and relatively large) leaflets. These clefts could result from the increase in hydrophilicity of the sheet surface that had been treated with the acid [140]. Another potential origin of the cleavage is the withdrawal of some other minerals within talc by the acid [141]; these previously existing impurities (calcite, dolomite, magnesite, and chlorite) could function as spatial binders for brucite and silica tetrahedron portions within unmodified talc sheet.

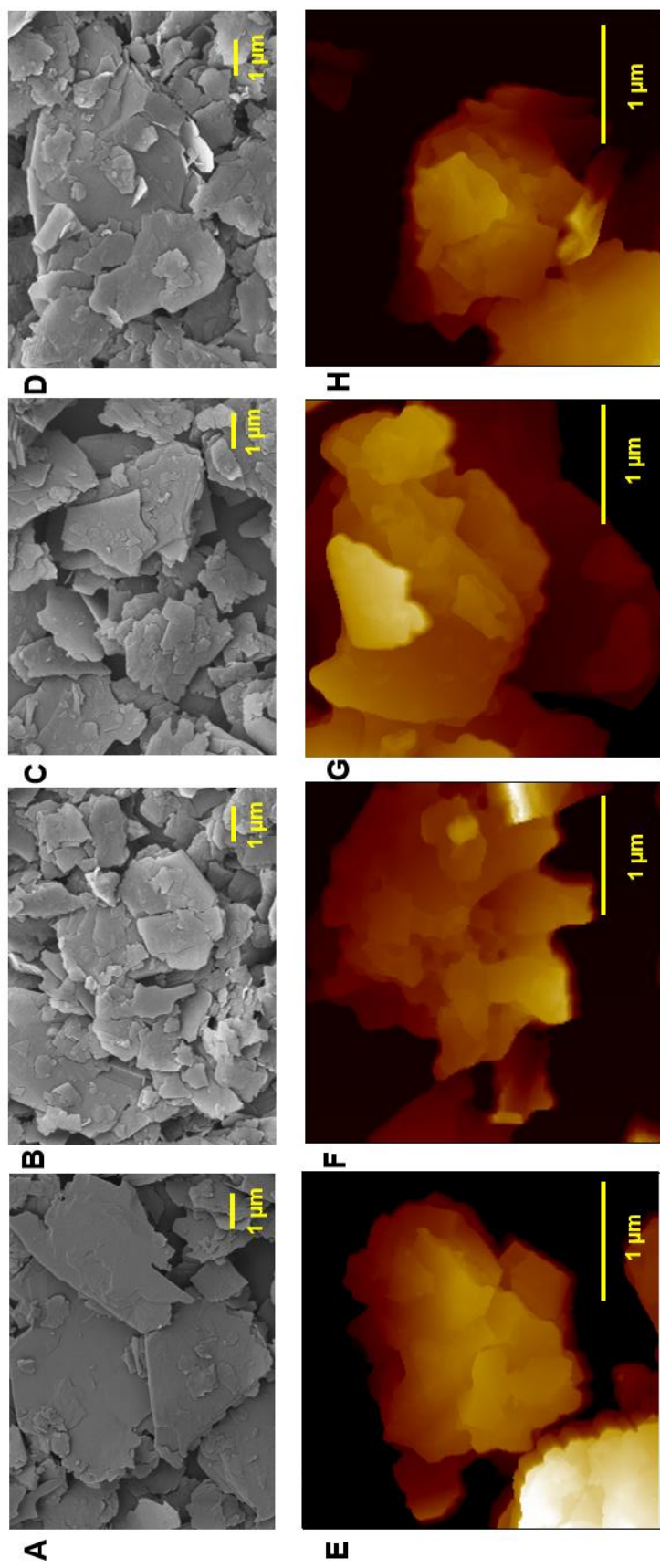


Figure 20 The representative SEM-micrographs and AFM topographic images of talc: (A and E) unmodified talcum powder, (B and F) acid treatment, (C and G) surface modified with APTMS and (D and H) surface modified with HDTMS, respectively.

The color scale in E through H represents 0 nm (darkest) 850 nm (brightest)

The results of organofunctional silanes grafting on talc powder were shown Fig.20C and 20D respect to the unmodified talc. Exhibited in Fig.20C, the talc that underwent surface modification by Aminopropyltrimethoxysilane (APTMS), has lateral size from ~ 400 nm – up to $4 \mu\text{m}$. Although the reduction of lamellar lateral size was also observed in talc treated with APTMS, the higher degree of the leaflet stacking was preserved, if compared to the hydrochloric acid modification (Fig.20B). In addition, the amount of random piling of the platelets of APTMS-grafted talc was less visible than that of HCl-treated talc. An individual particle examined by AFM in Fig.20G portrays size of the lamella sheet of ~ 200 – few μm piling on top of each other and cracks were less observed in talc particles after APTMS treatment. Lastly, the talc modified by Hexadecyltrimethoxysilane (HDTMS) was shown in Fig.20D and 20H. The overview appraisal in Fig.20D reveals sizeable talc particle leaflets of width at least $5 \mu\text{m}$ and some very small leaflets of width smaller than $2 \mu\text{m}$. Since this treatment makes talc surface more electrically insulating than that of the unmodified talc and that of talc treated with HCl and APTMS, it is more difficult to obtain highly resolved features on the talc clump by SEM. From our available observation, the lamellar leaflets appear large, and the small sheets have the width close to $1 \mu\text{m}$ which is similar to those small leaflets in the unmodified talc shown in Fig. 20A. Moreover, the lamellar stacking of HDTMS-grafted talc was not clearly discerned—the piling of the talc sheet was found to scatter on the large aggregate, in spite of showing some degree of randomness as shown in Fig.20D. The enlargement of HDTMS-treated talc particles respect to unmodified talc particles could result from the coagulation enabled by the HDTMS treatment. Similar tendency for the aggregation was also found in AFM observation. Fig.20H displays the observation from AFM whose features of the lamellar leaflets and

lamellar stacking appear more similar to those from silane grafting talc (Fig.20G) than those from HCl-treated talc (Fig.20F). Furthermore, the representative structure of HDTMS-grafted talc particles appears as a pile of leaflets that have unequal width as compared with the unmodified talc particles.

4.3.2 Characteristic of surface-modified talc

FTIR spectra of all talc samples are shown in Fig.21. Characteristic absorption bands of talc at 670, 1018, and 3677 cm^{-1} , corresponding to Mg–OH vibration [142], asymmetric vibration of Si–O– bonding [143], and fundamental mode of OH vibration [144], respectively are clearly visible. Small signal from adsorbed water at 1654 cm^{-1} [145] is also detected in all samples. XPS spectra in Fig.22A show that the native talc reveals only one type of Si2p signal at 103.0 eV corresponding to the Si(–O)₄ binding environment [86], while two types of Mg1s signal were detected, i.e., the dominating peak at 1302.8 eV from Mg–OH and the minor peak at 1304.8 eV from Mg in talc crystals [146]. These results were verified from the O1s spectra, which were deconvoluted to two peaks at 531.9 eV for Si–O–Si from SiO₄ tetrahedron of talc and at 533.6 eV from hydroxyl group [88]. The results confirmed that hydroxyl groups in talc are bonded with Mg and no silanol group was presented in the sample.

After the acid treatment, it was observed that the intensity of the FTIR signal at 670 cm^{-1} was increased relative to the signal at 1018 cm^{-1} , indicating that the acid induces hydrolysis of the talc. The fact that the position of the band at 3677 cm^{-1} was not shifted confirms that Mg within the lattice was not affected by the acid [144]. Nevertheless, the structure of SiO₄ tetrahedron in siloxane basal planes of the talc was greatly affected by the acid treatment because the band at 1018 cm^{-1} was split into two

bands at 1080 and 1000 cm^{-1} , corresponding to asymmetric Si–O–Si bonding of amorphous silica [147] and Si–O stretching of talc [148], respectively. It was confirmed by Si2p XPS spectrum in Fig.22B, in which the signal at 103.7 and 101.7 eV, corresponding to silicon in $\text{Si}(\text{O})_{2-x}(\text{OH})_{4-2x}$ [149] and in Si–O dangling bonding [150]. The formation of the dangling Si–O bonding was also confirmed by O1s signal at 530.9 eV [88], while the hydroxide in the silanol group on the surface was supported by high O1s signal at 533.6 eV. It should be noted that the signal from hydroxyl group on the surface of acid-treated talc was expected to come from the newly created silanol group because all magnesium on the surface was leached out by the acid as witnessed from the absence of Mg1s signal.

For the organosilane grafting, the process did not affect Mg–OH structure of the talc since the FTIR bands at 670 and 3677 cm^{-1} in Fig.21 and the Mg1s XPS spectra in Fig.22 remained unchanged. The grafting was successful because the XPS signals from Si–O in silanes were observed at 102.2 eV in Si2p spectra [87] and at 530.9 eV in O1s spectra [88]. Moreover, the FTIR signatures of the silanes used, i.e., NH_2 stretching absorption band at 1562 cm^{-1} for APTMS [91] and the bands at 2856 and 2929 cm^{-1} corresponding to CH_2 and CH_3 of HDTMS [93], were detected. The FTIR band at 1040 cm^{-1} in APTMS-modified sample, which was also observed as a shoulder peak in HDTMS-modified sample, was expected to be the result from Si–O–Si bonding between silicon from the silane and silicon on the surface.

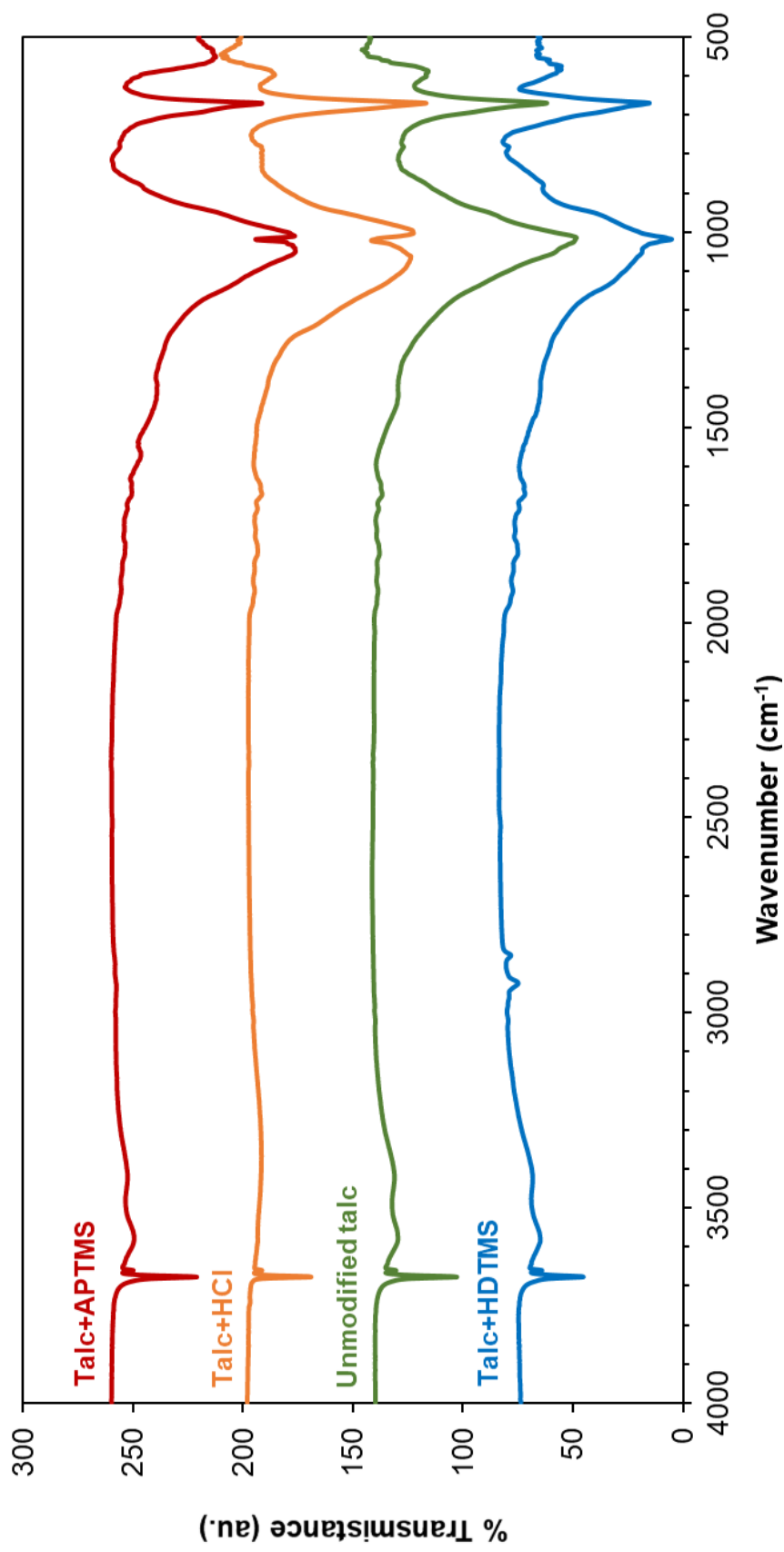


Figure 21 FTIR spectra of surface-modified talc in each condition.

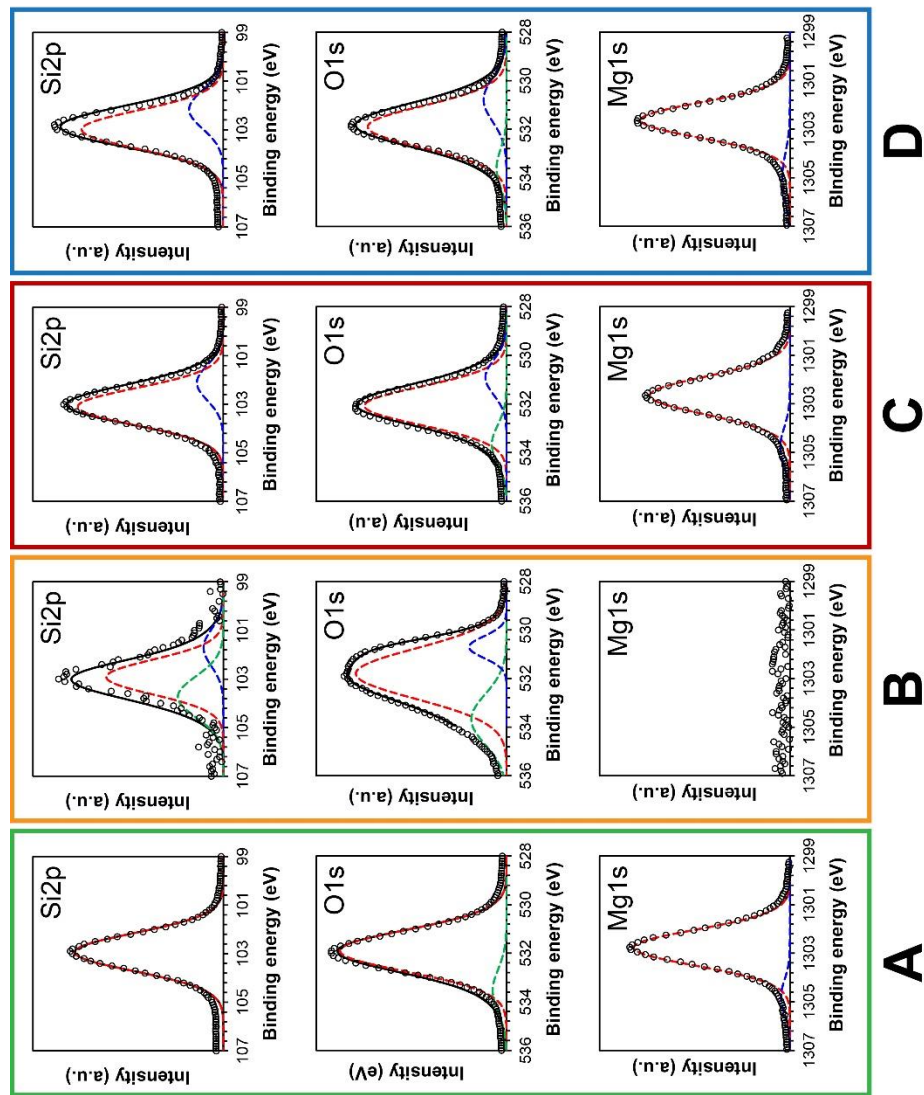


Figure 22 High-energy resolution Si2p, O1s and Mg1s XPS spectra of talc particles after surface modification with (A) unmodified talc, (B) HCl treatment, (C) APTMS and (D) HDTMS.

4.3.3 Characteristic of the modified AFM probes

Since the surface functionalization of the AFM probes was the same as our previous work [151], detailed characterizations of the modified tips will not be discussed herein. In essence, the tips were analyzed by XPS (ULVAC-PHI, PHI 5000 VersaProbe II) with Al K α radiation from synchrotron as the excitation source. The X-ray beam was focused on the cantilever of the AFM probe. For the MUA-modified probe, the COOH group was the terminal functional group protruding from the probe surface, as evidenced by XPS O1s spectra at 532.5 and 533.5 eV as well as by XPS C1s spectra at 286.2, 287.3 and 289.0 eV, all of which represent different parts of COOH functional group [152, 153]. On the other hand, for the formation superhydrophobic monolayer on the AFM probe, the binding of the HDTMS to the tip surface was confirmed by the presence of Si–O bonding in Si2p and O1s spectra at 102.2 and 530.9 eV, respectively. The CH₃-terminal group was detected from C1s spectra at 284.7 eV.

4.3.4 Effects of modified surface on the talc structure

Theoretically, the hydrophilic characteristic of talc is originated from the presence of silanol (-SiOH) or (-MgOH) groups at the edge of the surface. Most part of the talc surface, but not at all the surface is hydrophilic. Its relatively high electrical charge renders to its polarity in water. It is necessary to generate new silanol on the surface in order to increase the hydrophilicity [154]. For acid treatment, the reaction process is done by using hydrochloric acid reacted with siloxane bonds (Si-O-Si) on the talc surface. The new silanol groups could be generated, which is acted as the polar surface. This reaction leads to the enhancement of hydrophilic sites because either talc-OH or silanol group is formed on the surface. Also, different silanes coupling agents

are used for surface modification since they are the efficient substances extensively used in composites and adhesive formulations [155]. The reaction is occurred from an organosilane's silicon functional group that react with talc's reactive hydroxyl groups. The concomitant condensation of silanols (aging) also take place, producing a stable covalent bond and a stable layer on the talc surface. Moreover, the length of alkyl spacer between the silane organo-functionality and the silicon atom also influences the interaction force. These findings are in agreement with the previous study which is found that the shorter alkyl spacer is leading to the higher reactivity of alkoxy groups because of its stronger electron interaction between the functionality (X) and the silicon atom [156]. According to these findings, the surface modification with silane molecules or treatment with acids may not only change the physical/chemical properties, but also affect the agglomeration of clay minerals. Therefore, the dispersion of talc particles is investigated both of before and after surface treatments by using the hydrophobicity /hydrophilicity test at macroscopical level as shown in Fig.23.

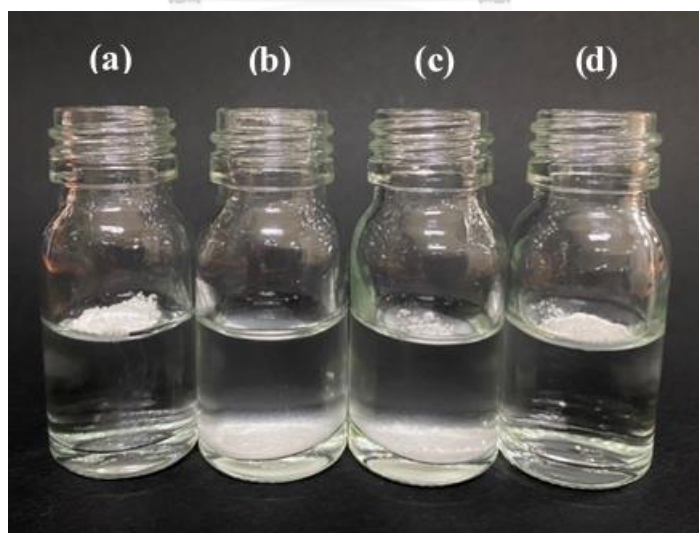


Figure 23 Surface affinity test of (a) unmodified talc particles, (b) HCl-treated talc, (c) APTMS-grafted talc and (d) HDTMS-grafted talc.

According to the water containing-surface affinity test, all unmodified and grafted HDTMS on talc particles are absolutely float at the interface even though their density (talc density = 2.75 g/cm^3) is relatively greater than water. This phenomenon is occurred because of their strong hydrophobic property. On the contrary, treated talc with HCl caused talc particles to settle out completely, leading to the less hydrophobicity of particles and easier dispersed in water. Interestingly, talc particles are partially suspended in aqueous solution after APTMS had grafted on the surface. Some particles tend to gradually dissolve in water when times are prolonged. These findings are supposed to occur from two reasons: (i) the unequal amount of polar portion ($-\text{NH}_2$) contained in each particle and (ii) the modified surface's reaction is not completed; thus, the uniformly characteristic properties of all particles could not be occurred. However, these results are obviously showed that talc particles became hydrophilic due to their easy dissolved in water after using HCl and APTMS treatment. The hydrophobic character still presents after the surface had modified with HDTMS (particles remained suspended in aqueous solution). The floating ability is decreased after the hydrophilic portion in particles had increased.

However, the degree of hydrophobicity was verified by contact angle which measured through liquid. This angle quantifies the wettability of solid surface by calculation the relative strength of molecular interaction of liquid, solid, and vapor molecules in the equilibrium state after water droplets had rolled off the surface. Contact angle values, both of before- and after surface modification, are measured as shown in Table 5.

Table 5 The water contact angle of different surface-modified talc particles

Samples	Water contact angle (deg)
Unmodified talc	62.39 ± 2.18
HCl-treated talc	57.79 ± 1.39
APTMS-grafted talc	50.02 ± 1.94
HDTMS-grafted talc	96.48 ± 4.58

The contact angle of unmodified talc, HCl-treated talc, APTMS-grafted talc and HDTMS-grafted talc are $62.39^\circ \pm 2.18^\circ$, $57.79^\circ \pm 1.39^\circ$, $50.02^\circ \pm 1.94^\circ$ and $96.48^\circ \pm 4.58^\circ$, respectively. Since the initial talcum particles have mildly hydrophobic characteristic and the surface treatment with inorganic acid can lead to the contact angle decreasing, the changing of the surface to hydrophilic characteristic is occurred due to its numerous hydrophilic (silanol groups) formation. The contact angel of particles which coated with APTMS on their surface is extremely low. This effect might occur from a large number of amino ($-\text{NH}_2$) functional group grafted on the surface particles. In contrast, the contact angel of HDTMS-modified particles is increased more than 96° , suggesting a highly hydrophobic property of the coated surface.

4.3.5 Adhesion measurements

Force spectroscopy on talc particles

The interaction forces resulting from the surface modification on talc particles was determined from force-distance curves: the degree of cantilever deflection during

the approach and retraction of the AFM probe. We employed bare silicon probes (or Si tip) to represent physical agents that exhibit hydrophilic property. For the interacting counterpart with hydrophobic surface, we used silicon probes coated with diamond-like carbon (or DLC tip) due to existing sp^3 bonding in the carbon network [157]. Defined as Mohs hardness 1 (lowest) on the Mohs scale of the mineral which can be visibly scratched by most minerals, talc would represent a soft material in bulk; it deforms with significant extent under mechanical stress. When considered together with relatively large adhesions that were generally observed in Fig.24A and 24B, our system of interacting pairs can be appropriately depicted by Johnson-Kendall-Robert (JKR) model [158]. In these force-distance curves, we analyzed their features and observed several tendencies. First, the maximum adhesion force ($F_{ad,max}$) described as the magnitude of the most negative force which attracts the talc surface and the tip, is the most readily recognizable characteristic. As a general trend, the comparison between unmodified and modified talc surfaces that interacted with both hydrophilic and hydrophobic probes reveals that the treatments change their $F_{ad,max}$. Specifically, $F_{ad,max}$ decreases with decreasing hydrophilicity (increasing hydrophobicity) of the talc surfaces: $F_{ad,max}$ of APTMS-grafted talc is greater than those of HCl-treated talc, and of unmodified talc and of HDTMS-grafted talc as shown in Fig.24A. In addition, increase in hydrophobicity of the interacting agents (tips) reduces $F_{ad,max}$ in all unmodified/unmodified particle surfaces (comparing Fig.24A to Fig.24B).

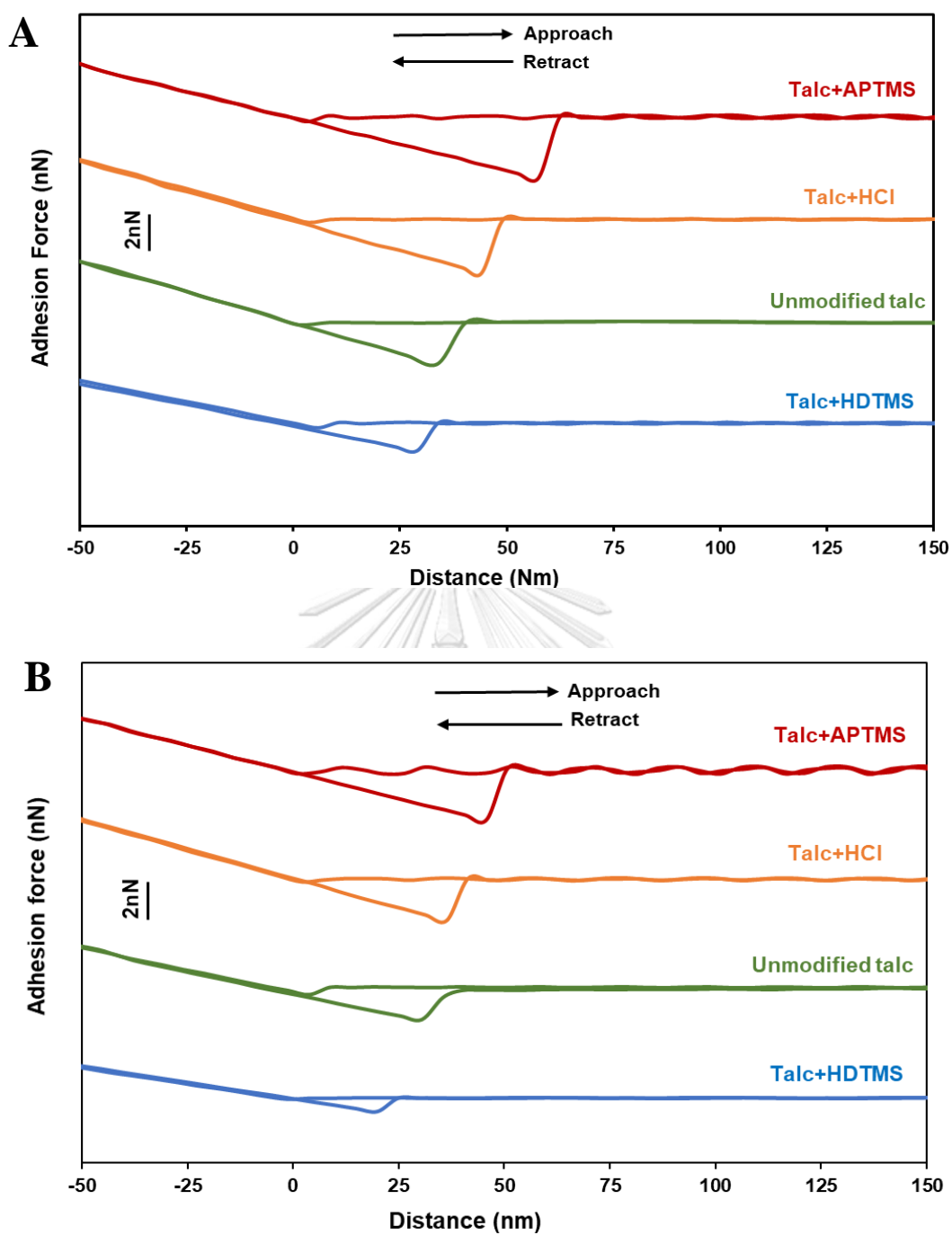


Figure 24 The representative force-distance curves between unmodified/modified talc particles and (A) silicon and (B) diamond-like carbon (DLC) probe.

Second, although not immediately apparent, the slope of the repulsive regime—delineated at the positive interacting forces down to the position of $F_{ad,max}$ during the

retract as well as the left side of zero during the approach— is largest for unmodified talc and becomes slightly lessened for all the treated talc particles that interacted with both Si and DLC probes. This indicates that surface modification either by organosilanization or by inorganic acid treatment talc reduces the stiffness of the talc surface. Another notable feature is the wavy or sinusoidal-like attribute that appeared at zero force region during the approach and retract. The rising and falling of force around zero is ascribed to the bending of the soft cantilever that we used (with spring constant < 0.2 N/m) after experiencing substantial interacting force with soft sample [95]. Therefore, the waviness was more apparent in the probe-surface pairs with stronger interaction as well as softer surface. It is consistent with our observation that the undulation of zero force becomes perceptible in the talc surfaces treated with HCl and its degree is larger in the talc particles grafted with APTMS, but it is rarely observed in unmodified talc powder. The soft cantilever deflection due to considerable interaction could also yield a sudden sharp movement of the probe after the probe retraction reaches $F_{ad,max}$ that we observed in both Fig.24A and 24B. However, for the soft probe with certain (but low) spring constant, the tip flicking at jumped off contact (JOC) is likely to emanate after some threshold value of $F_{ad,max}$ has been reached. Accurate maximum forces can be derived from the statistical analysis of numerous force-distance curve data that obtained under identical conditions. Results of adhesion force extracted from F/D curves are summarized in Table 6.

Table 6 Summarize of adhesion force obtained between different tip types and surface-modified talc.

Surface-modified talc	Adhesion force (nN)			
	Types of AFM tips			
	Silicon tip		Silicon coated with DLC tip	
Unmodified talc	2.85 ± 0.06	1.95 ± 0.07	1.76 ± 0.07	0.86 ± 0.09
HCl-treated talc	3.53 ± 0.11	2.63 ± 0.10	2.25 ± 0.10	1.34 ± 0.09
APTMS-grafted talc	4.00 ± 0.13	3.04 ± 0.10	2.59 ± 0.11	1.76 ± 0.10
HDTMS-grafted talc	2.02 ± 0.09	1.19 ± 0.08	0.72 ± 0.05	0.39 ± 0.04

Eight pairs of the interacted Si/DLC probes and unmodified/modified surface of talc particles are arranged to measure the adhesion force. Both of Si-tips and DLC-tips have the same of adhesion force tendency. the strength of tip-sample's interaction from highest to lowest can be in ordered as APTMS-grafted talc > HCl-treated talc > unmodified talc > HDTMS-grafted talc. Both of Si- and DLC-tips that interacted with APTMS-grafted particles showed the strong adhesion force (2.48–4.13 nN) whereas the weak adhesion force (0.67-2.11 nN) is observed on tips interacted with HDTMS-grafted talc surface. According to the highly adhesion force, the APTMS-modified talc particles, which are contained the amine group at the terminal surface, have a slightly increased in adhesion strength (0.34-0.5 nN) when compared to HCl-treated talc. It is possible that the amine functional groups that coated the talc particles

is higher hydrophilic (or higher polarity) when compared to the silanol groups (-SiOH) generated after acid treatment.

Importantly, an interaction force between unmodified/modified talcum particles and two types of AFM tips can be classified in two modes. Adhesion data were plotted in a histogram and defined by the average and the standard deviation (Student's t test of unequal standard deviation for each modified/unmodified talc particles, $p < 0.05$) as shown in Fig.25. The bimodal distribution is supposed to reflect two types of talc surface which are faces and edges, which are indicate as the anisotropic property [133]. The mean value of the adhesion force in one mode is approximately 1-2 times of those in another mode. Generally, faces surface (basal planes) is composed of Si-O-Si groups, which exhibits hydrophobic property (low surface energy). This property leads to the difficult in dispersion in water. In contrast, the edges surface contained hydrophilic sites (such as SiOH or MgOH) renders to a higher surface energy when compared to the face surfaces. Therefore, the low adhesion force mode possibly reflects the interactions between AFM tips and faces surface of talc particles whereas the higher adhesion force could be observed in tips interacted with the edges surface.

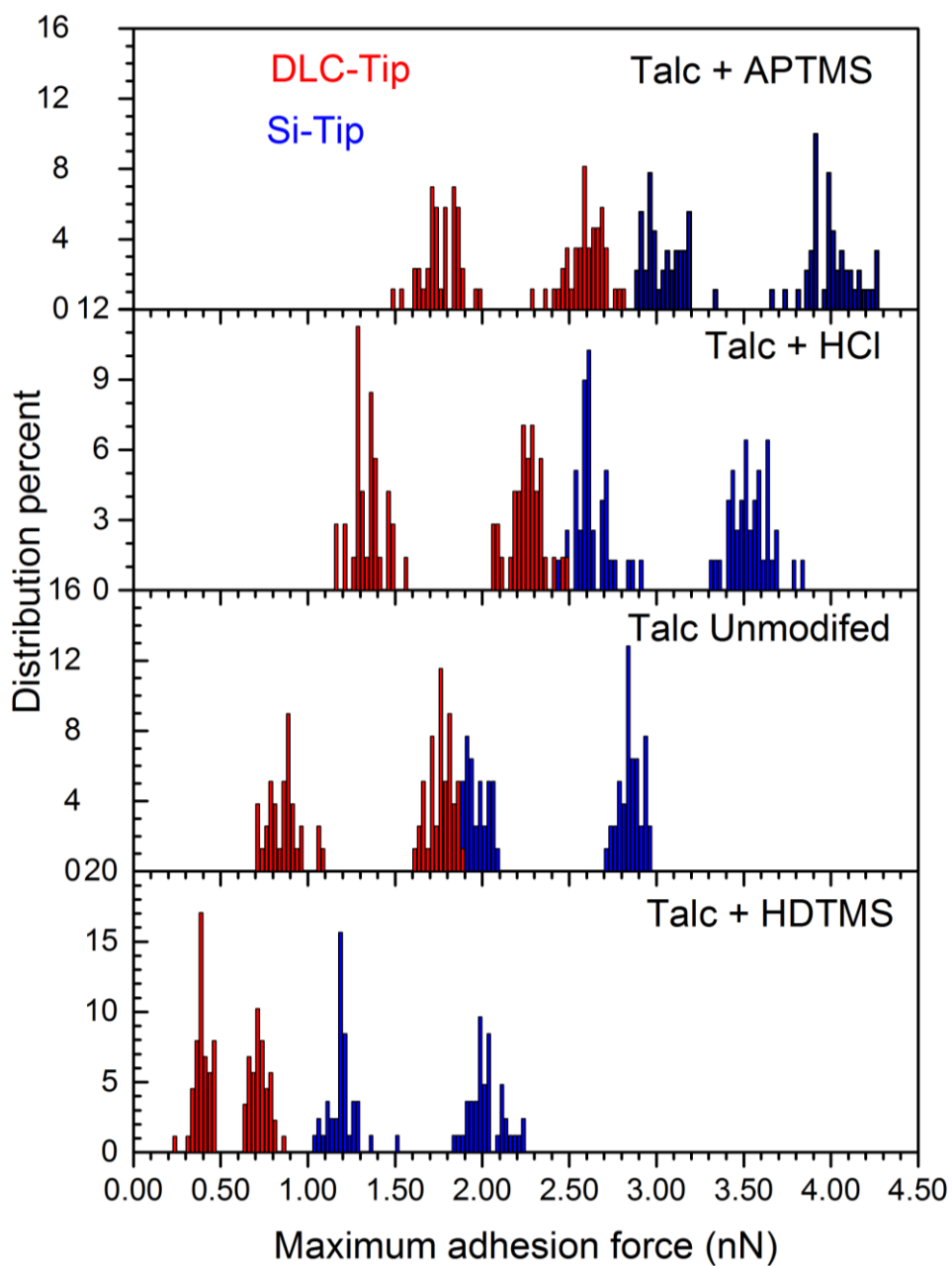


Figure 25 Histogram represent the bimodal fashion of the adhesion force obtained between Si /DLC tips and unmodified/modified talc particles.

Additionally, the important factors that affect the adhesion force after surface modification is molecules types that terminated talc particles. For example, talc

particles which are modified with APTMS are found to be increased in ratio of hydrophilic parts over hydrophobic surface. The Si-O-Si on faces surface that cross-linking and protruding the -NH_2 molecules on the outer layer of talc particles (confirmed by XPS analysis) resulting in the strongest adhesion. Similarly, HDTMS grafted on talc particles leads to the formation of -CH_3 terminated surface structure. However, since the HDTMS is a superhydrophobic molecule due to composed of a long-chain hydrocarbon, resulting in low adsorption sites and weak of adhesion force.

Effects of chemically-modified AFM tips on adhesion forces

According to the statistical tests (see detail in Appendix B), the adhesion forces that measured from Si-tip is significantly different from DLC-tip. Data were described under the 95 % confidential hypothesis based on the linear regression model. This result is pointed out that types of AFM tip surface are directly affect the adhesive forces. To confirm this observation, the chemically-modified AFM tips through chemisorption with Self-assembled monolayer (SAMs) method were also conducted. This process implies by attaching specific molecules on AFM tips and recording force-distance curve between modified tips and particles of interest. In this work, the strong hydrophilic and hydrophobic molecules at the terminal probe are carboxyl (-COOH) and methyl (-CH_3) group, respectively. Chemical bonds and functional groups attached on the tip surface were characterized by XPS analysis. In our experiment, a minimum of 50 individual force curves were assessed for the extreme condition of modified particles and different terminate AFM tip surface. The average of maximum adhesion forces and the standard deviations were extracted from these F-d curves. Comparison of adhesion forces for bare and modified AFM probes is exhibited in Fig.26.

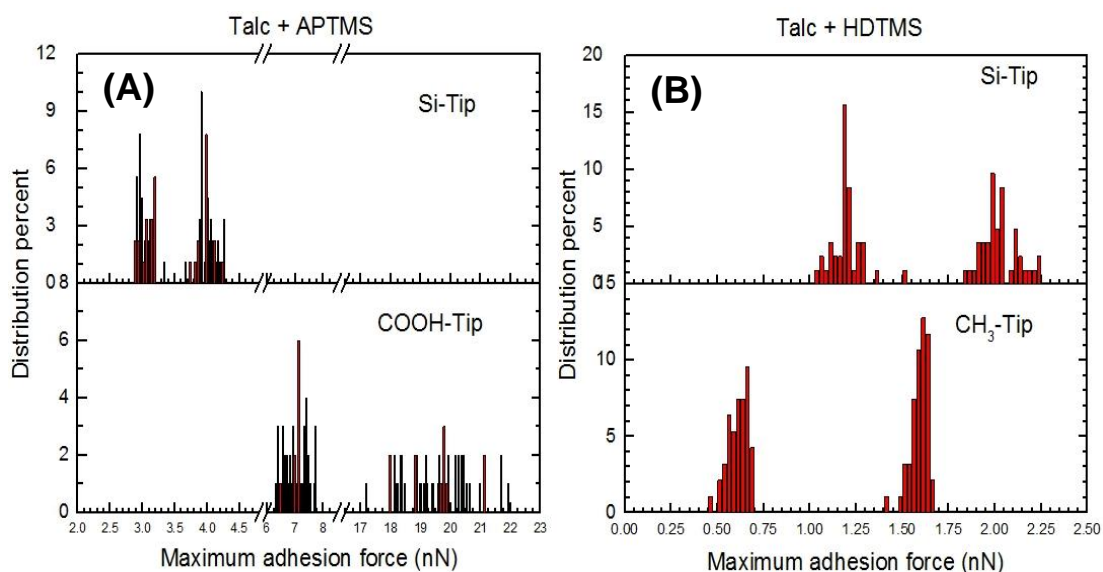


Figure 26 Adhesion forces of the interactions between functionalized/non-functionalized probes and modified talc particles with (a) APTMS and (b) HDTMS.

The adhesion force between APTMS-modified talcum powder and the COOH-terminated probe is approximately 19.52 ± 1.07 nN. There is increasing up to 5 times when compared to the unmodified silicon tip (4.00 ± 0.1 nN) as shown in Fig.4.9(A). The maximum adhesion values of the modified tip surface are intensively high as indicated by large pull-off forces. The significantly increased adhesion force observed between carboxyl group-terminated tips and talcum powder-grafted APTMS is attributed to the hydrophilic-hydrophilic interaction. In contrast, the weakest adhesion force is observed on the tip terminated with hydrophobic (methyl) group contact with HDTMS-grafted talc particles, as seen in Fig.4.9(B). The adhesion force of CH_3 -terminated tips is approximately 1.59 ± 0.04 nN, which is weaker than those found in silicon probe. Because the oxide layer could form naturally on the silicon probe; therefore, the terminated tip surface is quite polar. In terms of AFM tips's property

similarity, both of DLC and CH₃-terminated probe are defined as nonpolar surface because of their covering with hydrophobic molecules. Nevertheless, strong adhesion forces are likely to be observed in the CH₃-terminated probe. These results suggested that the increasing of interaction force is associated with the length of alkyl chain on the probe surface [159]. SAMs modified tips has potential to enhance van der Waals interaction because of an entwining of alkyl groups and a lot of molecules which are able to interact with other surfaces. Therefore, these findings indicated that it is not only the hydrophobic/hydrophilic effect, but also types of molecules protruded on the surface that dominate the adhesion forces.

Hamaker constant estimations

The total van der Waals (vdW) interaction potential is inversely proportional to the 6th power of the distance which, in our consideration, is the tip-sample separation distance (d):

$$U_{vdW} = -\frac{C_{vdW}}{d^6} \quad (1)$$

where C_{vdW} is the proportionality constants for the total van der Waals energy. Although C_{vdW} of the interacting tip-sample pairs is theoretically contingent on the pair's electric properties in bulk such as macroscale dipole moments ($\vec{\mu}$) and polarizability (α) [160], it can be experimentally obtained from the Hamaker constant (A_H), [161] through the relationship:

$$A_H = \pi^2 C_{vdW} \rho_1 \rho_2 \quad (2)$$

where ρ_1 and ρ_2 are the number of atoms per unit volume of the tip and sample pair. According to the manufacturer, the coating of diamond-like carbon on Si (or to native

SiO₂ at the surface) for the DLC probe that we employed is ~15 nm thick. Comparably, the ratios between the number of silane molecules—APTMS or HDTMS that made up the probe terminals—and the number of native SiO₂ at the surface of the silanized probes were of similar values as determined by the XPS measurements. With the approximation in volume density over of the entire probe (of at least 261 μm³), we neglected the varied volume contributed by the surface treatment <1% (within the order 1 μm³). As a consequence, the total number of atoms/molecules at the probe terminal together with the Si probe per volume (ρ_1) could be assumed to be similar regardless of the types of probe terminal modification. In addition, the total number of different atoms per volume (ρ_2) within the bulk talc particles was estimated as the concentration of atoms in the crystal lattice of monoclinic talc whose unit cell is characterized by edge lengths $a = 5.26 \text{ \AA}$, $b = 9.10 \text{ \AA}$, $c = 18.81 \text{ \AA}$ and the inclined angle $\beta = 80^\circ$ [162]. Our XPS results showed the congruent values of ratio between the amount/signal of Si-OH, -NH₂, and -CH₃ and the amount/signal of SiO₂ in the talc powder treated with HCl, APTMS, and HDTMS, respectively. Similar to the consideration for the interacting probes, the volume contributed by the surface modification that amounted to <1% (~within the order 6 μm³) was negligible compared to the volume of a typical talc particle (~ 10 x 10 x 10 μm³). Hence, ρ_2 was considered identical in all the talc particles that were unmodified, treated with HCl, APTMS and HDTMS. Using these assumptions, we were able to compare the Hamaker constants of interacting pairs of the various unmodified/modified talc facets and different Si-based probes and directly refer their tendency to that of the total van der Waals constants. To determine the Hamaker constant, we first converted our force-distance (F - z) curve in the approach

portion to the force and tip-sample separation distance (F - d) curves using the relationship

$$d = z + z_c = z + \left(-\frac{F}{k_c}\right) \quad (3)$$

where F is the measured interaction force between the tip and the sample, k_c is the cantilever spring constant and z_c is the cantilever deflection defined to be positive when the cantilever bends towards the sample as the example shown in Fig.27. The relationship of the force (F) and tip-sample separation distance (d) on the right portion from the minimum force:

$$F(d) = -\frac{A_H R}{6d^2} \quad (4)$$

where R is tip radius (the nominal value that we used in the calculation was 10 nm), allowed us to determine the Hamaker constant characterizing each force-distance curve.

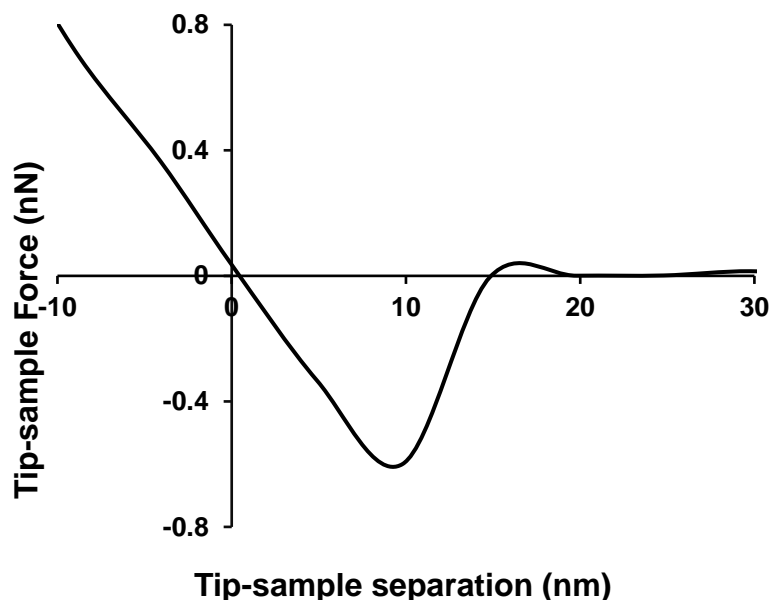


Figure 27 An example of the force and tip-sample separation (F - d) curve from the unmodified talc powder that interacted with the COOH-terminated probe.

Generally, the adhesion force is the combined effects from several interactions, such as ion-ion interactions, capillary force, electrostatic attraction and van der Waals (vdW) interactions. Since charges on the talc surface is completely neutral and the relative humidity (%RH) of all experiments is effectively controlled at the level less than 30%; therefore, the ion-ion interactions and the capillary force can be neglected. Moreover, it is well known that the elemental layers of talc are linked by van der Waals bonds. Hence, all of experiments, the vdW interactions are hypothesized as the important force in adhesion phenomena. The strength of vdW forces is directly correlated to the Hamaker constant (A_H), which is the value derived from all interacting molecules-pairs in the bodies. The calculated A_H of each condition is shown in Table 7.

Table 7 Estimated Hamaker constant between talc-modified surface and AFM tips.

Calculated A_H ($\times 10^{-21} \text{J}$)		
Surface-modified talc	Type of AFM tips	
	Silicon tip	Silicon coated with DLC tip
Unmodified talc	28.51 ± 2.33	7.29 ± 1.16
HCl-treated talc	48.23 ± 2.15	17.24 ± 1.44
APTMS-grafted talc	79.25 ± 3.05	19.76 ± 1.03
HDTMS-grafted talc	13.66 ± 1.05	3.79 ± 0.28

The tendency of A_H , which is calculated from F-d curves, is consistent with the adhesion force. The hydrophilicity and hydrophobicity of talc particles are directly affected to the A_H , which can be used to imply the strength of vdW interactions. Surface treatments with HCl acid and APTMS indicate the highly hydrophilic characteristic; in other words, the enhancement of the polar portion on molecules leads to the increased in A_H . In contrast, the A_H derived from the HDTMS-grafted talc particles is significantly decreased, resulting from the net structure of modified particles became less polar (increasing hydrophobic portion) molecule. According to the tendency of A_H , these results are pointed out that the interaction of the hydrophilic-hydrophilic pairs is stronger than hydrophilic-hydrophobic pairs. At the same time, the interaction of the hydrophilic-hydrophobic pairs is stronger than hydrophobic-hydrophobic pairs as well. For the clearly visible, the A_H derived from the tip functionalization with strong hydrophilic/hydrophobic groups and modified/unmodified particles is needed to be calculated and compared. Some conditions were determined as shown in Table 8.

Table 8 Estimated Hamaker constant between the different terminated surfaces of AFM tip and modified/unmodified talc particles.

Surface-modified talc	Calculated A_H ($\times 10^{-21} J$)	
	Types of tip modification	
	COOH-terminated tip	CH ₃ -terminated tip
Unmodified talc	88.27 ± 2.27	10.49 ± 0.31
Talc + APTMS	452.60 ± 3.40	-
Talc + HDTMS	-	6.27 ± 0.63

In order to confirm the magnitude of vdW interactions, the strongest A_H is calculated from the interaction between a COOH-terminated probe and APTMS-modified talc. While the weakest A_H is observed from the CH₃-terminated probe and HDTMS-grafted talc particles, the A_H in hydrophilic-hydrophilic attractions is higher than hydrophobic-hydrophobic interactions approximately two order of magnitude. These results can be concluded that the changing tendency of the Hamaker constant is in accord with the relative strength of vdW interactions. Also, the modification of the AFM-probe surface using different types of molecules affect the adhesion.

4.4 CONCLUSION

Concepts of chemically modified talc particles and AFM-based force spectroscopy for the specific case using functional groups exhibited hydrophilic and hydrophobic characteristics had been demonstrated. It is possible to apply these concepts to other types of functionality in several areas. The adsorption sites of talc surface (edges sites and basal planes) could be postulated by measuring adhesive forces between treated-talc particles and non-functionalized/functionalized AFM tips. The changing of adhesive forces is consistent with the calculated Hamaker constant, which represents the strength of van der Waals interactions. In this surface studies, the strong adhesion of the hydrophilic tips (Si-tips) interacts with hydrophilic particles (HCl- and APTMS-treated talc) is observed. The increasing of strong adhesion had occurred when silicon probes was replaced by a COOH-functionalized AFM probes, giving evidence of intermolecular forces is predominant. Furthermore, the weak adhesion force is found in the condition of modified particles and AFM probe with HDTMS. This weak force is supposed to occur from the hydrophobic-hydrophobic attractions. These changings in adhesive force can be partly explained by the JKR theory. The identification of surface's interaction forces is very useful in the adhesion and adsorption studies. These knowledges can be used to predict the manners of functional groups distributed on samples. Moreover, they can be used to interpret in terms of the specific interactions between two surfaces and can be used for improvement of the chemical properties in others clay minerals.

CHAPTER V

CONCLUSION AND RECOMMENDATION

5.1 Conclusions

The dissertation first investigated the effects of catalyst surfaces on adsorption in the diuron's photocatalytic degradation over zinc oxide. AFM-based force spectroscopy elucidated the various functional groups of diuron (reactant)'s adhesion behavior on different ZnO (catalyst) surfaces to be physical adsorption. The functionalization of AFM tip surface with various molecules resembling the functional group of diuron distinguished and identified the Zn or O-terminated surfaces of conventional ZnO particles and the surface of ZnO nanorods. The results suggested that the functional group's polarity of the reactant and the atomic arrangement of the catalyst surface determined the preferential absorption configuration. Analysis of the Hertz model and Hamaker constants indicated that the electrostatic intermolecular attractions amounted to vdW interactions mainly governed the adsorption behavior of diuron molecules onto the ZnO catalytic surface. Another portion of the thesis describes how the surface treatments alter talcum particles' adhesion to various surfaces in the view of hydrophobicity/hydrophilicity, which affects the particulate ability to disperse, wet, and agglomerate. We found that surface modification changed hydrophilic and hydrophobic sites' ratio on the two types of the particle's exposed surfaces: face and edge surfaces. The increased hydrophobic portion, corresponding to the observed high contact angle, reduced the measured adhesion forces. We found a correlation between adhesion and

hydrophobicity/hydrophilicity of the talcum particles: the strong adhesion in hydrophilic-hydrophilic attraction and the weak adhesion in hydrophobic-hydrophobic attraction. Similarly, our results suggested that vdW interactions predominately dictate the hydrophobic effects in talcum adhesion. The extension of our findings would aid the explanation of the adhesive behaviors of talcum on the microelectronic structures as well.

5.2 Recommendation and Future directions

Based on all the experimental findings presented in previous chapters, we obtained a fundamental understanding of particle interactions with both surfaces and molecules through the direct force measurement using AFM in ambient conditions. However, our study scope limited to the AFM operation in the air suggests abundant opportunities for the use of AFM to examine particles' interactions with molecules or surfaces of interest in other media: electrolyte solution or solvents. Such operation is possible because AFM allows the acquisition of the interaction force/energy data regardless of the medium. The unique advantage of AFM could lead to new understanding associated with adsorption and adhesion mechanism of both talcum and ZnO, e.g., the roles of zeta potential distribution, electrostatic double-layer interactions, and ionic strength in aqueous solutions. The appropriate model to describe the interaction in these media includes DLVO (Deryaguin-Landau-Verwey-Overbeek). Previous studies have used the DLVO model to predict the repulsive hydration force for hydrophilic surfaces, the attractive hydrophobic force for hydrophobic surfaces, and the repulsive steric force [163]. The comprehensive insights derived from the interactions of talcum/ZnO particles and surfaces/diuron molecules in various media would enable us to conceive effective solutions for removing talcum particles from the

solid surface in microelectronic devices and to empower us to control the diuron adsorption configuration for harmless photodegradation.



REFERENCES



จุฬาลงกรณ์มหาวิทยาลัย
CHULALONGKORN UNIVERSITY

1. Cooper, D.W., H.L. Wolfe, J.T. Yeh, R.J.J.A.S. Miller, and Technology, *Surface cleaning by electrostatic removal of particles*. 1990. **13**(1): p. 116-123.
2. Wang, B., Y. Wang, C. Liu, X. Feng, G. Yang, and H. Wang, *Achieving accelerated osteogenic differentiation via novel magnesium silicate hollow spheres*. *New J. Chem.*, 2015. **39**(12): p. 9722-9728.
3. Tan, C.L.C., S. Gao, B.S. Wee, A. Asa-Awuku, B.J.R.J.A.S. Thio, and Technology, *Adhesion of dust particles to common indoor surfaces in an air-conditioned environment*. 2014. **48**(5): p. 541-551.
4. Taspinar, O.O. and S. Ozgul-Yucel, *Lipid adsorption capacities of magnesium silicate and activated carbon prepared from the same rice hull*. *European Journal of Lipid Science and Technology*, 2008. **110**(8): p. 742-746.
5. Krysztafkiewicz, A., L.K. Lipska, F. Ciesielczyk, and T.J.A.P.T. Jesionowski, *Amorphous magnesium silicate—synthesis, physicochemical properties and surface morphology*. 2004. **15**(5): p. 549-565.
6. Wu, Z., T. Tang, H. Guo, S. Tang, Y. Niu, J. Zhang, W. Zhang, R. Ma, J. Su, C. Liu, and J. Wei, *In vitro degradability, bioactivity and cell responses to mesoporous magnesium silicate for the induction of bone regeneration*. *Colloids Surf B Biointerfaces*, 2014. **120**: p. 38-46.
7. Zou, X., Z. Tian, X. Wang, M. Tan, W. Ding, and X. Lu, *Formation of magnesium silicate on surface of silica for steam reforming of liquefied petroleum gas*. *Catalysis Communications*, 2015. **68**: p. 116-119.
8. Krysztafkiewicz, A., L.K. Lipska, F. Ciesielczyk, and T. Jesionowski, *Amorphous magnesium silicate — synthesis, physicochemical properties and surface morphology*. *Advanced Powder Technology*, 2004. **15**(5): p. 549-565.
9. Rashid, I., N.H. Daraghme, M.M. Al Omari, B.Z. Chowdhry, S.A. Leharne, H.A. Hodali, and A.A. Badwan, *Magnesium silicate*. *Profiles Drug Subst Excip Relat Methodol*, 2011. **36**: p. 241-85.
10. Ziskind, G., L.P. Yarin, S. Peles, and C. Gutfinger, *Experimental Investigation of Particle Removal from Surfaces by Pulsed Air Jets*. *Aerosol Science and Technology*, 2002. **36**(5): p. 652-659.
11. Drelich, J.J.M., *Metallurgy and Exploration, Adhesion forces measured between particles and substrates with nano-roughness*. 2006. **23**(4): p. 226-232.
12. Green, J.-B.D.J.A.c.a., *Analytical instrumentation based on force measurements: combinatorial atomic force microscopy*. 2003. **496**(1-2): p. 267-277.
13. Baykara, M.Z. and U. Schwarz, *Atomic force microscopy: Methods and applications*, in *Encyclopedia of Spectroscopy and Spectrometry*. 2017, Elsevier.
14. Vorburger, T.V., J.A. Dagata, G. Wilkening, K. Lizuka, E. Thwaite, and P.J.C.A. Lonardo, *Industrial uses of STM and AFM*. 1997. **46**(2): p. 597-620.
15. Hariharan, C.J.A.C.A.G., *Photocatalytic degradation of organic contaminants in water by ZnO nanoparticles: Revisited*. 2006. **304**: p. 55-61.
16. Devipriya, S., S.J.S.e.m. Yesodharan, and s. cells, *Photocatalytic degradation of pesticide contaminants in water*. 2005. **86**(3): p. 309-348.
17. Nied, D., K. Enemark-Rasmussen, E. L'Hopital, J. Skibsted, B.J.C. Lothenbach, and C. Research, *Properties of magnesium silicate hydrates (MSH)*. 2016. **79**: p. 323-332.

18. Luce, R.W., R.W. Bartlett, and G.A. Parks, *Dissolution kinetics of magnesium silicates*. *Geochimica et Cosmochimica Acta*, 1972. **36**(1): p. 35-50.
19. Ciesielczyk, F., A. Krysztafkiewicz, and T. Jesionowski, *Magnesium silicates – adsorbents of organic compounds*. *Applied Surface Science*, 2007. **253**(20): p. 8435-8442.
20. Nied, D., K. Enemark-Rasmussen, E. L'Hopital, J. Skibsted, and B. Lothenbach, *Properties of magnesium silicate hydrates (M-S-H)*. *Cement and Concrete Research*, 2016. **79**: p. 323-332.
21. Hartman, J.S. and R.L. Millard, *Gel synthesis of magnesium silicates: A ²⁹Si magic angle spinning NMR study*. *Physics and Chemistry of Minerals*, 1990. **17**(1): p. 1-8.
22. Wesolowski, M., *Thermal decomposition of talc: A review*. *Thermochimica Acta*, 1984. **78**(1): p. 395-421.
23. Abdo, K., *Toxicology and carcinogenesis studies of talc (CAS 14807-96-6) in F344/N rats and B6C3F1 mice (inhalation studies)*. 1993, NTP Tech Report Series 421: 1-286. National Toxicology Program, Research Triangle Park, NC.
24. Rudenko, P. and A. Bandyopadhyay, *Talc as friction reducing additive to lubricating oil*. *Applied Surface Science*, 2013. **276**: p. 383-389.
25. Rayner, J.H. and G. Brown, *Triclinic form of talc*. *Nature*, 1966. **212**(5068): p. 1352-1353.
26. Wallqvist, V., P.M. Claesson, A. Swerin, J. Schoelkopf, P.A.J.C. Gane, S.A. Physicochemical, and E. Aspects, *Interaction forces between talc and hydrophobic particles probed by AFM*. 2006. **277**(1-3): p. 183-190.
27. Fan, Z. and J.G. Lu, *Zinc oxide nanostructures: synthesis and properties*. *J Nanosci Nanotechnol*, 2005. **5**(10): p. 1561-73.
28. Djuricic, A.B. and Y.H. Leung, *Optical properties of ZnO nanostructures*. *Small*, 2006. **2**(8-9): p. 944-61.
29. Özgür, Ü., Y.I. Alivov, C. Liu, A. Teke, M.A. Reshchikov, S. Doğan, V. Avrutin, S.J. Cho, and H. Morkoç, *A comprehensive review of ZnO materials and devices*. *Journal of Applied Physics*, 2005. **98**(4).
30. Hariharan, C., *Photocatalytic degradation of organic contaminants in water by ZnO nanoparticles: Revisited*. *Applied Catalysis A: General*, 2006. **304**(Supplement C): p. 55-61.
31. Hariharan, C., *Photocatalytic degradation of organic contaminants in water by ZnO nanoparticles: Revisited*. *Applied Catalysis A: General*, 2006. **304**: p. 55-61.
32. Meephon, S., S. Puttamat, and V. Pavarajarn, *Dependence of Catalyst Surface in Photocatalytic Degradation of Phenyl Urea Herbicides*. *Engineering Journal*, 2018. **22**(5): p. 57-66.
33. Carrier, M., C. Guillard, M. Besson, C. Bordes, and H.J.T.J.o.P.C.A. Chermette, *Photocatalytic degradation of diuron: experimental analyses and simulation of HO radical attacks by density functional theory calculations*. 2009. **113**(22): p. 6365-6374.
34. Peng, Y.-K. and S.E.J.N.T. Tsang, *Facet-dependent photocatalysis of nanosize semiconductive metal oxides and progress of their characterization*. 2018. **18**: p. 15-34.

35. Binnig, G., C.F. Quate, and C. Gerber, *Atomic force microscope*. Phys Rev Lett, 1986. **56**(9): p. 930-933.
36. Cappella, B. and G. Dietler, *Force-distance curves by atomic force microscopy*. Surface Science Reports, 1999. **34**(1-3): p. 1-+.
37. Burgain, J., J. Scher, J. Petit, G. Francius, and C. Gaiani, *Links between particle surface hardening and rehydration impairment during micellar casein powder storage*. Food Hydrocolloids, 2016. **61**: p. 277-285.
38. Khan, M.K., Q.Y. Wang, and M.E. Fitzpatrick, *Atomic force microscopy (AFM) for materials characterization*. 2016: p. 1-16.
39. Butt, H.-J., M. Jaschke, and W. Ducker, *Measuring surface forces in aqueous electrolyte solution with the atomic force microscope*. Bioelectrochemistry and Bioenergetics, 1995. **38**(1): p. 191-201.
40. Butt, H.-J., B. Cappella, and M. Kappl, *Force measurements with the atomic force microscope: Technique, interpretation and applications*. Surface science reports, 2005. **59**(1-6): p. 1-152.
41. Allen, S., M.C. Davies, C.J. Roberts, S.J. Tendler, and P.M.J.T.i.B. Williams, *Atomic force microscopy in analytical biotechnology*. 1997. **15**(3): p. 101-105.
42. Rebelo, L.M., J.S. de Sousa, A.S. Abreu, M.P.M.A. Baroni, A.E.V. Alencar, S.A. Soares, J. Mendes Filho, and J.B. Soares, *Aging of asphaltic binders investigated with atomic force microscopy*. Fuel, 2014. **117**: p. 15-25.
43. Ranade, M.B., *Adhesion and Removal of Fine Particles on Surfaces*. Aerosol Science and Technology, 1987. **7**(2): p. 161-176.
44. Leite, F.L., C.C. Bueno, A.L. Da Róz, E.C. Ziemath, and O.N.J.I.j.o.m.s. Oliveira, *Theoretical models for surface forces and adhesion and their measurement using atomic force microscopy*. 2012. **13**(10): p. 12773-12856.
45. Butt, H.-J., B. Cappella, and M.J.S.s.r. Kappl, *Force measurements with the atomic force microscope: Technique, interpretation and applications*. 2005. **59**(1-6): p. 1-152.
46. Tan, C.L.C., S. Gao, B.S. Wee, A. Asa-Awuku, and B.J.R. Thio, *Adhesion of Dust Particles to Common Indoor Surfaces in an Air-Conditioned Environment*. Aerosol Science and Technology, 2014. **48**(5): p. 541-551.
47. Corn, M., *The Adhesion of Solid Particles to Solid Surfaces, I, a Review*. Journal of the Air Pollution Control Association, 1961. **11**(11): p. 523-528.
48. Götzinger, M. and W.J.P.T. Peukert, *Dispersive forces of particle-surface interactions: direct AFM measurements and modelling*. 2003. **130**(1-3): p. 102-109.
49. Tomas, J., *Micromechanics of Particle Adhesion*, in *IUTAM Symposium on Multiscale Problems in Multibody System Contacts: Proceedings of the IUTAM Symposium held in Stuttgart, Germany, February 20-23, 2006*, P. Eberhard, Editor. 2007, Springer Netherlands: Dordrecht. p. 301-316.
50. Corn, M., *The Adhesion of Solid Particles to Solid Surfaces II*. Journal of the Air Pollution Control Association, 1961. **11**(12): p. 566-584.
51. Lai, T., R. Chen, and P. Huang, *Temperature dependence of microscale adhesion force between solid surfaces using an AFM*. Journal of Adhesion Science and Technology, 2014. **29**(2): p. 133-148.

52. Lai, T., P. Huang, and Y. Cai, *Adhesion Reduction of Diamond-Like Carbon Films Based on Different Contact Geometries by Using an AFM*. The Journal of Adhesion, 2016. **92**(1): p. 18-38.
53. Barattin, R. and N. Voyer, *Chemical modifications of AFM tips for the study of molecular recognition events*. Chemical communications (Cambridge, England), 2008(13): p. 1513-1532.
54. Safenkova, I.V., A.V. Zherdev, and B.B. Dzantiev, *Application of atomic force microscopy for characteristics of single intermolecular interactions*. Biochemistry (Moscow), 2012. **77**(13): p. 1536-1552.
55. Wang, J.L. and L.J. Xu, *Advanced oxidation processes for wastewater treatment: formation of hydroxyl radical and application*. Critical reviews in environmental science and technology, 2012. **42**(3): p. 251-325.
56. Lawless, D., N. Serpone, and D. Meisel, *Role of hydroxyl radicals and trapped holes in photocatalysis. A pulse radiolysis study*. The Journal of Physical Chemistry, 1991. **95**(13): p. 5166-5170.
57. Wu, C.-Y., W.J. Wolf, Y. Levartovsky, H.A. Bechtel, M.C. Martin, F.D. Toste, and E. Gross, *High-spatial-resolution mapping of catalytic reactions on single particles*. Nature, 2017. **541**(7638): p. 511-515.
58. Wang, Z., Q. Li, H. Xu, C. Dahl-Petersen, Q. Yang, D. Cheng, D. Cao, F. Besenbacher, J.V. Lauritsen, and S. Helveg, *Controllable etching of MoS₂ basal planes for enhanced hydrogen evolution through the formation of active edge sites*. Nano Energy, 2018. **49**: p. 634-643.
59. Carrier, M., C. Guillard, M. Besson, C. Bordes, and H. Chermette, *Photocatalytic degradation of diuron: experimental analyses and simulation of HO radical attacks by density functional theory calculations*. The Journal of Physical Chemistry A, 2009. **113**(22): p. 6365-6374.
60. Meephon, S., T. Rungrotmongkol, S. Puttamat, S. Praserttham, and V. Pavarajarn, *Heterogeneous photocatalytic degradation of diuron on zinc oxide: Influence of surface-dependent adsorption on kinetics, degradation pathway, and toxicity of intermediates*. Journal of Environmental Sciences, 2019. **84**: p. 97-111.
61. Jang, E.S., J.H. Won, S.J. Hwang, and J.H. Choy, *Fine tuning of the face orientation of ZnO crystals to optimize their photocatalytic activity*. Advanced Materials, 2006. **18**(24): p. 3309-3312.
62. Schneider, J., M. Matsuoka, M. Takeuchi, J. Zhang, Y. Horiuchi, M. Anpo, and D.W. Bahnemann, *Understanding TiO₂ photocatalysis: mechanisms and materials*. Chemical reviews, 2014. **114**(19): p. 9919-9986.
63. Bai, S., L. Wang, Z. Li, and Y. Xiong, *Facet-engineered surface and interface design of photocatalytic materials*. Advanced Science, 2017. **4**(1): p. 1600216.
64. Özgür, Ü., Y.I. Alivov, C. Liu, A. Teke, M. Reshchikov, S. Doğan, V. Avrutin, S.-J. Cho, and Morkoç, *A comprehensive review of ZnO materials and devices*. Journal of applied physics, 2005. **98**(4): p. 11.
65. Peng, Y.-K. and S.E. Tsang, *Facet-dependent photocatalysis of nanosize semiconductive metal oxides and progress of their characterization*. Nano Today, 2018. **18**: p. 15-34.
66. Dulub, O., U. Diebold, and G. Kresse, *Novel stabilization mechanism on polar surfaces: ZnO (0001)-Zn*. Physical review letters, 2003. **90**(1): p. 016102.

67. Dulub, O., L.A. Boatner, and U. Diebold, *STM study of the geometric and electronic structure of ZnO (0001)-Zn,(0001)-O,(1010), and (1120) surfaces*. Surface Science, 2002. **519**(3): p. 201-217.
68. Parker, T., N. Condon, R. Lindsay, F. Leibsle, and G. Thornton, *Imaging the polar (0001) and non-polar (1010) surfaces of ZnO with STM*. Surface science, 1998. **415**(3): p. L1046-L1050.
69. Yin, X.-L., A. Birkner, K. Hänel, T. Löber, U. Köhler, and C. Wöll, *Adsorption of atomic hydrogen on ZnO (101 [combining macron] 0): STM study*. Physical Chemistry Chemical Physics, 2006. **8**(13): p. 1477-1481.
70. Duke, C. and A. Lubinsky, *Calculations of low-energy electron diffraction intensities from the polar faces of ZnO*. SurSc, 1975. **50**(2): p. 605-614.
71. Jedrecy, N., S. Gallini, M. Sauvage-Simkin, and R. Pinchaux, *The ZnO non-polar (1010) surface: an X-ray structural investigation*. Surface science, 2000. **460**(1-3): p. 136-143.
72. Ostendorf, F., S. Torbrügge, and M. Reichling, *Atomic scale evidence for faceting stabilization of a polar oxide surface*. Physical Review B, 2008. **77**(4): p. 041405.
73. Peng, Y.-K., L. Ye, J. Qu, L. Zhang, Y. Fu, I.F. Teixeira, I.J. McPherson, H. He, and S.C.E. Tsang, *Trimethylphosphine-assisted surface fingerprinting of metal oxide nanoparticle by ³¹P solid-state NMR: A zinc oxide case study*. Journal of the American Chemical Society, 2016. **138**(7): p. 2225-2234.
74. Dong, Y., R. An, S. Zhao, W. Cao, L. Huang, W. Zhuang, L. Lu, and X. Lu, *Molecular Interactions of Protein with TiO₂ by the AFM-Measured Adhesion Force*. Langmuir, 2017. **33**(42): p. 11626-11634.
75. Wang, M.S., L.B. Palmer, J.D. Schwartz, and A. Razatos, *Evaluating protein attraction and adhesion to biomaterials with the atomic force microscope*. Langmuir, 2004. **20**(18): p. 7753-7759.
76. Chu, S.Y., T.M. Yan, and S.L. Chen, *Characteristics of sol-gel synthesis of ZnO-based powders*. Journal of Materials Science Letters, 2000. **19**(4): p. 349-352.
77. Vafaei, M. and M.S. Ghamsari, *Preparation and characterization of ZnO nanoparticles by a novel sol-gel route*. Materials Letters, 2007. **61**(14-15): p. 3265-3268.
78. Chen, Y.W., Q. Qiao, Y.C. Liu, and G.L. Yang, *Size-Controlled Synthesis and Optical Properties of Small-Sized ZnO Nanorods*. Journal of Physical Chemistry C, 2009. **113**(18): p. 7497-7502.
79. Lepot, N., M.K. Van Bael, H. Van den Rul, J. D'Haen, R. Peeters, D. Franco, and J. Mullens, *Synthesis of ZnO nanorods from aqueous solution*. Materials Letters, 2007. **61**(13): p. 2624-2627.
80. Ito, T., M. Namba, P. Bühlmann, and Y. Umezawa, *Modification of Silicon Nitride Tips with Trichlorosilane Self-Assembled Monolayers (SAMs) for Chemical Force Microscopy*. Langmuir, 1997. **13**(16): p. 4323-4332.
81. Barattin, R. and N. Voyer, *Chemical modifications of atomic force microscopy tips*, in *Atomic Force Microscopy in Biomedical Research*. 2011, Springer. p. 457-483.

82. Jakša, G., B. Štefane, and J. Kovač, *XPS and AFM characterization of aminosilanes with different numbers of bonding sites on a silicon wafer*. Surface and interface analysis, 2013. **45**(11-12): p. 1709-1713.
83. Meephon, S., T. Rungrotmongkol, N. Kaiyawet, S. Puttamat, and V. Pavarajarn, *Surface-dependence of adsorption and its influence on heterogeneous photocatalytic reaction: A case of photocatalytic degradation of linuron on zinc oxide*. Catalysis Letters, 2018. **148**(3): p. 873-881.
84. Liu, B. and H.C. Zeng, *Hydrothermal synthesis of ZnO nanorods in the diameter regime of 50 nm*. Journal of the American Chemical Society, 2003. **125**(15): p. 4430-4431.
85. Ricci, D. and P.C. Braga, *Recognizing and avoiding artifacts in AFM imaging*, in *Atomic Force Microscopy*. 2004, Springer. p. 25-37.
86. Shircliff, R.A., P. Stradins, H. Moutinho, J. Fennell, M.L. Ghirardi, S.W. Cowley, H.M. Branz, and I.T. Martin, *Angle-resolved XPS analysis and characterization of monolayer and multilayer silane films for DNA coupling to silica*. Langmuir, 2013. **29**(12): p. 4057-4067.
87. Jakša, G., B. Štefane, and J. Kovač, *Influence of different solvents on the morphology of APTMS-modified silicon surfaces*. Applied Surface Science, 2014. **315**: p. 516-522.
88. Hashemi, A. and A. Bahari, *Structural and dielectric characteristic of povidone–silica nanocomposite films on the Si (n) substrate*. Applied Physics A, 2017. **123**(8): p. 535.
89. Yang, S., L. Liu, Z. Jia, W. Fu, D. Jia, and Y. Luo, *Study on the structure-properties relationship of natural rubber/SiO₂ composites modified by a novel multi-functional rubber agent*. eXPRESS Polymer Letters, 2014. **8**(6).
90. Gusain, R., S. Kokufu, P.S. Bakshi, T. Utsunomiya, T. Ichii, H. Sugimura, and O.P. Khatri, *Self-assembled thin film of imidazolium ionic liquid on a silicon surface: Low friction and remarkable wear-resistivity*. Applied Surface Science, 2016. **364**: p. 878-885.
91. Bogusz, K., M. Tehei, C. Stewart, M. McDonald, D. Cardillo, M. Lerch, S. Corde, A. Rosenfeld, H.K. Liu, and K. Konstantinov, *Synthesis of potential theranostic system consisting of methotrexate-immobilized (3-aminopropyl)trimethoxysilane coated alpha-Bi₂O₃ nanoparticles for cancer treatment*. Rsc Advances, 2014. **4**(46): p. 24412-24419.
92. Suddai, A., P. Nuengmatcha, P. Sricharoen, N. Limchoowong, and S. Chanthai, *Feasibility of hard acid-base affinity for the pronounced adsorption capacity of manganese(II) using amino-functionalized graphene oxide*. Rsc Advances, 2018. **8**(8): p. 4162-4171.
93. Gao, N.W., M. Li, W.H. Jing, Y.Q. Fan, and N.P. Xu, *Improving the filtration performance of ZrO₂ membrane in non-polar organic solvents by surface hydrophobic modification*. Journal of Membrane Science, 2011. **375**(1-2): p. 276-283.
94. De Conto, J.F., M.R. Oliveira, M.M. Oliveira, T.G. Brandao, K.V. Campos, C.C. Santana, and S.M. Egues, *One-pot synthesis and modification of silica nanoparticles with 3-chloropropyl-trimethoxysilane assisted by microwave irradiation*. Chemical Engineering Communications, 2018. **205**(4): p. 533-537.

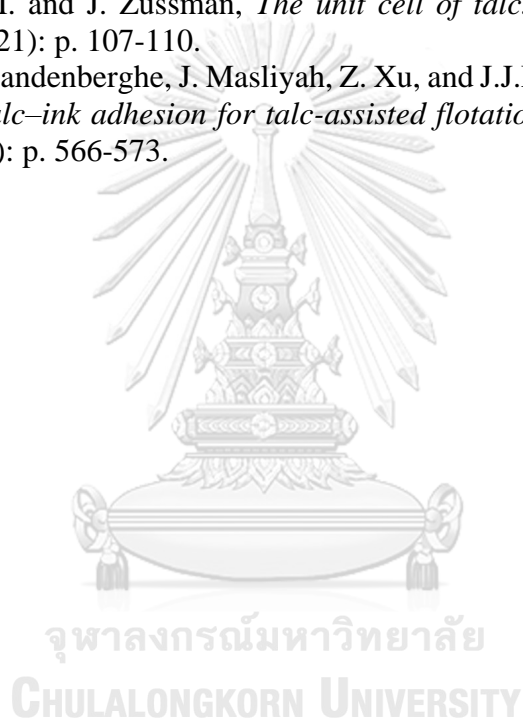
95. Lai, T., R. Chen, and P. Huang, *Temperature dependence of microscale adhesion force between solid surfaces using an AFM*. Journal of Adhesion Science and Technology, 2015. **29**(2): p. 133-148.
96. Lai, T., S. Zhu, and P. Huang, *Adhesion behavior of a grating at a single location by using an AFM flat tip under different conditions*. The Journal of Adhesion, 2016. **92**(3): p. 194-213.
97. Zhou, H., M. Götzinger, and W. Peukert, *The influence of particle charge and roughness on particle–substrate adhesion*. Powder Technology, 2003. **135-136**: p. 82-91.
98. Götzinger, M. and W. Peukert, *Dispersive forces of particle–surface interactions: direct AFM measurements and modelling*. Powder Technology, 2003. **130**(1-3): p. 102-109.
99. Leite, F.L., C.C. Bueno, A.L. Da Róz, E.C. Ziemath, and O.N. Oliveira, *Theoretical models for surface forces and adhesion and their measurement using atomic force microscopy*. International journal of molecular sciences, 2012. **13**(10): p. 12773-12856.
100. Hamaker, H., *A simple and general extension of the three halves power law*. Physica, 1942. **9**(1): p. 135-138.
101. Bergström, L., *Hamaker constants of inorganic materials*. Advances in Colloid and Interface Science, 1997. **70**: p. 125-169.
102. Reifenger, R., *Fundamentals of Atomic Force Microscopy: Part I: Foundations*. 2016: World Scientific Publishing Company Pte. Limited.
103. Kornherr, A., S. Hansal, W.E. Hansal, J.O. Besenhard, H. Kronberger, G.E. Nauer, and G. Zifferer, *Molecular dynamics simulations of the adsorption of industrial relevant silane molecules at a zinc oxide surface*. The Journal of chemical physics, 2003. **119**(18): p. 9719-9728.
104. Kornherr, A., S.A. French, A.A. Sokol, C.R.A. Catlow, S. Hansal, W.E. Hansal, J.O. Besenhard, H. Kronberger, G.E. Nauer, and G. Zifferer, *Interaction of adsorbed organosilanes with polar zinc oxide surfaces: a molecular dynamics study comparing two models for the metal oxide surface*. Chemical Physics Letters, 2004. **393**(1-3): p. 107-111.
105. Kornherr, A., G.E. Nauer, A.A. Sokol, S.A. French, C.R.A. Catlow, and G. Zifferer, *Adsorption of organosilanes at a Zn-terminated ZnO (0001) surface: molecular dynamics study*. Langmuir, 2006. **22**(19): p. 8036-8042.
106. Wander, A. and N. Harrison, *An ab initio study of hydrogen adsorption on ZnO (1010)*. The Journal of Physical Chemistry B, 2001. **105**(26): p. 6191-6193.
107. Jacobs, R., B. Zheng, B. Puchala, P.M. Voyles, A.B. Yankovich, and D. Morgan, *Counterintuitive reconstruction of the polar O-terminated ZnO surface with zinc vacancies and hydrogen*. The journal of physical chemistry letters, 2016. **7**(22): p. 4483-4487.
108. Wander, A. and N. Harrison, *The stability of polar oxide surfaces: The interaction of H₂O with ZnO (0001) and ZnO (000 $\bar{1}$)*. The Journal of chemical physics, 2001. **115**(5): p. 2312-2316.
109. Wang, Y., B. Meyer, X. Yin, M. Kunat, D. Langenberg, F. Traeger, A. Birkner, and C. Wöll, *Hydrogen Induced Metallicity on the ZnO (10 1 0) Surface*. Physical review letters, 2005. **95**(26): p. 266104.

110. Meyer, B. and D. Marx, *Density-functional study of the structure and stability of ZnO surfaces*. Physical Review B, 2003. **67**(3): p. 035403.
111. Bamba, D., P. Atheba, D. Robert, A. Trokourey, and B. Dongui, *Photocatalytic degradation of the diuron pesticide*. Environmental Chemistry Letters, 2008. **6**(3): p. 163-167.
112. Katsumata, H., M. Sada, Y. Nakaoka, S. Kaneco, T. Suzuki, and K. Ohta, *Photocatalytic degradation of diuron in aqueous solution by platinized TiO₂*. Journal of Hazardous Materials, 2009. **171**(1-3): p. 1081-1087.
113. Malato, S., J. Cáceres, A. Fernández-Alba, L. Piedra, M. Hernando, A. Agüera, and J. Vial, *Photocatalytic treatment of diuron by solar photocatalysis: evaluation of main intermediates and toxicity*. Environmental science & technology, 2003. **37**(11): p. 2516-2524.
114. Wesółowski, M.J.T.A., *Thermal decomposition of talc: A review*. 1984. **78**(1-3): p. 395-421.
115. Claverie, M., A. Dumas, C. Carême, M. Poirier, P. Micoud, F. Martin, and C. Aymonier, *Synthetic talc and talc-like structures: preparation, features and applications*. 2018.
116. Andrić, L., A. Terzić, Z. Aćimović-Pavlović, L. Pavlović, and M. Petrov, *Comparative kinetic study of mechanical activation process of mica and talc for industrial application*. Composites Part B: Engineering, 2014. **59**: p. 181-190.
117. Cai, C.-j., Z.-g. Shen, Y.-h. Zheng, Y.-s. Xing, and S.-l.J.J.o.m.s. Ma, *A novel technology for powder dispersion and surface modification*. 2007. **42**(11): p. 3745-3753.
118. Sinha Ray, S. and M. Okamoto, *Polymer/layered silicate nanocomposites: a review from preparation to processing*. Progress in Polymer Science, 2003. **28**(11): p. 1539-1641.
119. HASHIZUME, H.J.C.S., *Adsorption of aromatic compounds in water by talc*. 2009. **14**(2): p. 61-64.
120. Zhan, F. and N. Chen, *Studies on Friction and Mechanical Properties of High Density Polypropylene (HDPP) Filled with Modified Talc*. Advanced Materials Research, 2012. **624**: p. 279-282.
121. Malandrini, H., F. Clauss, S. Partyka, J.J.J.o.c. Douillard, and i. science, *Interactions between talc particles and water and organic solvents*. 1997. **194**(1): p. 183-193.
122. Tarasevich, Y.I. and E.V. Aksenenko, *Interaction of water molecules with hydrophilic and hydrophobic surfaces of colloid particles*. Journal of Water Chemistry and Technology, 2015. **37**(5): p. 224-229.
123. Jaynes, W., S.J.C. Boyd, and c. minerals, *Hydrophobicity of siloxane surfaces in smectites as revealed by aromatic hydrocarbon adsorption from water*. 1991. **39**(4): p. 428-436.
124. Song, S., A. Lopez-Valdivieso, and Y.J.P.T. Ding, *Effects of nonpolar oil on hydrophobic flocculation of hematite and rhodochrosite fines*. 1999. **101**(1): p. 73-80.
125. Šolc, R., M.H. Gerzabek, H. Lischka, and D. Tunega, *Wettability of kaolinite (001) surfaces — Molecular dynamic study*. Geoderma, 2011. **169**: p. 47-54.

126. Yin, X., J.J.M. Miller, Metallurgy, and Exploration, *Wettability of kaolinite basal planes based on surface force measurements using atomic force microscopy*. 2012. **29**(1): p. 13-19.
127. Tarasevich, Y.I., E.J.J.o.W.C. Aksenenko, and Technology, *Interaction of water molecules with hydrophilic and hydrophobic surfaces of colloid particles*. 2015. **37**(5): p. 224-229.
128. Fiorentino, B., R. Fulchiron, V. Bounor-Legaré, J.-C. Majesté, J.C. Leblond, and J.J.A.C.S. Duchet-Rumeau, *Chemical modification routes of synthetic talc: Influence on its nucleating power and on its dispersion state*. 2015. **109**: p. 107-118.
129. Li, S.-F., S.-C. Yang, S.-L. Zhao, P. Li, and J.-H.J.J.o.t.S.C.S. Zhang, *Microwave and acid modified talc as adsorbents of methylene blue in aqueous solution*. 2015. **80**(4): p. 563-574.
130. Xanthos, M., *Functional fillers for plastics*. 2010: John Wiley & Sons.
131. Hadal, R., A. Dasari, J. Rohrmann, R.J.M.S. Misra, and E. A, *Effect of wollastonite and talc on the micromechanisms of tensile deformation in polypropylene composites*. 2004. **372**(1-2): p. 296-315.
132. Liu, K., W. Stadlbauer, G. Zitzenbacher, C. Paulik, and C. Burgstaller. *Effects of surface modification of talc on mechanical properties of polypropylene/talc composites*. in *AIP Conference Proceedings*. 2016. AIP Publishing LLC.
133. Xu, L., J. Tian, H. Wu, S. Fang, Z. Lu, C. Ma, W. Sun, Y.J.A.i.c. Hu, and i. science, *Anisotropic surface chemistry properties and adsorption behavior of silicate mineral crystals*. 2018. **256**: p. 340-351.
134. Gupta, V., J.D.J.J.o.C. Miller, and I. Science, *Surface force measurements at the basal planes of ordered kaolinite particles*. 2010. **344**(2): p. 362-371.
135. Israelachvili, J.N., *Intermolecular and surface forces*. 2011: Academic press.
136. Yang, D., L. Xie, E. Bobicki, Z. Xu, Q. Liu, and H.J.L. Zeng, *Probing anisotropic surface properties and interaction forces of chrysotile rods by atomic force microscopy and rheology*. 2014. **30**(36): p. 10809-10817.
137. Liu, J., L. Sandaklie-Nikolova, X. Wang, J.D.J.J.o.c. Miller, and i. science, *Surface force measurements at kaolinite edge surfaces using atomic force microscopy*. 2014. **420**: p. 35-40.
138. Nalaskowski, J., B. Abdul, H. Du, and J.D. Miller, *Anisotropic Character of Talc Surfaces as Revealed by Streaming Potential Measurements, Atomic Force Microscopy, Molecular Dynamics Simulations and Contact Angle Measurements*. Canadian Metallurgical Quarterly, 2007. **46**(3): p. 227-235.
139. Braga, P.C. and D. Ricci, *Atomic force microscopy in biomedical research: Methods and protocols*. 2011: Springer.
140. Castillo, L.A., S.E. Barbosa, P. Maiza, and N.J.J.J.o.M.s. Capiati, *Surface modifications of talcs. Effects of inorganic and organic acid treatments*. 2011. **46**(8): p. 2578-2586.
141. Zdrávková, J., M. Valášková, and S. Študentová. *Talc properties after acid treatment and mechanical procedures*. in *Proceedings of the 5th International Conference on Nanoma-terials, NANOCON-2013*. 2013.
142. Rywak, A.A. and J.M. Burlitch, *The crystal chemistry and thermal stability of sol-gel prepared fluoride-substituted talc*. Physics and Chemistry of Minerals, 1996. **23**(7): p. 418-431.

143. Perez, F.D. and J.M. Burlitch, *Sol-gel synthesis of fluoride-substituted talc*. Chemistry of Materials, 1995. **7**(12): p. 2277-2283.
144. Blanchard, M., M. Meheut, L. Delon, M. Poirier, P. Micoud, C. Le Roux, and F. Martin, *Infrared spectroscopic study of the synthetic Mg-Ni talc series*. Physics and Chemistry of Minerals, 2018. **45**(9): p. 843-854.
145. Yang, H.M., C.F. Du, Y.H. Hu, S.M. Jin, W.G. Yang, A.D. Tang, and E.G. Avvakumov, *Preparation of porous material from talc by mechanochemical treatment and subsequent leaching*. Applied Clay Science, 2006. **31**(3-4): p. 290-297.
146. Liu, C., W.C. Zhang, S.X. Song, and H.Q. Li, *A novel method to improve carboxymethyl cellulose performance in the flotation of talc*. Minerals Engineering, 2019. **131**: p. 23-27.
147. Fidalgo, A. and L.M. Ilharco, *The defect structure of sol-gel-derived silica/polytetrahydrofuran hybrid films by FTIR*. Journal of Non-Crystalline Solids, 2001. **283**(1-3): p. 144-154.
148. Hofmeister, A.M. and J.E. Bowey, *Quantitative infrared spectra of hydrosilicates and related minerals*. Monthly Notices of the Royal Astronomical Society, 2006. **367**(2): p. 577-591.
149. Raquez, J.M., Y. Nabar, R. Narayan, and P. Dubois, *Novel high-performance talc/poly[(butylene adipate)-co-terephthalate] hybrid materials*. Macromolecular Materials and Engineering, 2008. **293**(4): p. 310-320.
150. Dietrich, P.M., C. Streeck, S. Glamsch, C. Ehlert, A. Lippitz, A. Nutsch, N. Kulak, B. Beckhoff, and W.E.S. Unger, *Quantification of Silane Molecules on Oxidized Silicon: Are there Options for a Traceable and Absolute Determination?* Analytical Chemistry, 2015. **87**(19): p. 10117-10124.
151. Dokmai, V., R. Methaapanon, and V. Pavarajarn, *Corrosion of amorphous alumina in deionized water under mild condition*. Applied Surface Science, 2020. **499**: p. 143906.
152. Zheng, Y.Y., C.D. Xiong, Z.C. Wang, and L.F. Zhang, *Enhanced osteoblast cells adhesion, spreading, and proliferation to surface-carboxylated poly(etheretherketone)*. Journal of Bioactive and Compatible Polymers, 2015. **30**(3): p. 302-318.
153. Vogt, A.D., T. Han, and T.P. Beebe, *Adsorption of 11-mercaptoundecanoic acid on Ni(111) and its interaction with probe molecules*. Langmuir, 1997. **13**(13): p. 3397-3403.
154. Fraile, J.M., J.I. García, J.A. Mayoral, and E.J.A.C.A.G. Vispe, *Comparison of hydrophilic and hydrophobic silicas as supports for titanium catalysts*. 2004. **276**(1-2): p. 113-122.
155. Gallego, J.-C., M. Jaber, J. Miehé-Brendlé, and C.J.N.J.o.C. Marichal, *Synthesis of new lamellar inorganic-organic talc-like hybrids*. 2008. **32**(3): p. 407-412.
156. Xie, Y., C.A. Hill, Z. Xiao, H. Militz, C.J.C.P.A.A.S. Mai, and Manufacturing, *Silane coupling agents used for natural fiber/polymer composites: A review*. 2010. **41**(7): p. 806-819.
157. Paul, R., S.N. Das, S. Dalui, R.N. Gayen, R.K. Roy, R. Bhar, and A.K. Pal, *Synthesis of DLC films with different sp²/sp³ ratios and their hydrophobic behaviour*. Journal of Physics D: Applied Physics, 2008. **41**(5).

158. Lin, Z., Z. Yu, and Y. Wei, *Measurement of nanoindentation properties of polymers considering adhesion effects between AFM sharp indenter and material*. Journal of Adhesion Science and Technology, 2020. **34**(15): p. 1591-1608.
159. Ito, T., M. Namba, P. Bühlmann, and Y.J.L. Umezawa, *Modification of silicon nitride tips with trichlorosilane self-assembled monolayers (SAMs) for chemical force microscopy*. 1997. **13**(16): p. 4323-4332.
160. Lifshitz, E.M. and M. Hamermesh, *The theory of molecular attractive forces between solids*, in *Perspectives in Theoretical Physics*. 1992, Elsevier. p. 329-349.
161. Hamaker, H.C., *A simple and general extension of the three halves power law*. Physica, 1942. **9**(1): p. 135-138.
162. Akizuki, M. and J. Zussman, *The unit cell of talc*. Mineralogical Magazine, 1978. **42**(321): p. 107-110.
163. Liu, J., J. Vandenberghe, J. Masliyah, Z. Xu, and J.J.M.e. Yordan, *Fundamental study on talc-ink adhesion for talc-assisted flotation deinking of wastepaper*. 2007. **20**(6): p. 566-573.





APPENDIX A
Adhesion measurements after classification and statistical tests

A1: Summary of adhesion energies determined in **Figure 15** with fitting parameters

Particles or surface	Type of tip modification															
	NH ₂ -terminated			Cl-terminated			CH ₃ -terminated			Unmodified Si tip						
	\bar{x}^a	S.D. _b	N ^c	χ^2 ^d	\bar{x}^a	S.D. _b	N ^c	χ^2 ^d	\bar{x}^a	S.D. _b	N ^c	χ^2 ^d	\bar{x}^a	S.D. _b	N ^c	χ^2 ^d
Conventional ZnO particles: the population with lower adhesion energy	62.82	1.41	48	6.19	44.42	8.37	62	10.58	3.71	0.79	72	4.41	3.24	1.04	66	6.08
Conventional ZnO particles: the population with higher adhesion energy	120.41	6.66	43	9.20	83.32	2.48	42	19.35	11.25	0.65	58	3.38	8.50	0.27	60	3.99
ZnO nanorods	44.11	4.15	68	5.49	21.84	3.75	69	15.48	6.28	0.75	66	16.57	1.42	0.40	80	11.99
The standard Zn-terminated ZnO surface	121.65	4.00	50	47.54	87.65	3.77	34	5.69	4.11	0.31	36	1.63	9.73	0.51	49	14.78
The standard O-terminated ZnO surface	62.91	8.90	44	9.63	46.37	1.77	25	25.17	10.47	0.87	39	11.12	3.64	0.43	57	2.24

A 2: Hypothesis t-test results of adhesion energies determined from interactions between various modified AFM tips and ZnO particles

Comparison of adhesion energies from	Type of tip modification							
	NH ₂ -terminated		Cl-terminated		CH ₃ -terminated		Unmodified Si tip	
	Test Result ^c	P-Value	Test Result ^a	P-Value	Test Result ^a	P-Value	Test Result ^a	P-Value
Conventional ZnO powder Vs. ZnO nanorods	Significantly different	1.55E-40	Significantly different	6.22E-34	Significantly different	0.0124	Significantly different	7.96E-34
The population of conventional ZnO powder that has lower adhesion energy Vs. the relevant standard ZnO surface ^b	NOT significantly different (O-terminated ZnO surface)	0.0702	NOT significantly different (O-terminated ZnO surface)	0.698	NOT significantly different (Zn-terminated ZnO surface)	0.700	NOT significantly different (O-terminated ZnO surface)	0.0602
The population of conventional ZnO powder that has higher adhesion energy Vs. the relevant standard ZnO surface	NOT significantly different (Zn-terminated ZnO surface)	0.339	NOT significantly different (Zn-terminated ZnO surface)	0.558	NOT significantly different (O-terminated ZnO surface)	0.132	NOT significantly different (Zn-terminated ZnO surface)	0.0760
The population of conventional ZnO powder that has lower Vs. higher adhesion energy	Significantly different	5.04E-49	Significantly different	2.44E-42	Significantly different	2.01E-31	Significantly different	7.72E-57

APPENDIX B

Linear model fits for the correlations between the maximum adhesion forces within the observed ranges by Si-tip/DLC-tip and the contact angle of unmodified/modified talc particles.

Interacting tips	Position within the range	Slope			Intercept			χ^2 ^a	R^2 ^b
		Value	Standard error	Value	Standard error				
Si-tip	Max	-0.0402	0.0126	6.0076	0.8696	0.20	0.84		
	Mean	-0.0384	0.0096	5.2295	0.6611	0.12	0.89		
	Min	-0.0369	0.0093	4.4969	0.6405	0.11	0.89		
DLC-tip	Max	-0.0407	0.0067	4.7212	0.4620	0.06	0.95		
	Mean	-0.0332	0.0062	3.6925	0.4302	0.05	0.93		
	Min	-0.0244	0.0070	2.5165	0.4823	0.06	0.86		

^a Chi squared value (minimized for a good fit), ^b R squared value (in terms of distance from points to be best fitting line)

VITA

NAME Vipada Dokmai

DATE OF BIRTH 02 February 1991

PLACE OF BIRTH Nakhonratchasima province

INSTITUTIONS ATTENDED She finished high school from Satrichaiyaphum School, Chaiyaphum in 2009. In 2013, she received and got the second class honor in Bachelor's Degree of Chemical Engineering from Khon Kean University. Her senior project studied about the developing precise model of corrosion and fouling monitoring in condenser. She had an experience in operation engineering at Gulf Power Generation. After that, she gained admission to Graduated School of Chulalongkorn University in Center of Excellence in Particle Technology and graduated in 2015 with the thesis entitled "Alumina Corrosion in Deionized water". She continued studying Doctoral degree of Chemical Engineering, Chulalongkorn University since August 2015 and received grant fund from Thailand Science Research and Innovation through Research and Researchers for Industries Program.

HOME ADDRESS 225 Moo.1, Nivetrat Rd., Kaeng Sanam Nang, Kaeng Sanam Nang, Nakhonratchasima, 30440, Thailand.

PUBLICATION

1. Vipada Dokmai, Rungthiwa Methaapanon, Varong Pavarajarn, Corrosion of amorphous alumina in deionized water under mild condition. Applied Surface Science, 2020. 499: p. 143906.
2. Vipada Dokmai, Worasom Kundhikanjana, Narong Chanlek, Kitiphath Sinthipharakoon, Udom Sae-Ueng, Witchukorn Phuthong and Varong Pavarajarn, Effects of catalyst surfaces on adsorption revealed by atomic force microscope force spectroscopy: photocatalytic degradation of diuron over zinc oxide. Physical Chemistry Chemical Physics, 2020. 22(26): p. 15035-15047.